SELF-HEALING MATERIALS AND MULTINOZZLE PRINTHEADS WITH EMBEDDED MICROVASCULAR NETWORKS

BY

CHRISTOPHER JOHN HANSEN

DISSERTATION

Submitted in partial fulfillment of the requirements
for the degree of Doctor of Philosophy in Materials Science and Engineering
in the Graduate College of the
University of Illinois at Urbana-Champaign, 2011

Urbana, Illinois

Doctoral Committee:

Professor Jennifer Lewis, Chair
Professor Paul Braun
Professor Nancy Sottos
Professor Scott White

ABSTRACT

Microvascular networks are pervasive in biological systems, assisting in the repair of tissue damage, regulation of temperature, and efficient distribution of nutrients. Emulating these functional attributes in engineering contexts such as self-healing materials, microfluidic temperature regulation, and tissue engineering is gaining significant attention. Yet, the ability to design and replicate synthetic microvascular networks remains a challenge with limited progress to date. The objectives of this dissertation are to (1) create self-healing materials with interpenetrating microvascular networks via direct-write assembly of fugitive organic inks, (2) design systems with controlled thermal regulation and investigate their self-healing behavior, and (3) produce multinozzle printheads composed of biomimetic microvascular networks for high-throughput printing.

Self-healing materials with embedded interpenetrating microvascular networks in an epoxy substrate/coating architecture are fabricated by direct-write assembly. Two key fabrication advancements were required: (1) dual ink printing to produce separate interpenetrating networks and (2) vertical ink printing to provide a healing agent transport pathway from the embedded network to the damage region. Each network is filled with one component of a two-part epoxy resin, which flow into the crack plane upon fracture and polymerize to restore mechanical strength. This microvascular platform enables the use of new liquid healing chemistries and repeated healing of at least 30 cycles of mechanical damage in the coating by independently supplying both healing agents to the damaged region(s).

To overcome slow healing kinetics that require multiple days between damage events to recover mechanical performance under ambient conditions, their design is modified to include a third interpenetrating microvascular network within these epoxy coating/substrate architectures. Two of these networks contain epoxy resin and hardener healing agents, which remain sequestered until mechanical fracture of the coating triggers their release to the damaged region. The third interpenetrating network is used to circulate a temperature-controlled fluid that locally heats the damaged region. Temperature isotherms of 30, 50 and 70°C are achieved within minutes, yielding a sharp reduction in the healing time, from 48 to 4 hr, required for mechanical property restoration.

Finally, multinozzle printheads for high throughput direct-write assembly are designed and implemented. These hierarchical microvascular networks, which are composed of 6 bifurcating generations, are fabricated by CNC-milling of an acrylic substrate to create 64 square nozzles (~200 x 200 μm^2 with a center-to-center spacing of 400 μm) that are bonded by solvent welding to a solid acrylic substrate. Computational fluid modeling reveals that a uniform velocity profile within each generation of the bifurcating network is established independent of the specific ink rheology. Microvascular printheads demonstrate equal printing rates that produce filamentary features of uniform width and height. Multiple multinozzle networks are also coupled with prescribed offset distances to create multi-material printheads. Due to the highly parallel nature of the deposition, 3D structures are rapidly fabricated within minutes over large areas (~1 m^2).

ACKNOWLEDGMENTS

I wish to express my unending gratitude to my husband Jonathan for his steadfast support in my graduate studies and future aspirations. For all of the weekends he traveled from Peoria, only for me to leave to spend hours in lab or with the robocaster, I thank him for his patience and understanding. I am truly the luckiest to have found a "be"-er to counterbalance my "do"-er mentality, and who points out the iridescent bugs of life.

I thank my parents, Craig and Susan, for their support in my continuing studies, especially the restraint they demonstrated to avoid the question "when will you be done?", and to instead comment in awe at colorful paper figures.

I am deeply grateful for the support of my advisor, Professor Jennifer Lewis, who has generously provided her time, funding and advice. Her support of new and interesting ideas and pursuit of academic and industrial collaborations has provided me with opportunities beyond my imagining when I arrived at Illinois. I anticipate my appreciation of this support will only grow with time, as I pursue my future career.

I wish to thank my committee members, Professors Scott White, Nancy Sottos, and Paul Braun, for their guidance and support through the Autonomic Materials Systems (AMS) group. I greatly appreciative the open, collaborative, and supportive atmosphere fostered within the group. I also wish to thank the students of the AMS group, particularly those on the Microvascular MURI, who helped with the nitty-gritty details of experimental lab work. I am especially grateful to Dr. Kathleen Toohey, Dr. Andrew Hamilton, Brian Kozola, Rajat Saksena, David McIlroy, Cassandra Kingsbury, Jericho Moll, Dr. Alejandro Aragón, and Dr. Solar Olegubefola.

Finally, I wish to thank my fellow research group members. Your constant advice, teaching, critiques, and entertainment have immensely helped my journey through graduate school. Though I am grateful to each and every group member, I wish to specifically thank: Prof. Jacinta Conrad and Dr. Jun Yoshikawa for being amazing officemates; Dr. Willie Wu for his microvascular and robocasting knowledge and assistance; Drs. Rob Shepherd, Summer Rhodes, Sara Parker, Ranjeet Rao, Dan Harris, Bok Yeop Ahn, Mingjie Xu, and Eric Duoss for their help with integrating into graduate school; Matt Montgomery and John Vericella for staying up night after night to meet industrial deadlines; Profs. Jacinta Conrad and Liz Glogowski for assistance with academic applications and interviews; and John Bukowski for his lab knowledge befitting a jack-of-all trades, his introduction to Moon-Glo, and his inspiring optimism. I hope all of our paths will continue to cross in the coming years.

TABLE OF CONTENTS

CHAPTER 1

INTRODUCTION

Biological microvascular networks provide inspiration for successful incorporation of multi-functionality in engineered materials. In biology, microvascular networks provide optimal fluid flow for nutrient and waste transport to sustain tissues,[1, 2] thermal transport to conserve or dissipate body heat,[3-5] and damage-induced clotting to mend injury.[6] One approach to replicating this multi-functionality in engineered materials is via embedded synthetic microvascular networks. Recent efforts have focused on incorporating synthetic microvasculature into materials for autonomic healing,[7-9] micro-component cooling,[10-12] tissue engineering,[13-15] lab-on-chip devices,[16-18] 3D microfluidics,[19-21] and micro-fuel cells.[22-24]

My dissertation focuses on enhancing healing repeatability and kinetics in self-healing materials via embedded interpenetrating microvascular networks. This work builds upon pioneering research that first relied on microcapsules to deliver healing agent to damage regions. However, this discrete reservoir limits the availability of fluid to heal a damage region[25-28] and allows only single-event healing of a given region. By contrast, embedded microvascular networks can supply a virtually limitless amount of healing agent when fed by a sufficiently large reservoir, thereby enabling numerous healing cycles of localized damage.[7-9]

Several fabrication techniques may be used to incorporate microvascular networks into materials systems, including direct ink writing,[20, 29-32] soft lithography,[33-35] stereolithography,[36-38] 2-photon polymerization,[39, 40] etch processes,[41, 42] electrostatic discharge,[43-45] and soluble fiber networks.[46] Of these techniques,

direct ink writing offers the greatest flexibility in materials selection and network design, as well as the potential for large-scale manufacturing.

1.1 Dissertation Scope

The primary aims of this dissertation are to create self-healing materials with embedded interpenetrating microvascular networks that exhibit repeated autonomic healing cycles and accelerated recovery of mechanical properties after damage. A complementary aim of this research is to create multinozzle printheads from embedded microvasculature for high-throughput printing of 3D architectures. We first develop dual fugitive inks with distinct temperature-dependent rheological profiles for direct-write assembly of interpenetrating microvascular networks. Self-healing materials with binary interpenetrating networks that house epoxy resin and hardener healing agents are mechanically tested to demonstrate their ability to repeatedly heal a single fracture location. Next, self-healing materials are designed and fabricated with a ternary interpenetrating network architecture. In the added network, a thermal fluid is circulated to accelerate healing reaction kinetics. Temperature effects on the bulk epoxy curing are systematically characterized and used to inform the observed accelerated healing in these novel self-healing constructs. Toward our complementary goal of scalable production of microvascular systems, we fabricate multinozzle printheads composed of hierarchical branching vascular networks that mimic those found in biological systems. These printheads, which conform to Murray's Law, are used for both single and multi-material deposition for additive manufacturing of micro-structured materials.

1.2 Dissertation Organization

In Chapter 2, the pertinent literature is reviewed with an emphasis on microvascular networks that includes their fabrication, application to autonomous healing, and routes for scalable manufacture. In Chapter 3, self-healing materials with binary interpenetrating microvascular networks are produced by direct writing of fugitive inks and their ability to repeatedly restore localized mechanical damage is demonstrated. In Chapter 4, thermally accelerated self-healing is demonstrated for materials with embedded ternary interpenetrating microvascular networks. In Chapter 5, the manufacture of multinozzle printheads based on Murray's Law is discussed and their application to high-throughput printing is demonstrated. Finally, the conclusions of my dissertation are summarized in Chapter 6.

1.3 References

1. C. D. Murray, *The Physiological Principle of Minimum Work*. Proceedings of the National Academy of Sciences, 1926, 12, p. 207-214.
2. K. A. McCulloh, J. S. Sperry, and F. R. Adler, *Water transport in plants obeys Murray's law*. Nature, 2003, 421, p. 939-942.
3. N. Charkoudian, *Skin Blood Flow in Adult Human Thermoregulation: How It Works, When It Does Not, and Why*. Mayo Clinical Proceedings, 2003, 78, p. 603-612.
4. J. W. Valvano, *Bioheat Transfer*, in *Encyclopedia of Medical Devices and Instrumentation*2005, Wiley. p. 1-10.
5. C. G. Crandall, T. E. Wilson, and K. C. Kregel, *Mechanisms and modulators of temperature regulation*. Journal of Applied Physiology, 2010, 109, p. 1219-1220.
6. P. Martin, *Wound Healing - Aiming for Perfect Skin Regeneration*. Science, 1997, 276, p. 75-81.
7. K. S. Toohey, *Microvascular networks for continuous self-healing materials*. Thesis (University of Illinois at Urbana-Champaign), 2007, p.
8. K. S. Toohey, C. J. Hansen, J. A. Lewis, S. R. White, and N. R. Sottos, *Delivery of two-part self-healing chemistry via microvascular networks*. Advanced Functional Materials, 2009, 19, p. 1399-1405.

9. K. S. Toohey, N. R. Sottos, J. A. Lewis, J. S. Moore, and S. R. White, *Self-healing materials with microvascular networks*. Nature Materials, 2007, 6, p. 581-585.
10. R. B. Oueslati, D. Therriault, and S. Martel, *PCB-integrated heat exchanger for cooling electronics using microchannels fabricated with the direct-write method*. IEEE Transactions on components and packaging technologies, 2008, 31, p. 869-874.
11. B. D. Kozola, L. A. Shipton, V. K. Natrajan, K. T. Christensen, and S. R. White, *Characterization of Active Cooling and Flow Distribution in Microvascular Polymers*. Journal of Intelligent Material Systems and Structures, 2010, 21, p. 1147-1156.
12. X. Wei, Y. Joshi, and M. K. Patterson, *Experimental and numerical study of a stacked microchannel heat sink for liquid cooling of microelectronic devices*. Transactions of the American Society of Mechanical Engineers, 2007, 129, p. 1432-1444.
13. J. T. Borenstein, E. J. Weinberg, B. K. Orrick, C. Sundback, M. R. Kaazempure-Mofrad, and J. P. Vacanti, *Microfabrication of Three-Dimensional Engineered Scaffolds*. Tissue Engineering, 2007, 13, p. 1837-1844.
14. N. W. Choi, M. Cabodi, B. Held, J. P. Gleghorn, L. J. Bonassar, and A. D. Stroock, *Microfluidic scaffolds for tissue engineering*. Nature Materials, 2007, 6, p. 908-915.
15. Y. Ling, J. Rubin, Y. Deng, C. Huang, U. Dmirci, J. M. Karp, and A. Khademhosseini, *A cell-laden microfluidic hydrogel*. Lab on a Chip, 2007, 7, p. 756-762.
16. M. P. MacDonald, G. C. Spalding, and K. Dholakia, *Microfluidic sorting in an optical lattice*. Nature, 2003, 426, p. 421-424.
17. D. Psaltis, S. R. Quake, and C. Yang, *Developing optofluidic technology through the fusion of microfluidics and optics*. Nature, 2006, 442, p. 381-386.
18. T. Thorsen, S. J. Maerkl, and S. R. Quake, *Microfluidic large-scale integration*. Science, 2002, 298, p. 580-584.
19. D. J. Beebe, J. S. Moore, J. M. Bauer, Q. Yu, R. H. Liu, C. Dvadoss, and B.-H. Jo, *Functional hydrogel structures for autonomous flow control inside microfluidic channels*. Nature, 2000, 404, p. 588-590.
20. D. Therriault, S. R. White, and J. A. Lewis, *Chaotic mixing in three-dimensional microvascular networks fabricated by direct-write assembly*. Nature Materials, 2003, 2, p. 265-272.
21. S. K. W. Dertinger, D. T. Chiu, N. L. Jeon, and G. M. Whitesides, *Generation of gradients having complex shapes using microfluidic networks*. Analytical Chemistry, 2001, 73, p. 1240-1246.
22. R. Ferrigno, A. D. Stroock, T. D. Clark, M. Mayer, and G. M. Whitesides, *Membraneless Vanadium Redox Fuel Cell Using Laminar Flow*. Journal of the American Chemical Society, 2002, 124, p. 12930-12931.
23. S. M. Mitrovski, L. C. C. Elliott, and R. G. Nuzzo, *Microfluidic Devices for Energy Conversion: Planar Integration and Performance of a Passive, Fully Immersed H2-O2 Fuel Cell*. Langmuir, 2004, 20, p. 6974-6976.

24. E. R. Choban, L. J. Markoski, A. Wieckowski, and P. J. A. Kenis, *Microfluidic fuel cell based on laminar flow*. Journal of Power Sources, 2004, 128, p. 54-60.
25. E. N. Brown, N. R. Sottos, and S. R. White, *Fracture testing of a self-healing polymer composite*. Experimental Mechanics, 2002, 42, p. 372-379.
26. M. R. Kessler, N. R. Sottos, and S. R. White, *Self-healing structural composite materials*. Composites: Part A, 2003, 34, p. 743-753.
27. J. D. Rule, E. N. Brown, N. R. Sottos, S. R. White, and J. S. Moore, *Wax-Protected Catalyst Microspheres for Efficient Self-Healing Materials*. Advanced Materials, 2005, 17, p. 205-208.
28. S. R. White, N. R. Sottos, P. H. Geubelle, J. S. Moore, M. R. Kessler, S. R. Sriram, E. N. Brown, and S. Viswanathan, *Autonomic healing of polymer composites*. Nature, 2001, 409, p. 794-797.
29. J. A. Lewis, *Direct ink writing of 3D functional materials*. Advanced Functional Materials, 2006, 16, p. 2193-2204.
30. J. A. Lewis and G. M. Gratson, *Direct writing in three dimensions*. Materials Today, 2004, 7, p. 32-39.
31. D. Therriault, R. F. Shepherd, S. R. White, and J. A. Lewis, *Fugitive inks for direct-write assembly of three-dimensional microvascular networks*. Advanced Materials, 2005, 17, p. 395-399.
32. D. Therriault, S. R. White, and J. A. Lewis, *Rheological behavior of fugitive organic inks for direct-write assembly*. Applied Rheology, 2007, 17, p. 10112-10120.
33. J. C. Love, J. R. Anderson, and G. M. Whitesides, *Fabrication of three-dimensional microfluidic systems by soft lithography*. Materials Research Society Bulletin, 2001, p. 523-528.
34. Y. Xia and G. M. Whitesides, *Soft Lithography*. Annual Review of Materials Science, 1998, 28, p. 153-184.
35. Y. Xia and G. M. Whitesides, *Soft Lithography*. Angewandte Chemie International Edition, 1998, 37, p. 550-575.
36. F. P. W. Melchels, J. Feijen, and D. W. Grijpma, *A Review on Stereolithography and its Applications in Biomedical Engineering*. Biomaterials, 2010, 31, p. 6121-6130.
37. R. B. Wicker, A. V. Ranade, and F. Medina, *Embedded micro-channel fabrication using line-scan stereolithography*. Assembly Automation, 2005, 25, p. 316-329.
38. C. Xia and N. X. Fang, *3D Microfabricated Bioreactor with Capillaries*. Biomedical Microdevices, 2009, 11, p. 1309-1315.
39. S. Kawata, H.-B. Sun, T. Tanaka, and K. Takada, *Finer features for functional microdevices*. Nature, 2001, 412, p. 697-698.
40. W. Zhou, S. M. Kuebler, K. L. Braun, T. Yu, J. K. Cammack, C. K. Ober, J. W. Perry, and S. R. Marder, *An efficient two-photon-generated photoacid applied to positive-tone 3D microfabrication*. Science, 2002, 296, p. 1106-1109.
41. T. M. Harms, M. J. Kazmierczak, and F. M. Gerner, *Developing convective heat transfer in deep rectangular microchannels*. International Journal of Heat and Mass Transfer, 1999, 20, p. 149-157.

42. D. Lim, Y. Kamotani, B. Cho, J. Mazumder, and S. Takayama, *Fabrication of microfluidic mixers and artificial vasculatures using a high-brightness diode-pumped Nd:YAG laser direct write method*. Lab on a Chip, 2003, 3, p. 318-323.
43. K. D. Behler and E. D. Wetzel, *Novel techniques for vascularization of structures: electrohydrodynamic viscous fingering and electrical treeing*. 27th Army Science Conference, 2008, p. 1-8.
44. J. Furuta, E. Hiraoka, and S. Okamoto, *Discharge figures in dielectrics by electron irradiation*. Journal of Applied Physics, 1966, 37, p. 1873-1878.
45. J.-H. Huang, J. Kim, N. Agrawal, A. P. Sudarsan, J. E. Maxim, A. Jayaraman, and V. M. Ugaz, *Rapid Fabrication of Bio-inspired 3D Microfluidic Vascular Networks*. Advanced Materials, 2009, 21, p. 3567-3571.
46. L. M. Bellan, S. P. Singh, P. W. Henderson, T. J. Porri, H. G. Craighead, and J. A. Spector, *Fabrication of an artificial 3-dimensional vascular network using sacrificial sugar structures*. Soft Matter, 2009, 5, p. 1354-1357.

CHAPTER 2

LITERATURE REVIEW

2.1 Introduction

This literature review begins with an overview of several fabrication techniques used to produce microvascular networks. Next, the application of microvascular networks to self-healing materials and thermal regulation is described. Finally, the design of multinozzle arrays for additive manufacturing is reviewed, with an emphasis on filamentary ink printing methods.

2.2 Microvascular Fabrication Techniques

Many biological systems depend on complex planar and three-dimensional (3D) microvascular networks for widespread fluid transport (Figure 2.1). Synthetic replication of embedded microvasculature requires fluid channels to form a pervasive network, be controllably patterned within a range of potential matrix materials, and, ideally, possess hierarchical branching architectures. In this section, we describe several microvascular fabrication techniques and discuss their relative merits and drawbacks.

Planar microvascular fabrication techniques include silicon-based lithography, soft lithography, and machining. In silicon-based lithography, a thin layer of a photoresist is patterned on a silicon wafer by selective illumination through a mask. After solvent removal of the uncured photoresist layer, chemical etching processes remove material beneath exposed regions. This removal is controllable at the micron length scale or smaller and has created intricate microchannel networks.[1-3] The technique, however,

requires expensive masks for high fidelity features and is best suited for channels of equal depth across the substrate.

In soft-lithography,[4-7] an elastomeric polymer, often poly(dimethylsiloxane), is molded upon a lithographically patterned photoresist on a silicon wafer. After curing, the flexible elastomer stamp is peeled from the substrate and subsequently bonded to a flat substrate, leaving patterned gaps in the form of microchannels (Figure 2.2).[8-14] The advantages of this technique include construction of complex interpenetrating networks and high fidelity microchannel features with nanometer-scale resolution.[15] The inherently planar nature of soft lithography requires that multiple layers are stacked, registered, and laminated to yield the desired 3D microvasculature.[8-10] In addition, a unique silicon wafer master is needed for each layer. Registration errors can occur during stacking or curing of these layers.[16, 17]

Machining, a subtractive manufacturing method, has been extensively used to create embedded microvascular networks on length scales of 10 μm or greater. A common approach to the fabrication of microfluidic networks is to directly mill grooves to create microchannels within a material surface.[18] The feature sizes tend to be on the order of 100 μm – 1 mm when machined by computer numeric control (CNC) milling[19] or on the order of 10 μm when created by electrical discharge machining (EDM).[20, 21] An extension of this route is to machine grooves, into which tubing is affixed with an adhesive.[22, 23] The grooved surfaces are subsequently mated to a flat substrate to create embedded microfluidic pathways. The advantages of machining include its ubiquity, materials flexibility, and the tailored creation of fluidic networks of varying

dimensions. Despite these advantages, the creation of multiple interpenetrating networks is difficult to machine.

To date, three-dimensional microvascular networks have been fabricated in both random and periodic patterns. One fabrication technique relies on material vaporization due to electrostatic discharge to create random, space-filling, three-dimensional microvascular networks.[24, 25] A dielectric material, such as poly(methyl methacrylate), is exposed to incident electrons at high energies (~3 MeV) to produce space charge densities of ~1 mC/cm^2.[26] Discharge of the stored electrons is initiated via puncturing the specimen surface with a grounded needle to produce highly branching structures that are often labeled 'Lichtenberg figures' or 'Lichtenberg trees'. These networks consist of larger trunk channels near the initiation point that branch to form smaller channels at the extremities (Figure 2.3). Prior to electron bombardment, a metal mask can cover areas where no branching is desired, thereby providing crude control over the network location.[26, 27] Whereas many microvascular techniques require lengthy fabrication times, creation of microvascular networks via vaporization is a nearly instantaneous process. However, there is minimal control over the channel diameters and multiple isolated networks are not possible.

The inclusion of soluble fiber networks provides another pathway to creating random, pervasive microfluidic networks.[28, 29] Mechanically spun sacrificial sugar structures have been embedded within a matrix material, such as poly(dimethyl siloxane) or polycaprolactone (PCL), and then removed via immersion in a miscible solvent.[28] Fluorescently-labeled blood cells exhibited unimpeded unidirectional flow throughout the vascularized polymer block. Electrospinning has also been utilized for fugitive

microchannel fabrication using sacrificial poly(ethylene oxide).[29] Though the microfluidic networks exhibit fine channel diameters (0.5-100 μm) and high capillary densities, the channel locations cannot be controllably patterned or reproduced.

Direct-write assembly methods, such as direct laser ablation, stereolithography, two-photon polymerization, and direct ink writing, enable the controlled patterning of 3D microfluidic networks. Direct laser ablation creates microchannels by material removal from a substrate surface via a focused laser beam.[30-32] Microchannel dimensions as small as ~30 μm[30] are defined by the duration and intensity of the incident laser pulses.[33] Similar to machining, the patterned features can be embedded when the substrate is mated to another surface. A primary drawback is that its planar nature requires lamination of multiple layers to create 3D networks.[1, 34-36] Laser ablation is also limited in its scalability due to the difficulty in increasing the laser patterning area.

Stereolithography is a layer-by-layer rapid prototyping technique that produces 3D structures within a photocurable resin.[37-39] A 3D CAD drawing is sectioned into planar slices, and a laser traces over each slice to induce selective photopolymerization. After each layer is cured, the specimen is lowered by a *z*-stage (usually in ~50 to 150 μm increments), and a new layer of photocurable resin is uniformly spread over the previous layer. This process is repeated until the entire 3D structure is complete. With suitable CAD designs, this technique can create microchannels[39] and multiple separate fluid networks[38, 40, 41] (Figure 2.4). An advantage of stereolithography is the near-arbitrary fabrication of features, provided that they are physically supported by previously deposited layers. The features can be printed with a 10 μm resolution with a 1 μm *z*-step.[42] However, to reach this resolution requires lengthy fabrication times,

even when expedited through the use of digital projection photo masks,[43, 44] and is limited to specimen sizes of 35 mm^3 or less.[42] The technique also requires a photopolymerizable resin, which limits materials selection and can be costly.[45]

Two-photon polymerization (TPP) is similar to stereolithography in that it requires laser beam excitation to polymerize material.[46-50] Monomeric materials suitable for TPP processes have a non-linear dependence on radiation intensity so that polymerization occurs only in regions of high photon flux. Each region, known as a voxel, has a volume on the order of the cube of the laser wavelength, which allows TPP to produce fine feature sizes in three dimensions.[47] Over small total volumes of 100 μm x 100 μm x 20 μm,[48] TPP can produce 3D networks with separated microfluidic channels (Figure 2.5). However, large area patterning of 3D specimens is limited by the illumination volume on TPP systems and the line-scan speeds (~50 μm/s[48]).

Direct ink writing is a fabrication technique in which viscoelastic inks are extruded through a fine nozzle to pattern 3D structures. The nozzle, mounted on a 3-axis, motion-controlled stage directs the deposition of filamentary structures in a layer-by-layer approach on a substrate (Figure 2.6). To produce microvasculature, a fugitive organic ink[51, 52] is patterned. A suitable fugitive ink must possess a shear yield behavior for extrusion at reasonable pressures and a high modulus plateau for spanning large distances with minimal deformation. The patterned fugitive ink structures are infiltrated with a material, such as a two-part epoxy or photopolymer, that is subsequently cured to form a solid matrix.[53, 54] Finally, the fugitive ink is liquefied and removed from the matrix with application of modest vacuum to produce an interconnected, 3D microchannel network.[54-56] Fugitive ink filament diameters ranging from tens to thousands of

microns can be deposited.[53] This process can be scaled to create parts that exceed 1 m^2 in area and thicknesses of at least several centimeters.

2.3 Microvascular Self-Healing Materials

An autonomic material exhibits a specified response to an external stimulus in the absence of outside intervention.[57] The external stimulus can be mechanical,[58-61] electrical,[62] entropic,[63] optical,[64-66], thermal,[67] or pressure-based,[68, 69] with mechanical recovery a commonly desired response. A decade ago, White and coworkers[58] pioneered a novel microcapsule-based self-healing system composed of microencapsulated dicyclopentadiene (DCPD) and Grubbs' catalyst particles dispersed in a polymer matrix (Figure 2.7a). Upon mechanical loading and subsequent crack propagation, microcapsules within the crack propagation zone rupture and release DCPD monomer. The DCPD wicks into the crack plane via capillary forces, where it undergoes polymerization upon contact with Grubbs' catalyst in the crack plane. After healing for 48 hr at room temperature, mechanical testing of these specimens show up to 90.3% fracture toughness recovery (Figure 2.7c).[59] While this research provided a seminal advance in self-healing materials, the compartmentalized design limits healing to a single event in a given damage region due to localized depletion of the DCPD healing agent.

To overcome that design limitation, Toohey *et al*.[70] adopted a biomimetic coating/substrate architecture analogous to human skin. Because the human dermal layer serves as a protective barrier, it must be able to be rapidly and repeatedly healed when damaged (Figure 2.8a). Healing is accomplished by continuous fluid transport from the underlying microvascular network to the damage site. The synthetic analog to this

biological system consists of a brittle epoxy coating on a flexible polymer substrate in which a single interconnected microvascular network is embedded. Direct ink writing is used to create the microvascular network, which consists of 200 μm channels patterned in a face-centered tetragonal geometry with a 2 mm spacing and overall specimen dimensions of 45 mm x 7 mm x 10 mm. The network serves as a reservoir for the healing fluid, while the catalyst component is incorporated into the coating. Toohey *et al*.[70] used the same chemistry as the microcapsule-based system, with DCPD filling the microvascular network and Grubbs' catalyst dispersed in the coating material prior to curing. The samples are tested in 4-point bending to induce fracture events in the coating, which are recorded by an acoustic emission sensor (Figure 2.8b). The resulting cracks propagate through the brittle coating toward the microchannel openings at the coating-substrate interface, where they terminate their propagation due to the increased fracture toughness of the substrate. The underlying microvascular network supplies the crack with an abundance of healing fluid (DCPD) that locally polymerizes upon contact with the exposed Grubbs' catalyst (Figure 2.8c). After healing for 48 hr at 30°C, the same crack is reopened, and any recovery of the coating fracture toughness is recorded. The microvascular-based system exhibits repeated healing of a single crack location for up to 7 cycles, with up to 70% recovery of the original fracture toughness (Figure 2.8d). Beyond that point, no additional healing is observed due to preferential depletion of accessible Grubbs' catalyst within the fracture region. While the change from microcapsule to microvascular delivery of the same DCPD healing agent enables repeated healing, the incorporation of Grubbs' catalyst in a discrete, solid form prevents truly unlimited healing.

To further extend autonomic healing, an epoxy-based system composed of two reactive fluids was pursued so that neither healing agent is depleted relative to the other. As a first demonstration, Toohey *et al*.[71, 72] showed that a single interconnected microfluidic network could be subdivided into a series of sub-networks, each of which is sequentially filled with liquid epoxy resin and hardener (Figure 2.9a-c). Several epoxy resins and hardeners were tested for compatibility with the substrate material as well as rapid and complete curing upon mixing. In this approach, a single microfluidic network is printed, which is composed of 330 μm diameter channels with a lateral spacing of 3.3 mm in a face-centered tetragonal (FCT) geometry. Next, the microchannel network is infiltrated with a photopolymerizable epoxy fluid that is selectively photopolymerized to divide the single network into 4 smaller networks, which are filled with the epoxy resin and hardener in an alternating fashion. After the coating fractures, the resulting crack intersects the sub-networks, and both resin and hardener are wicked into the crack plane, where they react. Mechanical testing demonstrates that healing is extended beyond 7 cycles, although consistent healing is not observed for each cycle (Figure 2.9d). However, they did find that slight mechanical mixing (50 cycles at 20 μm displacement) enhances the recovery of mechanical properties over multiple healing cycles. This design improves on previous results by allowing new, inexpensive healing chemistries to be explored. However, the sub-network design requires healing agents to diffusively mix over long distances to fully react.

While the above examples are directly relevant to this dissertation, alternate methods have also been used to incorporate microvascular networks into composite structures. Williams *et al*.[22] created a sandwich composite with a vascular network in the foam

core. A polymethacrylamide closed-cell foam was machined with parallel channels 2 mm wide and 2.5 mm deep. Poly(vinyl chloride) tubing with a 2.5 mm external diameter, 1.5 mm internal diameter was situated within the machined channels with adhesive. To provide access to the core surface, 1.5 mm holes were drilled into the core to intersect the embedded tubing (Figure 2.10a). The sandwich was completed by bonding composite skins of pre-impregnated E-glass to the foam surface. Mechanical tests of control specimens demonstrated no decrease in stress at failure due to the presence of the underlying microvasculature. Initial tests of samples filled with pre-mixed two-part epoxy demonstrated full recovery of healing. However, repeated healing was not possible because the channels were filled with polymerized material. In a related experiment, new samples were tested that contained alternating tubes filled with either epoxy resin or hardener (Figure 2.10b). These were attached to syringes that were elevated above the networks in order to pressurize the fluid within the networks. Mechanical loading after fracture and healing for 36 hr at 20°C yielded a bimodal distribution in which half the specimens fully recovered and the other half displayed no healing. Premixed epoxy containing red or blue pigments were infiltrated into alternating channels designed to have a 2:1 ratio of surface outlets. Visual inspection after curing showed an average ratio of 2.3:1 for the components covering an average area fraction of 0.67 of the impact damage zone (Figure 2.10c).

2.4 Microvascular Thermal Regulation

Thermal regulation of materials via embedded microvascular networks is an area of growing importance. The heat transfer coefficient (h) for a microfluidic channel under laminar flow conditions is given by:

$$h = \frac{k_f Nu_\infty}{2R}, \tag{2.4}$$

where k_f is the thermal conductivity of the fluid, Nu_∞ is the dimensionless Nusselt number (usually 3-9), and $2R$ is the characteristic width of the microchannel.[73] The heat transfer coefficient is inversely proportional to the width ($2R$) so thermal transfer is enhanced at the microscale. As a result, microchannel heat transfer coefficients can be orders of magnitude greater than their macroscale counterparts.[74]

Numerous active cooling applications take advantage of microfluidic heat transfer. For example, microfluidics have been investigated for on-chip thermal management of microelectronic devices[74-77] to support elevated thermal loads from increased processing speeds. Batteries[78] and fuel cells[79, 80] may benefit from active thermal management to limit maximum temperatures and increase uniformity of the temperature distribution, as well as reduce variability in reactant delivery to the ionic transport membrane. In aerospace applications, laminar flow control (LFC), in which microfluidic networks cool the wings and fuselage for high-velocity, steady aerodynamic profiles, is expected to reduce drag and increase fuel economy.[81-84] Niche active heating applications also exist, including micro-Peltier junction heating for heat transfer[85] and microchip polymerase chain reaction (PCR) processing for rapid lab-on-a-chip DNA processing.[86]

2.4.1 Direct Ink Writing of Thermal Regulation Microvascular Networks

Most examples of active microfluidic thermal management are fabricated by wet[86] or dry etching,[74, 75, 86] or by soft lithography.[85] Recently, direct ink writing has been employed to fabricate microvascular networks for thermal management. The first demonstration of this concept is on printed circuit boards (PCBs) where standard silicon etching techniques are not applicable. Fugitive ink features were directly patterned on a commonly used PCB (copper/FR4 PCB) (Figure 2.11a-b).[87] The printed features are covered with epoxy and, after curing, a second PCB is attached with epoxy to produce a sandwich structure with the fugitive ink in the core (Figure 2.11c). After removal of the fugitive ink, distilled water at 5°C is flowed through the microchannels under laminar conditions ($Re \leq 178$) to determine the thermal efficiency of the micro-heat exchanger. The architecture demonstrated heat removal in excess of 0.8 W cm^{-2} for flow rates of 3 mL min^{-1} (Figure 2.11d). The large pressure drop precluded higher flow rates, but analysis shows the reduced viscosity of water at elevated temperatures would permit significantly higher flow rates under the same applied pressures.

Kozola and coworkers have investigated the use of direct ink writing to fabricate microvascular networks in polymeric thermal fins designed to conduct and dissipate heat from a high-temperature location.[88] 2D samples with parallel channels were created with either 12 channels (410 μm diameter, 1600 μm center to center spacing) or 24 channels (200 μm diameter, 800 μm center to center spacing) (Figure 2.12a). A 3D sample geometry contained three interconnected layers with each layer containing 24 channels (200 μm diameter, 800 μm center to center spacing) orthogonal to the neighboring layer(s). The fin thermal profile matches the theoretical solution in the

absence of flow. As flow initiates, the static mean field temperature drops from 60°C to 48°C at flow of 1 mL min^{-1}. Further increases in the flow rate to 10 ml min^{-1} cools the fin to 30°C (Figure 2.12b). The effective heat transfer coefficient, h_{eff}, for a flow rate of 10 mL min^{-1} is 198 W m^{-2} K^{-1}, which is a 53-fold increase as compared to h_{eff} for the case when no flow is present. Microscopic particle image velocimetry (μ-PIV) reveals that the average flow rate within all channels is relatively even (Figure 2.12c). Moreover, the fluid flow distribution becomes more uniform at higher flow rates and within the 3D geometry as compared to the 2D parallel features (Figure 2.12d).

2.4.2 Temperature Effects on Self-Healing Kinetics

Recent studies with self-healing systems have indicated that temperature can have a strong effect on mechanical restoration. Kessler *et al*.[89] measured the effect of temperature on the interlaminar fracture toughness in a microcapsule-based self-healing composite. To determine the influence of temperature on final healing properties, specimens were allowed to heal at either room temperature or 80°C. Specimens cured at room temperature had an average healing efficiency of 38%, while those cured at 80°C exhibited nearly a two-fold enhancement in healing efficiency.

Recently, Kirkby *et al*.[69] produced a tapered double cantilever beam (TDCB) specimen with shape-memory alloy (SMA) wires across the damaged interface (Figure 2.13a). Grubbs' catalyst microspheres are embedded in the matrix, while DCPD monomer is injected into the crack plane. Upon activation of the SMA wires via electrical resistive heating, the crack opening is reduced in size and the specimen is heated to 80°C through resistive heating of the SMA wires. This compression and heating results in a near doubling of the healing plateau load from 38 to 61 N. To

separate the influence of reduced crack opening thickness and resistive heating, the use of non-SMA wires was investigated. This experiment produces resistive heating, while avoiding compression of the fracture region. In this case, a healing plateau of 56N was observed, indicating that a significant fraction of fracture toughness recovery is achieved solely due to the elevated temperature conditions (Figure 2.13b). In subsequent work, similar results were observed for self-healing materials that contained encapsulated DCPD microspheres.[68]

Self-healing systems that do not incorporate microcapsules also benefit from heating. For example, fiber-reinforced composites with embedded hollow glass fibers that contain epoxy resin and hardener were heated to 90-100°C for 1-2 hr after fraction to facilitate liquid infiltration and curing in the crack plane.[90, 91] An alternate approach based on thermally a re-mendable polymer exploits the Diels-Alder reaction to produce healing.[67] The repair of the fracture plane relies on a crosslinking reaction that is activated and enhanced at temperatures greater than 120°C (Figure 2.14). Using this system, a single fracture region could be healed multiple times; however, a sharp reduction in healing efficiency occurred between the second and third heal cycles. Other systems, including thermoplastic particle inclusions[92] or epoxies experiencing chain rearrangement,[93] also benefit from thermally enhanced healing.

2.5 Multinozzle Printheads

Multiple nozzle arrays, or printheads, are of interest for myriad additive fabrication techniques, as they rapidly decrease printing times. To date, multinozzle arrays have

been developed for applications that include tissue engineering,[94] non-woven fiber mattes,[95] and microstructured ceramics.[96]

2.5.1 Fabrication of Multinozzle Printheads

Inkjet printing commonly employs multinozzle printheads.[97] To produce large volumes of highly reproducible printheads, commercial inkjet printing relies on silicon wafer and thin film manufacturing techniques.[98] The sequential fabrication steps are numerous, with 17 separate process flow steps in Hewlett-Packard's ThinkJet disposable printheads.[99] Briefly, a silicon substrate is covered with nitride and oxide layers, which are patterned and etched to produce addressable transistors, which are controlled with metallization of electrical interconnects. The surface is coated with a tantalum barrier to resist cavitation damage to the printhead from ink pressure waves. Finally, an ink barrier adheres the nozzle faceplate and defines the fluid flow pathways (Figure 2.15a). These multinozzle printheads typically consist of ~100 – 500 nozzles.[97]

The exact printhead design depends on which ink ejection method, either continuous inkjet printing (CIP) or drop on demand (DOD) printing,[100] is utilized. CIP is achieved with pressurized fluid continuously ejected from a nozzle that is held at a potential relative to the substrate, i.e. the droplets become electrically charged. DOD printing, by contrast, ejects single droplets based on a pressure wave induced within individual nozzles by either thermal or piezoelectric means (Figure 2.15b-c). The thermal method contains a thin-film resistive heating element that forms a bubble within microseconds by vaporizing ink near the nozzle, which subsequently collapses after heating ends. This expansion and collapse creates a pressure wave that ejects a droplet and feeds ink from the reservoir to the nozzle location. In piezoelectric-based

pressurization, a thin-film piezoelectric transducer located behind the nozzle generates a direct mechanical wave.

Silicon fabrication techniques are employed for electrohydrodynamic jetting nozzles (Figure 2.16a).[101] Three nozzles are created in an SOI silicon wafer by patterning an etch design followed by a buffered oxide etch. A metallic coating is added to individually address each nozzle. To reduce the wetting behavior of the ink, the final multinozzle array is coated in Teflon®. The nozzles have a final center-to-center spacing of 2.1 mm and the inner diameter of each nozzle is 360 μm.

Dip Pen Nanolithography (DPN) is a direct write technique that can pattern molecules by rastering a cantilevered silicon tip over a 2D substrate with sub-100 nm resolution.[102] Massively scaling DPN with passive tip arrays permits parallel patterning of molecules over centimeter-length distances.[103] Commercial arrays of 26 AFM tips have been used, but contain fixed spacings of 30 μm.[104] 500 tip arrays are also demonstrated using fabrication in silicon wafers. An oxide layer is thermally grown on a silicon wafer and then patterned to retain small SiO_2 squares after etching. Following anisotropic silicon etching, pyramidal silicon tips are created and coated with a silicon nitride layer. Further etching creates cantilevers for a massively parallel deposition. Using similar fabrication techniques, 2D cantilever arrays of up to 1.2 million tips have been patterned on 3 inch wafers (Figure 2.17a).[105] Multiple tip arrays with individual tip actuation is achieved by either thermoelectric means, where resistive heating actuates a bimetallic cantilever[106, 107] or electrostatic means, where a secondary electrode applies an electric field to raise or lower the cantilever tip.[108]

Hybrid fabrication techniques that incorporate polymeric substrates have also been demonstrated in context of DPN. In hard-tip, soft-spring lithography (HSL), an SOI wafer is attached to a PDMS substrate (Figure 2.17b).[109] Photolithography is used to define tip locations, which remain on the PDMS after preferential etching of the surrounding silicon material. Up to 1 cm^2 HSL arrays with 4750 tips are created by this method. Another DPN variant is Polymer Pen Lithography (PPL), which consists of fully polymeric tips that are fabricated via soft lithography. Liquid PDMS is poured over a silicon master containing pyramidal depressions and a glass substrate is attached for global rigidity (Figure 2.17c).[110] Upon curing, an array of 11 million individual tips is produced, each with a tip radius of 70±10 nm.

2.5.2 High Throughput Fabrication via Multinozzles

Inkjet multinozzle arrays have been used to deposit ceramic inks through piezoelectric printheads.[96] A Xaar XJ500 monochrome printhead, which consists of 500 nozzles with 50 μm orifices uniformly spaced over an array length of 70 mm, has a minimum resolution of 140 μm per feature (i.e., 180 dpi) at speeds up to 500 mm s^{-1}. The ceramic ink is composed of zirconia filtered with a 5 μm filter and suspended at 20 vol% in an isopropyl alcohol/octane solvent mixture. In order to print with the piezoelectric nozzles, the viscosity must be tuned within the range of 2.7 to 10 mPa-s. To build up appreciable thicknesses, 200 to 800 layers must be deposited to form feature heights of ~500 μm. Though the technique speeds the deposition of ceramics on the microscale, there are numerous disadvantages to this system, including low ceramic volume fraction, droplet spreading on the substrate, numerous deposition passes for feature cross-sections of low aspect ratio, and fracture due to large linear shrinkage during sintering.

A multi-material inkjet multinozzle system has been used to co-deposit a zirconia and a carbon-based ink.[111] Though the 4 piezoelectric print nozzles represents a drastic reduction in the number of nozzles as compared to the XJ500 printhead, the resolution is increased to ≈90 μm (288 dpi). Due to the low solids loading in the ink, 400 layers of material must be deposited per 100 μm of sintered material. Each production run creates 15 parts, each 1.5 x 4.2 x 0.3 mm in dimension. Though each part is modest in size, the large number of layers requires a fabrication time of greater than 11 hours. Moreover, the low ink viscosity produces poor feature fidelity.

To overcome these limitations, high-viscosity fluids (3000 mPa-s) have recently been ejected from custom-designed silicon multinozzle printheads.[112] Piezoelectric actuation rates of up to 1 MHz were used to produce resonant acoustic waves for reproducible droplet ejection out of 400 nozzles. Fluids ejected include water-glycerol solutions and photopolymer urethane resin. Though the viscosity envelope is increased for multinozzle deposition, surface tension considerations require elevated temperatures that could cause preferential evaporation. Moreover, excessive heating of the multi-nozzle array occurs during photopolymer resin ejection and requires lowering the fixture into a controlled temperature bath.

Multinozzle electrohydrodynamic jetting has printed silver inks for conductive features.[101] Syringes are filled with a nanocolloid silver-based ink and separate syringe pumps are used to feed each nozzle. The relatively large separation between nozzles permits simultaneous operation of all or a subset of the three nozzles with a single grounded substrate (Figure 2.16c-d). However, simulations indicate that bringing the nozzles into closer proximity with each other would lead to instabilities in the

deposition. Modeling by Theron *et al*.[113] indicate nozzles spaced 1 cm apart will have electrospinning jets that strongly interact. Experiments demonstrate that neighboring jets strongly influence each other via electric forces and produce non-uniform fiber mattes. Electrospinning multi-nozzles have been fabricated with large arrays (greater than 10 x 10) and significantly smaller (5 μm) nozzle openings, though actuation of only one nozzle was demonstrated in the experiments.[114]

Dip pen nanolithography has been used in a wide range of direct-write applications,[103] including screening for viruses,[115] local enzymatic reactions,[116] thin film polymer films,[117] and carbon nanotube patterning.[118] One notable DPN multinozzle application includes the patterning of phospholipids with 100 nm resolution on hydrophobic (e.g., polystyrene) to hydrophilic (e.g., silicon) substrates using 55,000 tips.[119] Parallel writing of two different phospholipid inks opens the possibility of biological membrane mimics of multiple chemistries.

Hard-tip, soft-spring lithography (HSL) with 1 cm^2 arrays containing 2,500 to 10,000 tips are used to print poly(ethylene glycol) and 16-mercaptohexadecanoic acid (MHA) on a hexamethyldisilazane-coated silicon wafer.[109] Tips do not deform in contact with the substrate surface, but the PDMS substrate compensates for any tip height or leveling mismatches. Tip arrays coated with gold and attached to a voltage source were able to selectively remove MHA from a substrate in holes only ~270 nm in diameter.

Polymer pen lithography (PPL) has used arrays of 15,000 or 28,000 tips to pattern 16-mercaptohexadecanoic acid in ethanol on a gold substrate.[110] Subsequent etching of the exposed gold created 1 μm diameter, 25 nm height features on a silicon substrate. Adjustment of the applied force of the deformable tips on the substrate enables control

over the feature size, which permits faster writing of wide features by force application instead of further rastering.

2.6 Summary

In this chapter, we have reviewed the fabrication of synthetic microvasculature, the application of microvasculature to benefit self-healing materials and to regulate the temperature of materials, and the use of multinozzle printheads for high throughput printing. Repeated microvascular self-healing, however, remains constrained by interpenetrating microvascular network design and fabrication, a limitation that is addressed in Chapter 3 by improved direct ink write techniques. The characteristically slow self-healing cure kinetics of previous microvascular self-healing can be accelerated via incorporation of microfluidic heating networks, which is discussed in Chapter 4. Finally, Chapter 5 demonstrates the deposition of concentrated gels for additive manufacturing contexts by embedding microvascular networks into multinozzle printheads.

2.7 References

1. T. M. Harms, M. J. Kazmierczak, and F. M. Gerner, *Developing convective heat transfer in deep rectangular microchannels*. International Journal of Heat and Mass Transfer, 1999, 20, p. 149-157.
2. J. Voldman, M. L. Gray, and M. A. Schmidt, *Microfabrication in Biology and Medicine*. Annual Review of Biomedical Engineering, 1999, 1, p. 401-425.
3. J. P. Camp, T. Stokol, and M. L. Shuler, *Fabrication of a multiple-diameter branched network of microvascular channels with semi-circular cross-sections using xenon difluoride etching*. Biomedical Microdevices, 2008, 10, p. 179-186.
4. Y. Xia and G. M. Whitesides, *Soft Lithography*. Annual Review of Materials Science, 1998, 28, p. 153-184.
5. Y. Xia and G. M. Whitesides, *Soft Lithography*. Angewandte Chemie International Edition, 1998, 37, p. 550-575.

6. J. C. Love, J. R. Anderson, and G. M. Whitesides, *Fabrication of three-dimensional microfluidic systems by soft lithography*. Materials Research Society Bulletin, 2001, p. 523-528.
7. J. A. Rogers and R. G. Nuzzo, *Recent Progress in Soft Lithography*. Materials Today, 2005, 8, p. 50-56.
8. J. R. Anderson, D. T. Chiu, R. J. Jackman, O. Cherniavskaya, J. C. McDonald, H. Wu, S. H. Whitesides, and G. M. Whitesides, *Fabrication of Topologically Complex Three-Dimensional Microfluidic Systems in PDMS by Rapid Prototyping*. Analytical Chemistry, 2000, 72, p. 3158-3164.
9. D. T. Chiu, N. L. Jeon, S. Huang, R. S. Kane, C. J. Wargo, I. S. Choi, D. E. Ingber, and G. M. Whitesides, *Patterned deposition of cells and proteins onto surfaces by using three-dimensional microfluidic systems*. Proceedings of the National Academy of Sciences, 2000, 97, p. 2408-2413.
10. H. Wu, T. W. Odom, D. T. Chiu, and G. M. Whitesides, *Fabrication of complex three-dimensional microchannel systems in PDMS*. Journal of the American Chemical Society, 2003, 125, p. 554-559.
11. A. C. Siegel, D. A. Bruzewicz, D. B. Weibel, and G. M. Whitesides, *Microsolidics: fabrication of three-dimensional metallic microstructures in poly(dimethylsiloxane)*. Advanced Materials, 2007, 19, p. 727-733.
12. J. Melin and S. R. Quake, *Microfluidic large-scale integration: the evolution of design rules for biological automation*. Annual Review of Biophysical and Biomolecular Structures, 2007, 36, p. 213-231.
13. T. Thorsen, S. J. Maerkl, and S. R. Quake, *Microfluidic large-scale integration*. Science, 2002, 298, p. 580-584.
14. R. F. Ismagilov, J. M. K. Ng, P. J. A. Kenis, and G. M. Whitesides, *Microfluidic arrays of fluid-fluid diffusional contacts as detection elements and combinatorial tools*. Analytical Chemistry, 2001, 73, p. 5207-5213.
15. B. D. Gates and G. M. Whitesides, *Replication of Vertical Features Smaller than 2 nm by Soft Lithography*. Journal of the American Chemical Society, 2003, 125, p. 14986-14987.
16. C. Moraes, Y. Sun, and C. A. Simmons, *Solving the shrinkage-induced PDMS alignment registration issue in multilayer soft lithography*. Journal of Micromechanics and Microengineering, 2009, 19, p. 065015: 065011-065016.
17. S. W. Lee and S. S. Lee, *Shrinkage ratio of PDMS and its alignment method for the wafer level process*. Microsystem Technologies, 2008, 14, p. 205-208.
18. X. Peng and B. Wang, *Forced-Convection and Flow Boiling Heat-Transfer for Liquid Flowing through Microchannels*. International Journal of Heat and Mass Transfer, 1993, 36, p. 3421-3427.
19. P.-S. Lee, S. V. Garimella, and D. Liu, *Investigation of heat transfer in rectangular microchannels*. International Journal of Heat and Mass Transfer, 2005, 48, p. 1688-1704.
20. M. Murali and S. H. Yeo, *Rapid Biocompatible Micro Device Fabrication by Micro Electro-Discharge Machining*. Biomedical Microdevices, 2004, 6, p. 41-45.

21. S.-T. Chen, *Fabrication of high-density micro holes by upward batch micro EDM*. Journal of Micromechanics and Microengineering, 2008, 18, p. 085002:085001-085009.
22. H. R. Williams, R. S. Trask, and I. P. Bond, *Self-Healing Composite Sandwich Structures*. Smart Materials and Structures, 2007, 16, p. 1198-1207.
23. H. R. Williams, R. S. Trask, and I. P. Bond, *Self-Healing Sandwich Panels: Restoration of Compressive Strength After Impact*. Composites Science and Technology, 2008, 68, p. 3171-3177.
24. K. D. Behler and E. D. Wetzel, *Novel techniques for vascularization of structures: electrohydrodynamic viscous fingering and electrical treeing*. 27th Army Science Conference, 2008, p. 1-8.
25. J.-H. Huang, J. Kim, N. Agrawal, A. P. Sudarsan, J. E. Maxim, A. Jayaraman, and V. M. Ugaz, *Rapid Fabrication of Bio-inspired 3D Microfluidic Vascular Networks*. Advanced Materials, 2009, 21, p. 3567-3571.
26. J. Furuta, E. Hiraoka, and S. Okamoto, *Discharge figures in dielectrics by electron irradiation*. Journal of Applied Physics, 1966, 37, p. 1873-1878.
27. M. D. Noskov, A. S. Malinovski, C. M. Cooke, K. A. Wright, and A. J. Schwab, *Experimental study and simulation of space charge stimulated discharge*. Journal of Applied Physics, 2002, 92, p. 4926-4934.
28. L. M. Bellan, S. P. Singh, P. W. Henderson, T. J. Porri, H. G. Craighead, and J. A. Spector, *Fabrication of an artificial 3-dimensional vascular network using sacrificial sugar structures*. Soft Matter, 2009, 5, p. 1354-1357.
29. L. M. Bellan, E. A. Strychalski, and H. G. Craighead, *Nanochannels fabricated in polydimethylsiloxane using sacrificial electrospun polyethylene oxide nanofibers*. Journal of Vacuum Science and Technology B, 2008, 26, p. 1728-1731.
30. D. Gomez, I. Goenaga, I. Lizuain, and M. Ozaita, *Femtosecond laser ablation for microfluidics*. Optical Engineering, 2005, 45, p. 051105:051101-051108.
31. D. Lim, Y. Kamotani, B. Cho, J. Mazumder, and S. Takayama, *Fabrication of microfluidic mixers and artificial vasculatures using a high-brightness diode-pumped Nd:YAG laser direct write method*. Lab on a Chip, 2003, 3, p. 318-323.
32. D. H. Kam and J. Mazumder, *Three-dimensional biomimetic microchannel network by laser direct writing*. Journal of Laser Applications, 2008, 20, p. 185-191.
33. H. Qi, T. Chen, L. Yao, and T. Zuo, *Micromachining of microchannel on the polycarbonate substrate with CO2 laser direct-writing ablation*. Optics and Lasers in Engineering, 2009, 47, p. 594-598.
34. B. Dang, M. S. Bakir, D. C. Sekar, C. R. King, and J. D. Meindl, *Integrated Microfluidic Cooling and Interconnects for 2D and 3D Chips*. IEEE Transactions on Advanced Packaging, 2010, 33, p. 79-87.
35. C. R. King, D. Sekar, M. S. Bakir, B. Dang, J. Pikarsky, and J. D. Meindl, *3D Stacking of Chips with Electrical and Microfluidic I/O Interconnects*. 2008 Electronic Components and Technology Conference, 2008, p. 1-7.
36. B. K. Paul, P. Kwon, and R. Subramanian, *Understanding Limits on Fin Aspect Ratios in Counterflow Microchannel Arrays Produced by Diffusion Bonding*. Journal of Manufacturing Science and Engineering, 2006, 128, p. 977-983.

37. F. P. W. Melchels, J. Feijen, and D. W. Grijpma, *A Review on Stereolithography and its Applications in Biomedical Engineering*. Biomaterials, 2010, 31, p. 6121-6130.
38. C. Xia and N. X. Fang, *3D Microfabricated Bioreactor with Capillaries*. Biomedical Microdevices, 2009, 11, p. 1309-1315.
39. R. B. Wicker, A. V. Ranade, and F. Medina, *Embedded micro-channel fabrication using line-scan stereolithography*. Assembly Automation, 2005, 25, p. 316-329.
40. H.-W. Kang, I. H. Lee, and D.-W. Cho, *Development of an assembly-free process based on virtual environment for fabricating 3D microfluidic systems using microstereolithography technology*. Transactions of the American Society of Mechanical Engineering, 2004, 126, p. 766-771.
41. K. Arcaute, B. K. Mann, and R. B. Wicker, *Stereolithography of three-dimensional bioactive poly(ethylene glycol) constructs with encapsulated cells*. Annals of Biomedial Engineering, 2006, 34, p. 1429-1441.
42. S. Yang, K.-F. Leong, Z. Du, and C.-K. Chua, *The Design of Scaffolds for Use in Tissue Engineering. Part II. Rapid Prototyping Techniques*. Tissue Engineering, 2002, 8, p. 1-11.
43. C. Sun, N. Fang, D. M. Wu, and X. Zhang, *Projection micro-stereolithography using digital micro-mirror dynamic mask*. Sensors and Actuators A, 2005, 121, p. 113-120.
44. A. Limaye and D. Rosen, *Quantifying Dimensional Accuracy of a Mask Projection Micro Stereolithography System*. Proceedings of the Fifteenth Solid Freeform Fabrication Symposium, 2004, p.
45. D. T. Pham and R. S. Gault, *A comparison of rapid prototyping technologies*. International Journal of Machine Tools and Manufacture, 1998, 38, p. 1257-1287.
46. D. Yang, S. J. Jhaveri, and C. K. Ober, *Three-dimensional microfabrication by two-photon lithography*. Materials Research Society Bulletin, 2005, 30, p. 976-982.
47. S. Kawata, H.-B. Sun, T. Tanaka, and K. Takada, *Finer features for functional microdevices*. Nature, 2001, 412, p. 697-698.
48. W. Zhou, S. M. Kuebler, K. L. Braun, T. Yu, J. K. Cammack, C. K. Ober, J. W. Perry, and S. R. Marder, *An efficient two-photon-generated photoacid applied to positive-tone 3D microfabrication*. Science, 2002, 296, p. 1106-1109.
49. S. M. Keubler, K. L. Braun, W. Zhou, J. K. Cammack, T. Yu, C. K. Ober, S. R. Marder, and J. W. Perry, *Design and application of high-sensitivity two-photon intiators for three-dimensional microfabrication*. Journal of Photochemistry and Photobiology A: Chemistry, 2003, 158, p. 163-170.
50. C. A. Coenjarts and C. K. Ober, *Two-Photon Three-Dimensional Microfabrication of Poly(Dimethylsiloxane) Elastomers*. Chemistry of Materials, 2004, 16, p. 5556-5558.
51. D. Therriault, S. R. White, and J. A. Lewis, *Rheological behavior of fugitive organic inks for direct-write assembly*. Applied Rheology, 2007, 17, p. 10112-10120.

52. J. Bruneaux, D. Therriault, and M. C. Heuzey, *Micro-extrusion of organic inks for direct-write assembly*. Journal of Micromechanics and Microengineering, 2008, 18, p. 1-11.
53. D. Therriault, R. F. Shepherd, S. R. White, and J. A. Lewis, *Fugitive inks for direct-write assembly of three-dimensional microvascular networks*. Advanced Materials, 2005, 17, p. 395-399.
54. D. Therriault, S. R. White, and J. A. Lewis, *Chaotic mixing in three-dimensional microvascular networks fabricated by direct-write assembly*. Nature Materials, 2003, 2, p. 265-272.
55. J. A. Lewis and G. M. Gratson, *Direct writing in three dimensions*. Materials Today, 2004, 7, p. 32-39.
56. J. A. Lewis, *Direct ink writing of 3D functional materials*. Advanced Functional Materials, 2006, 16, p. 2193-2204.
57. S. K. Ghosh, ed. *Self-healing materials: Fundamentals, design strategies, and applications*. 2009, Wiley-VCH.
58. S. R. White, N. R. Sottos, P. H. Geubelle, J. S. Moore, M. R. Kessler, S. R. Sriram, E. N. Brown, and S. Viswanathan, *Autonomic healing of polymer composites*. Nature, 2001, 409, p. 794-797.
59. E. N. Brown, N. R. Sottos, and S. R. White, *Fracture testing of a self-healing polymer composite*. Experimental Mechanics, 2002, 42, p. 372-379.
60. S. M. Bleay, C. B. Loader, V. J. Hawyes, L. Humberstone, and P. T. Curtis, *A smart repair system for polymer matrix composites*. Composites Part A: Applied Science and Manufacturing, 2001, 32, p. 1767-1776.
61. J. W. C. Pang and I. P. Bond, *A hollow fibre reinforced polymer composite encompassing self-healing and enhanced damage visibility*. Composites Science and Technology, 2005, 65, p. 1791-1799.
62. K. A. Williams, A. J. Boydston, and C. W. Bielawski, *Towards electrically conductive, self-healing materials*. Journal of the Royal Society Interface, 2007, 4, p. 359-362.
63. S. Gupta, Q. Zhang, T. Emrick, A. C. Balazs, and T. P. Russell, *Entropy-driven segregation of nanoparticles to cracks in multilayered composite polymer structures*. Nature Materials, 2006, 5, p. 229-233.
64. J. A. Carlson, J. M. English, and D. J. Coe, *A flexible, self-healing sensor skin*. Smart Materials and Structures, 2006, 15, p. N129-N135.
65. B. Ghosh and M. W. Urban, *Self-Repairing Oxetane-Substituted Chitosan Polyurethane Networks*. Science, 2009, 323, p. 1458-1460.
66. M. Burnworth, L. Tang, J. R. Kumpfer, A. J. Duncan, F. L. Beyer, G. L. Fiore, S. J. Rowan, and C. Weder, *Optically healable supramolecular polymers*. Nature, 2011, 472, p. 334-337.
67. X. Chen, M. A. Dam, K. Ono, A. Mal, H. Shen, S. R. Nutt, K. Sheran, and F. Wudl, *A Thermally Re-Mendable Cross-Linked Polymeric Material*. Science, 2002, 295, p. 1698-1702.
68. E. L. Kirkby, V. J. Michaud, J.-A. E. Månson, N. R. Sottos, and S. R. White, *Performance of self-healing epoxy with microencapsulated healing agent and shape memory alloy wires*. Polymer, 2009, p. 5533-5538.

69. E. L. Kirkby, J. D. Rule, V. J. Michaud, N. R. Sottos, S. R. White, and J.-A. E. Månson, *Embedded shape-memory alloy wires for improved performance of self-healing polymers*. Advanced Functional Materials, 2008, 18, p. 2253-2260.
70. K. S. Toohey, N. R. Sottos, J. A. Lewis, J. S. Moore, and S. R. White, *Self-healing materials with microvascular networks*. Nature Materials, 2007, 6, p. 581-585.
71. K. S. Toohey, C. J. Hansen, J. A. Lewis, S. R. White, and N. R. Sottos, *Delivery of two-part self-healing chemistry via microvascular networks*. Advanced Functional Materials, 2009, 19, p. 1399-1405.
72. K. S. Toohey, *Microvascular networks for continuous self-healing materials*. Thesis (University of Illinois at Urbana-Champaign), 2007, p.
73. D. B. Tuckerman and R. F. W. Pease, *High-Performance Heat Sinking for VLSI*. IEEE Electronic Device Letters, 1981, 2, p. 126-129.
74. X. Wei, Y. Joshi, and M. K. Patterson, *Experimental and numerical study of a stacked microchannel heat sink for liquid cooling of microelectronic devices*. Transactions of the American Society of Mechanical Engineers, 2007, 129, p. 1432-1444.
75. C. Perret, Y. Avenas, C. Gillot, J. Boussey, and C. Schaeffer, *Integrated cooling devices in silicon technology*. European Physical Journal of Applied Physics, 2002, 18, p. 115-123.
76. G. Natarajan and R. J. Bezema, *Microjet cooler with distributed returns*. Heat Transfer Engineering, 2007, 28, p. 779-787.
77. J. M. Koo, S. Im, L. Jiang, and K. E. Goodson, *Integrated microchannel cooling for three-dimensional electronic circuit architectures*. Journal of Heat Transfer, 2005, 127, p. 49-58.
78. R. Sabbah, R. Kizilel, J. R. Selman, and S. Al-Hallaj, *Active (air-cooled) vs. passive (phase change material) thermal management of high power lithium-ion packs: Limitation of temperature rise and uniformity of temperature distribution*. Journal of Power Sources, 2008, 182, p. 630-638.
79. J. Park and X. Li, *Effect of flow and temperature distribution on the performance of a PEM fuel cell stack*. Journal of Power Sources, 2006, 162, p. 444-459.
80. S. Yu and D. Jung, *Thermal management strategy for a proton exchange membrane fuel cell system with a large active cell area*. Renewable Energy, 2008, 33, p. 2540-2548.
81. D. W. Dunn and C. C. Lin, *On the role of three-dimensional disturbances in the stability of supersonic boundary layers*. Journal of the Aeronautical Sciences, 1953, 20, p. 577-578.
82. E. Reshotko, *Drag reduction by cooling in hydrogen-fueled aircraft*. Journal of Aircraft, 1979, 16, p. 584-590.
83. P. G. Parikh and A. L. Nagel, *Application of laminar flow control to supersonic transport configurations*. NASA CR-181917, 1990, p.
84. A. K. Noor, S. L. Venneri, D. B. Paul, and M. A. Hopkins, *Structures technology for future aerospace systems*. Computers and Structures, 2000, 74, p. 507-519.
85. G. Maltezos, M. Johnston, and A. Scherer, *Thermal management in microfluidics using micro-Peltier junctions*. Applied Physics Letters, 2005, 87, p. 154105:154101-154103.

86. C. Zhang, J. Xu, W. Ma, and W. Zheng, *PCR microfluidic devices for DNA amplification*. Biotechnology Advances, 2006, 24, p. 243-284.
87. R. B. Oueslati, D. Therriault, and S. Martel, *PCB-integrated heat exchanger for cooling electronics using microchannels fabricated with the direct-write method*. IEEE Transactions on components and packaging technologies, 2008, 31, p. 869-874.
88. B. D. Kozola, L. A. Shipton, V. K. Natrajan, K. T. Christensen, and S. R. White, *Characterization of Active Cooling and Flow Distribution in Microvascular Polymers*. Journal of Intelligent Material Systems and Structures, 2010, 21, p. 1147-1156.
89. M. R. Kessler, N. R. Sottos, and S. R. White, *Self-healing structural composite materials*. Composites: Part A, 2003, 34, p. 743-753.
90. R. S. Trask and I. P. Bond, *Biomimetic self-healing of advanced composite structures using hollow glass fibres*. Smart Materials and Structures, 2006, 15, p. 704-710.
91. R. S. Trask, G. J. Williams, and I. P. Bond, *Bioinspired self-healing of advanced composite structures using hollow glass fibres*. Journal of the Royal Society Interface, 2007, 4, p. 363-371.
92. M. Zako and N. Takano, *Intelligent Material Systems Using Epoxy Particles to Repair Microcrarcks and Delamination Damage in GFRP*. Journal of Intelligent Material Systems and Structures, 1999, 10, p. 836-841.
93. J. O. Outwater and D. J. Gerry, *On the Fracture Energy, Rehealing Velocity and Refracture Energy of Cast Epoxy Resin*. Journal of Adhesion, 1969, 1, p. 290-298.
94. X. Wang, Y. Yan, and R. Zhang, *Recent Trends and Challenges in Complex Organ Manufacturing*. Tissue Engineering: Part B, 2010, 16, p. 189-197.
95. N. Zhan, Y. Li, C. Zhang, Y. Song, H. Wang, L. Sun, Q. Yang, and X. Hong, *A novel multinozzle electrospinning process for preparing superhydrophobic PS films with controllable bean-on-string/microfiber morphology*. Journal of Colloid and Interface Science, 2010, 345, p. 491-495.
96. X. Zhao, J. R. G. Evans, M. J. Edirisinghe, and J. H. Song, *Ceramic Freeforming Using an Advanced Multinozzle Ink-Jet Printer*. Journal of Materials Synthesis and Processing, 2001, 9, p. 319-327.
97. C. D. Meinhart and H. Zhang, *The Flow Structure Insides a Microfabricated Inkjet Printhead*. Journal of Microelectromechanical Systems, 2000, 9, p. 67-75.
98. J. Chen and K. D. Wise, *A High-Resolution Silicon Monolithic Nozzle Array for Inkjet Printing*. IEEE Transactions on Electronic Devices, 1997, 44, p. 1401-1409.
99. J. S. Aden, J. H. Bhórquez, D. M. Collins, M. D. Crook, A. García, and U. E. Hess, *The Third-Generation HP Thermal InkJet Printhead*. Hewlett-Packard Journal, 1994, 45, p. 41-45.
100. B. Derby, *Inkjet Printing of Functional and Structural Materials: Fluid Property Requirements, Feature Stability, and Resolution*. Annual Review of Materials Research, 2010, 40, p. 395-414.
101. J.-S. Lee, S.-Y. Kim, Y.-J. Kim, J. Park, Y. Kim, J. Hwang, and Y.-J. Kim, *Design and evaluation of a silicon based multi-nozzle for addressable jetting*

using a controlled flow rate in electrohydrodynamic jet printing. Applied Physics Letters, 2008, 93, p. 243114:243111-243113.
102. S. Hong, J. Zhu, and C. A. Mirkin, *Multiple Ink Nanolithography: Toward a Multiple-Pen Nano-Plotter*. Science, 1999, 286, p. 523-525.
103. K. Salaita, Y. Wang, and C. A. Mirkin, *Applications of dip-pen nanolithography*. Nature Nanotechnology, 2007, 2, p. 145-155.
104. K. Salaita, S. W. Lee, X. Wang, L. Huang, T. M. Dellinger, C. Liu, and C. A. Mirkin, *Sub-100 nm, Centimeter-Scale, Parallel Dip-Pen Nanolithography*. Small, 2005, 1, p. 940-945.
105. D. S. Ginger, H. Zhang, and C. A. Mirkin, *The Evolution of Dip-Pen Nanolithography*. Angewandte Chemie International Edition, 2004, 43, p. 30-45.
106. X. Wang, D. A. Bullen, J. Zou, C. Liu, and C. A. Mirkin, *Thermally actuated probe array for parallel dip-pen nanolithography*. Journal of Vacuum Science and Technology B, 2004, 22, p. 2563-2567.
107. D. Bullen, S.-W. Chung, X. Wang, J. Zou, C. A. Mirkin, and C. Liu, *Parallel dip-pen nanolithography with arrays of individually addressable cantilevers*. Applied Physics Letters, 2004, 84, p. 789-791.
108. D. Bullen and C. Liu, *Electrostatically actuated dip pen nanolithography probe arrays*. Sensors and Actuators A, 2006, 125, p. 504-511.
109. W. Shim, A. B. Branschweig, X. Liao, J. Chai, J. K. Lim, G. Zheng, and C. A. Mirkin, *Hard-tip, soft-spring lithography*. Nature, 2011, 469, p. 516-520.
110. F. Huo, Z. Zheng, G. Zheng, L. R. Giam, H. Zhang, and C. A. Mirkin, *Polymer Pen Lithography*. Science, 2008, 321, p. 1658-1660.
111. M. Mott, J.-H. Song, and J. R. G. Evans, *Microengineering of Ceramics by Direct Ink-Jet Printing*. Journal of the American Ceramics Society, 1999, 82, p. 1653-1658.
112. J. M. Meacham, A. O'Rourke, Y. Yang, A. G. Fedorov, F. L. Degertekin, and D. W. Rosen, *Micromachined Ultrasonic Print-Head for Deposition of High-Viscosity Materials*. Journal of Manufacturing Science and Engineering, 2010, 132, p. 030905:030901-030911.
113. S. A. Theron, A. L. Yarin, E. Zussman, and E. Kroll, *Multiple jets in electrospinning: experiment and modeling*. Polymer, 2005, 46, p. 2889-2899.
114. L. M. Bellan, C. Alpha, T. Corso, J. Henion, and H. G. Craighead, *Chip-based microfabricated electrospinning nozzles*. Journal of Vacuum Science and Technology B, 2008, 26, p. 2539-2542.
115. K.-B. Lee, E.-Y. Kim, C. A. Mirkin, and S. M. Wolinsky, *The use of Nanoarrays for Highly Sensitive and Selective Detection of Human Immunodeficiency Virus Type 1 in Plasma*. Nano Letters, 2004, 4, p. 1869-1872.
116. J. Hyun, J. Kim, S. L. Craig, and A. Chilkoti, *Enzymatic Nanolithography of a Self-Assembled Oligonucleotide Monolayer on Gold*. Journal of the American Chemical Society, 2004, 126, p. 4770-4771.
117. D. C. Coffey and D. S. Ginger, *Patterning Phase Separation in Polymer Films with Dip-Pen Nanolithography*. Journal of the American Chemical Society, 2005, 127, p. 4564-4565.
118. S. G. Rao, L. Huang, W. Setyawan, and S. Hong, *Nanotube electronics: Large-scale assembly of carbon nanotubes*. Nature, 2003, 425, p. 36-37.

119. S. Lenhert, P. Sun, Y. Wang, H. Fuchs, and C. A. Mirkin, *Massively Parallel Dip-Pen Nanolithography of Heterogeneous Supported Phospholipid Multilayer Patterns*. Small, 2007, 3, p. 71-75.
120. K. A. McCulloh, J. S. Sperry, and F. R. Adler, *Water transport in plants obeys Murray's law*. Nature, 2003, 421, p. 939-942.
121. A. Roth-Nebelsick, D. Uhl, V. Mosbrugger, and H. Kerp, *Evolution and Function of Leafe Venation Architecture: A Review*. Annals of Botany, 2001, 87, p. 553-566.
122. A. R. Pries and T. W. Secomb, *Blood Flow in Microvascular Networks*, in *Handbook of Physiology,* 2008, Wiley.
123. J. Serbin, A. Ovsianikov, and B. Chichkov, *Fabrication of woodpile structures by two-photon polymerization and investigation of their optical properties*. Optics Express, 2004, 12, p. 5221-5228.
124. K. Salaita, Y. Wang, J. Fragala, R. A. Vega, C. Liu, and C. A. Mirkin, *Massively Parallel Dip-Pen Nanolithography with 55000-Pen Two-Dimensional Arrays*. Angewandte Chemie International Edition, 2006, 118, p. 7378-7381.

2.8 Figures

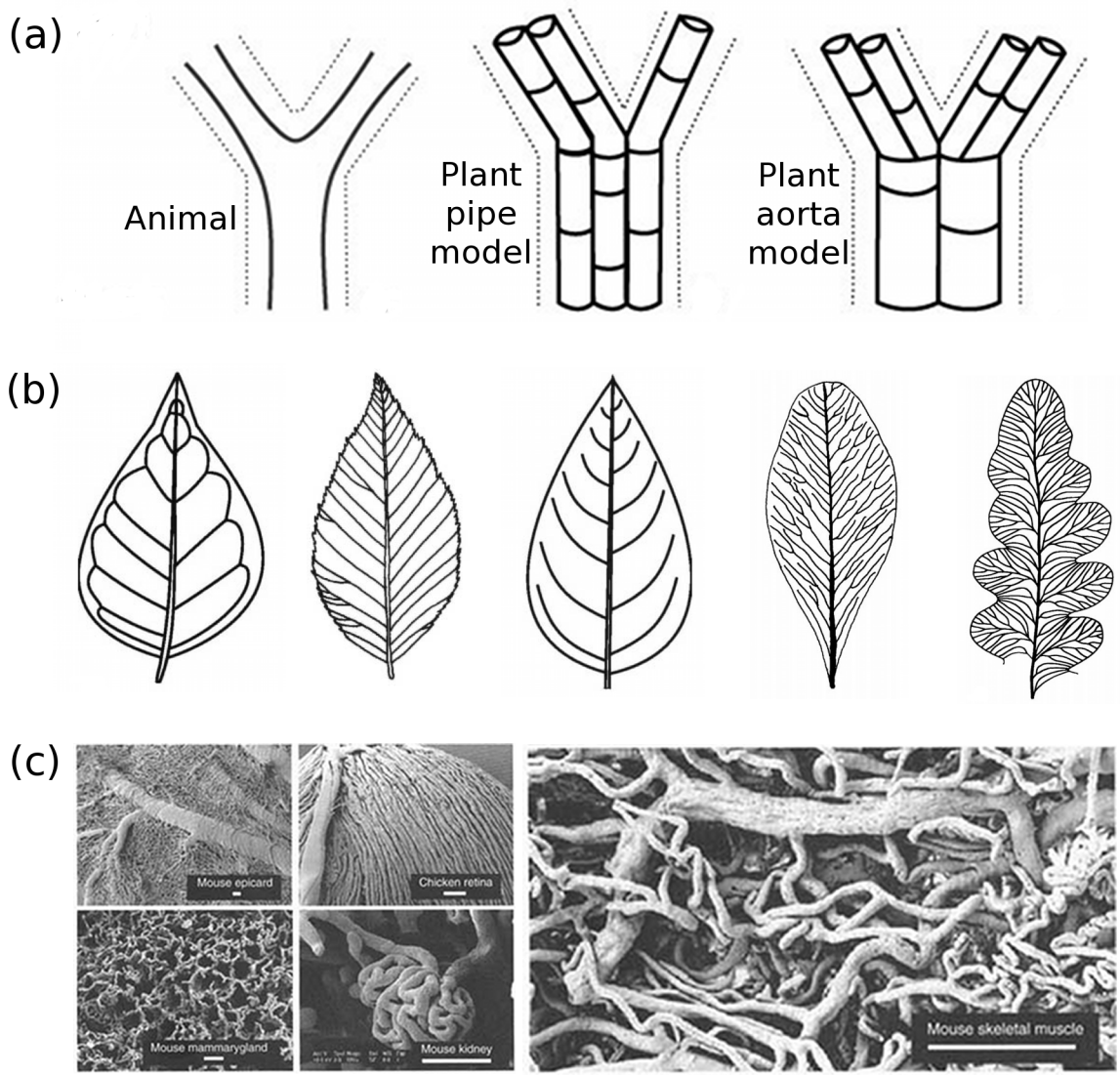

Figure 2.1. Biological microvasculature. (a) Bifurcating branch geometries for animals and plants.[120] Reproduced with permission from Nature Publishing Group. (b) 2D leaf venation patterns.[121] Reproduced with permission from Oxford University Press. (c) Microvascular structure in various tissues imaged by scanning electron microscopy. Scale bars all 40 μm.[122]

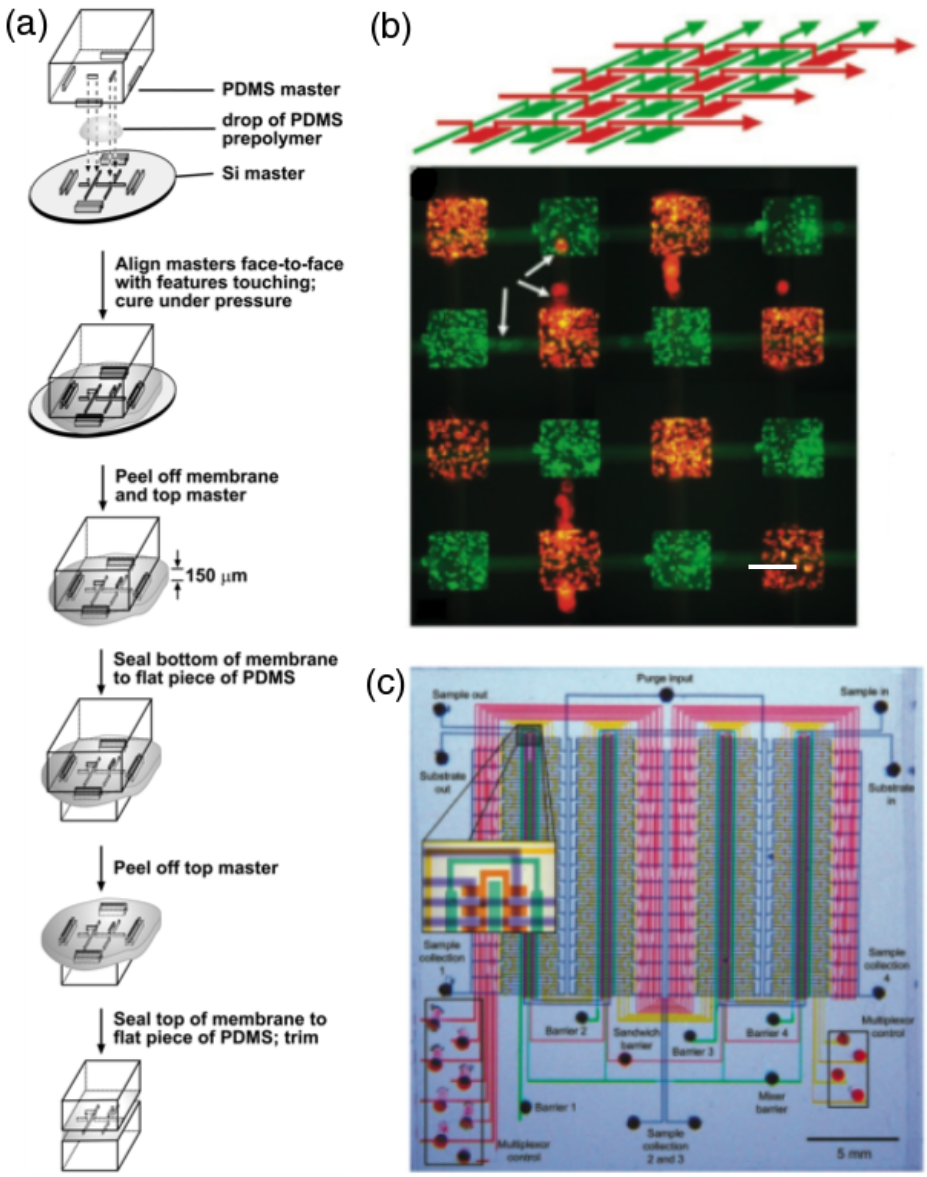

Figure 2.2. Creation of multi-network microchannels via 3D soft-lithography. (a) Schematic diagram of 3D soft-lithography technique.[6] Reproduced with permission from Cambridge University Press. (b) Fluorescence image of human bladder cancer cells (green) and bovine adrenal capillary endothelial cells patterned in wells on a substrate (scalebar is 200 μm).[9] Reproduced with permission from the National Academy of Sciences. (c) Control channel configurations allow control of biological specimens in massively paralleled on-chip mixing.[12, 13] Reproduced with permission from the American Association for the Advancement of Science.

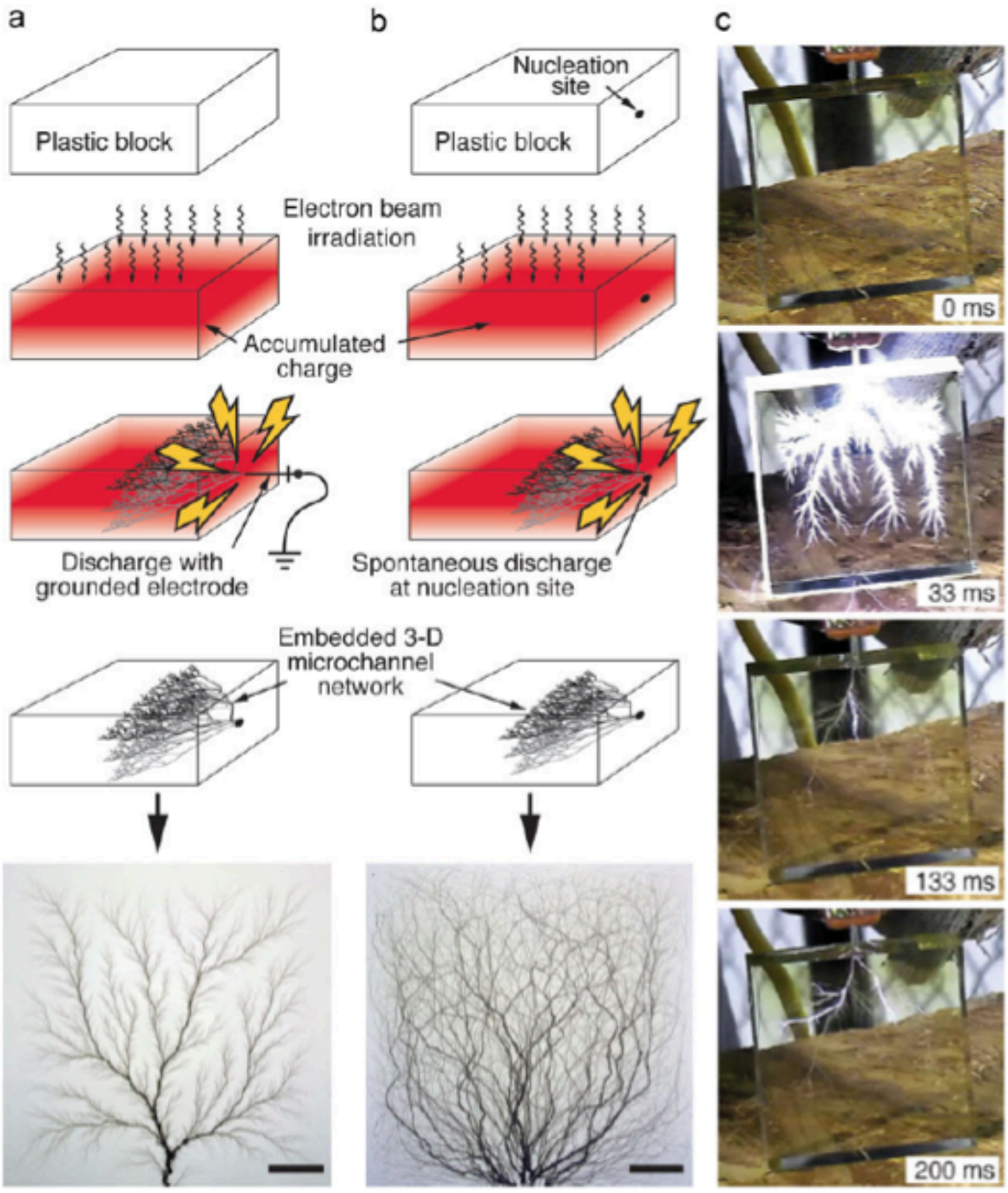

Figure 2.3. Fabrication of 3D microvascular networks with electrostatic discharge via either (a) ground or (b) nucleation site discharge. (c) Electric discharge forming microvasculature photographed as a time series.[25] Reproduced with permission from John Wiley & Sons, Inc.

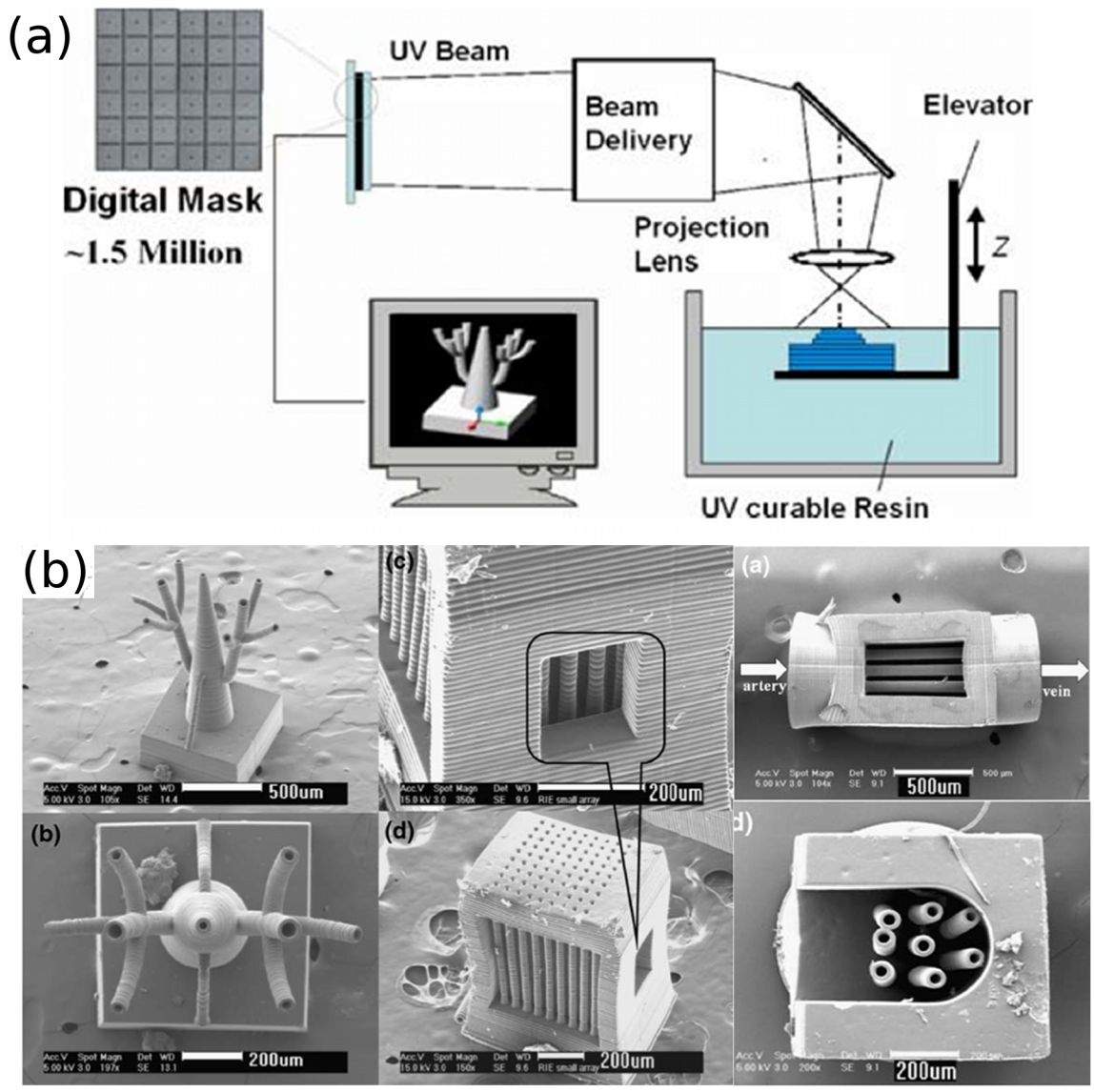

Figure 2.4. (a) Schematic of a representative projection micro-stereolithography experimental set-up. (b) Views of a micro-bioreactor fabricated by projection micro-stereolithography.[38] Reproduced with permission from Springer Science+Business Media.

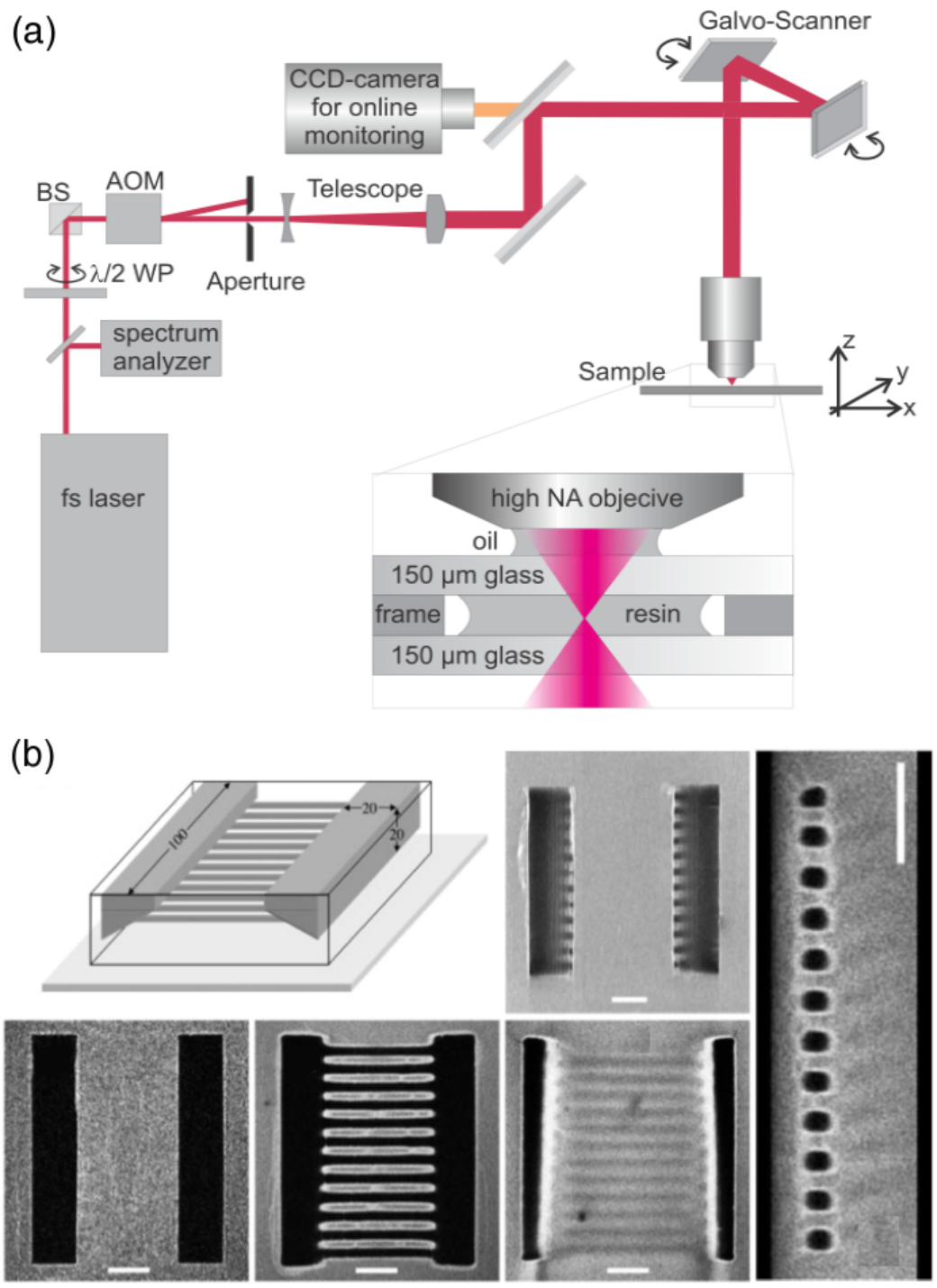

Figure 2.5. Microchannel creation via two-photon polymerization (TPP). (a) Schematic of a two-photon polymerization system.[123] (b) Microchannels for potential bioanalytical applications created by TPP, where the 12 channels are 50 μm in length and 4 μm x 4 μm in cross-section (scalebars are 20 μm).[48] Figure reproduced and modified from Figure 3 on p.1108 [48] with permission from American Association for the Advancement of Science.

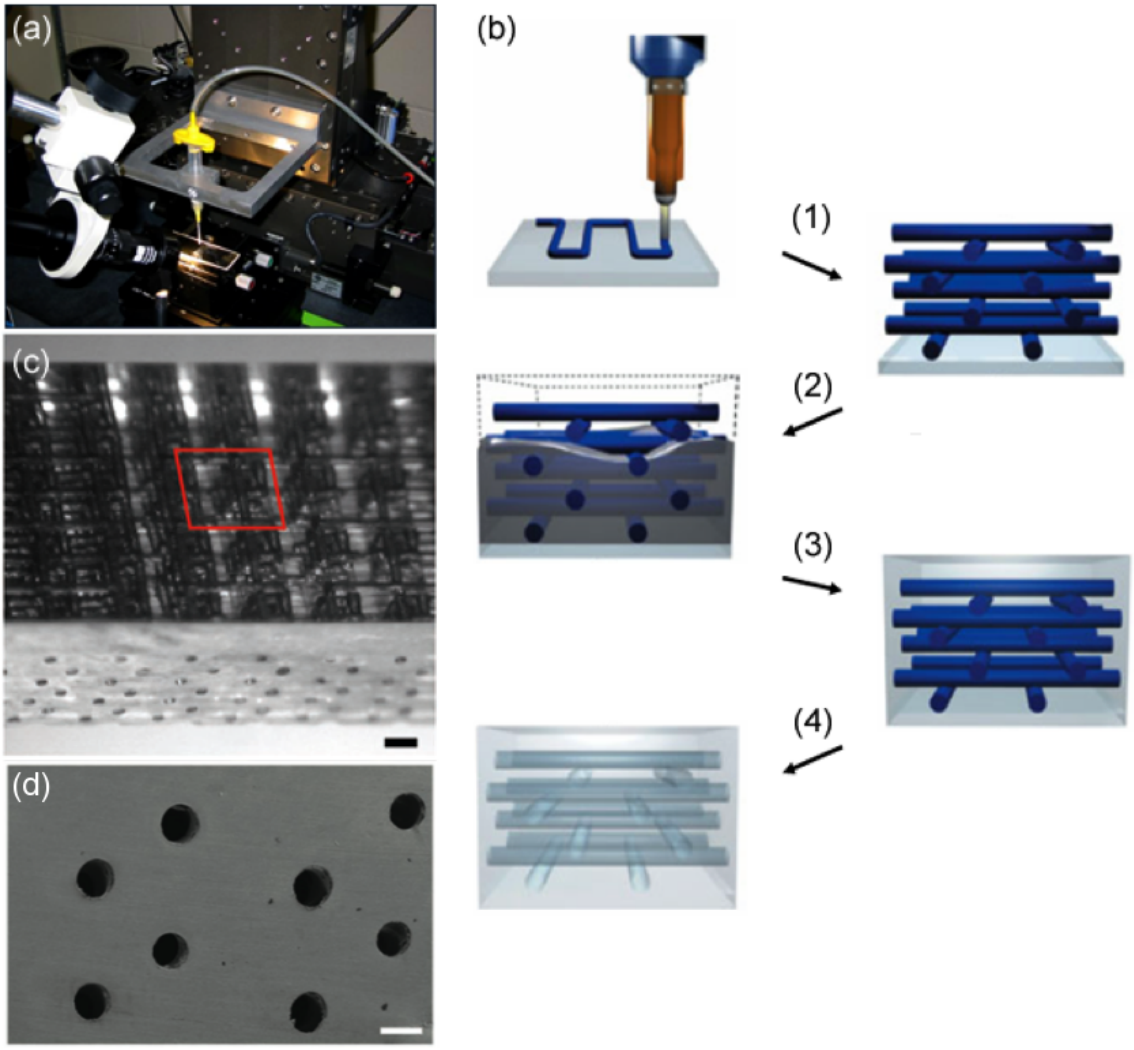

Figure 2.6. Microchannel fabrication via direct ink writing. (a) A direct ink writing system consisting of a pressure activated deposition nozzle mounted to a 3-axis positioning stage. (b) A schematic for fugitive direct ink writing. A fugitive ink is deposited on a substrate in a layer-by-layer fashion (1). The interstitial spaces are infiltrated with a liquid resin (2) that is subsequently polymerized (3). The fugitive ink is removed by heating to 70°C and applying a light vacuum (4). (c) Top view of an interconnected 3D microchannel network (scale bar is 500 μm). (d) Cross-section view of circular microchannels (scale bar is 250 μm).[53, 54] Reproduced with permission from John Wiley & Sons, Inc. and Nature Publishing Group.

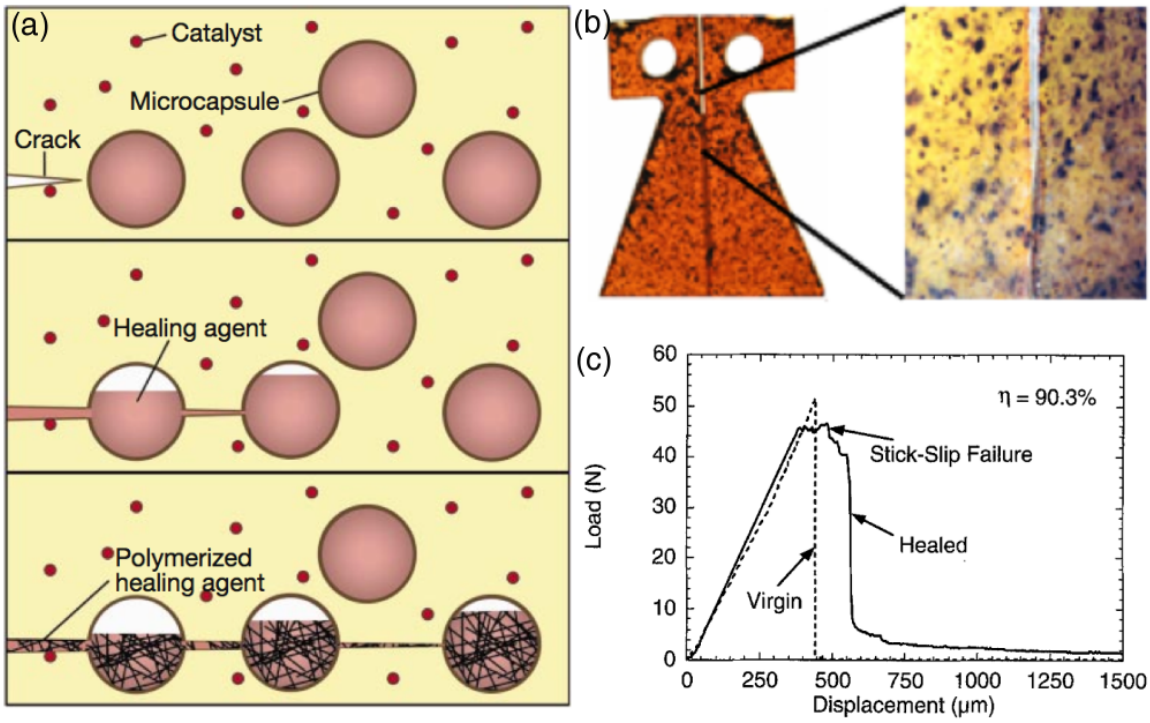

Figure 2.7. (a) Schematic of the microcapsule self-healing concept. Microencapsulated healing agent (DCPD monomer) and wax-protected catalyst microspheres (Grubb's catalyst) are embedded in an epoxy matrix. A propagating crack intersects the healing agent microcapsules, which releases into the crack plane and polymerizes on contact with the catalyst.[58] Reproduced with permission from Nature Publishing Group. (b) Tapered double-cantilever beam (TDCB) specimens with embedded healing agent at the crack interface. (c) Load-displacement curve for TDCB specimen, indicating up to 90.3% fracture toughness recovery.[59] Reproduced with permission from Springer Science+Business Media.

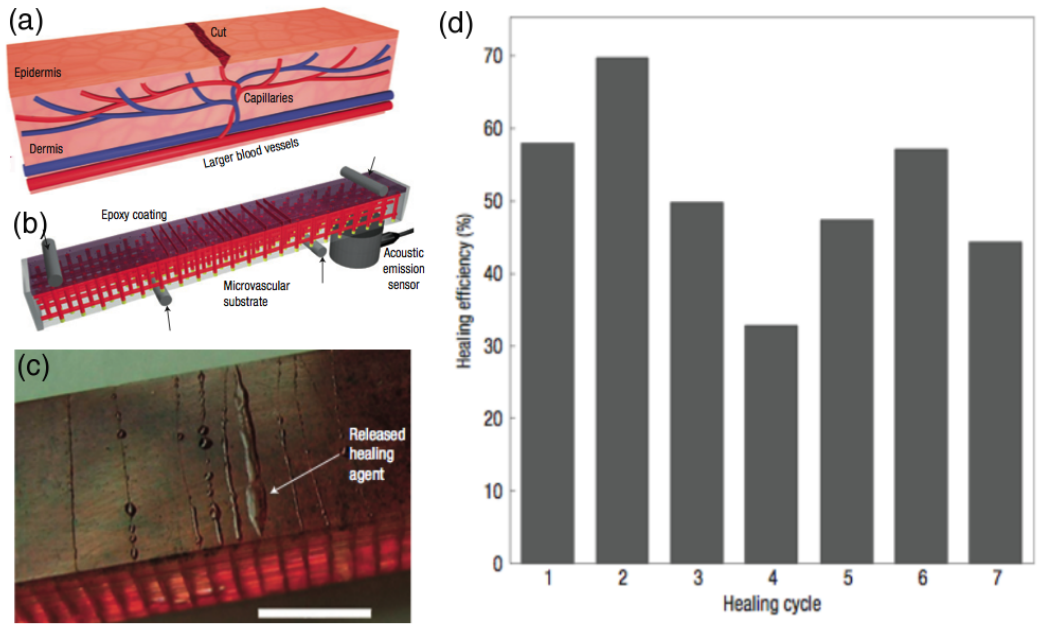

Figure 2.8. (a) Schematic of microvasculature supplying nutrients to heal a cut in the epidermal layer. (b) Schematic of 4-point bend test for microchannel-based self-healing concept. (c) Optical image of crack healing at the brittle coating surface (scale bar is 5 mm). (d) Healing efficiency for multiple healing cycles for 10 w/w% wax microspheres in brittle coating layer.[70] Reproduced with permission from Nature Publishing Group.

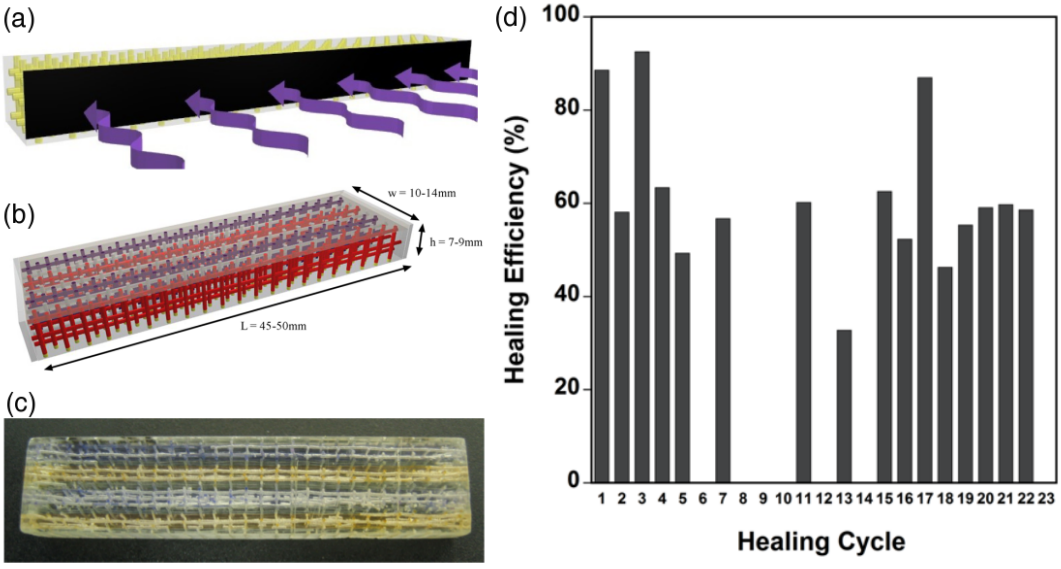

Figure 2.9. (a) Schematic of a single network filled with photopolymer that is segmented via covering with an opaque mask and curing the exposed regions. (a) Schematic of filled specimen with two-part epoxy system. (c) Image of bend bar filled with DCPD and Grubb's catalyst.[72] Images reproduced from the doctoral dissertation by K. S. Toohey with permission. (d) Healing efficiency of two-part epoxy over multiple healing cycles.[71] Reproduced with permission from John Wiley & Sons, Inc.

(a)

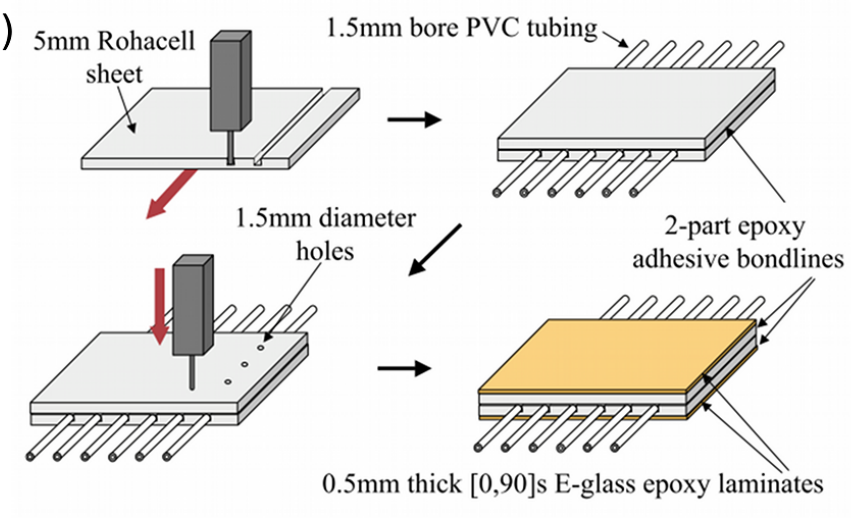

(b)

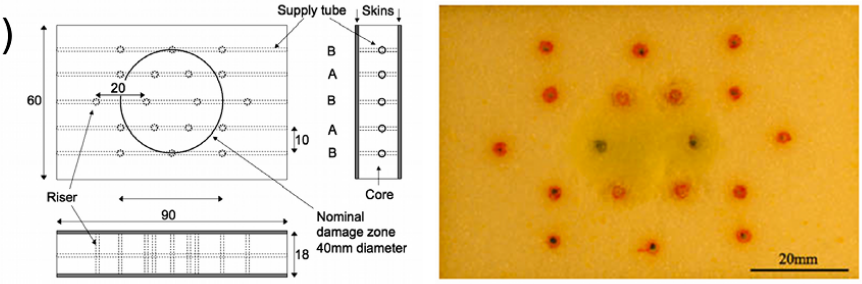

(c)

Damage Zone Photograph	Area Ratio Red:Blue (target 2:1)	Total area relative to residual dent	A (Red) risers breached (target: 4)	B (Blue) risers breached (target: 2)
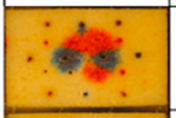	1.4:1	0.74	4	3
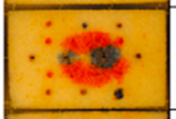	2.9:1	0.77	6	2
	1.7:1	0.62	5	2
	2.5:1	0.48	4	3
	3.1:1	0.72	6	2

Figure 2.10. (a) Machining and tubing affixed with adhesive create microvascular networks within the foam core of a composite sandwich structure.[22] (b) Design of epoxy resin hardener delivery to composite surface and fabricated specimen after mechanical testing. (c) Area fraction spreading after impact of epoxy resin and hardener at composite surface.[23] Reproduced with permission from Elsevier.

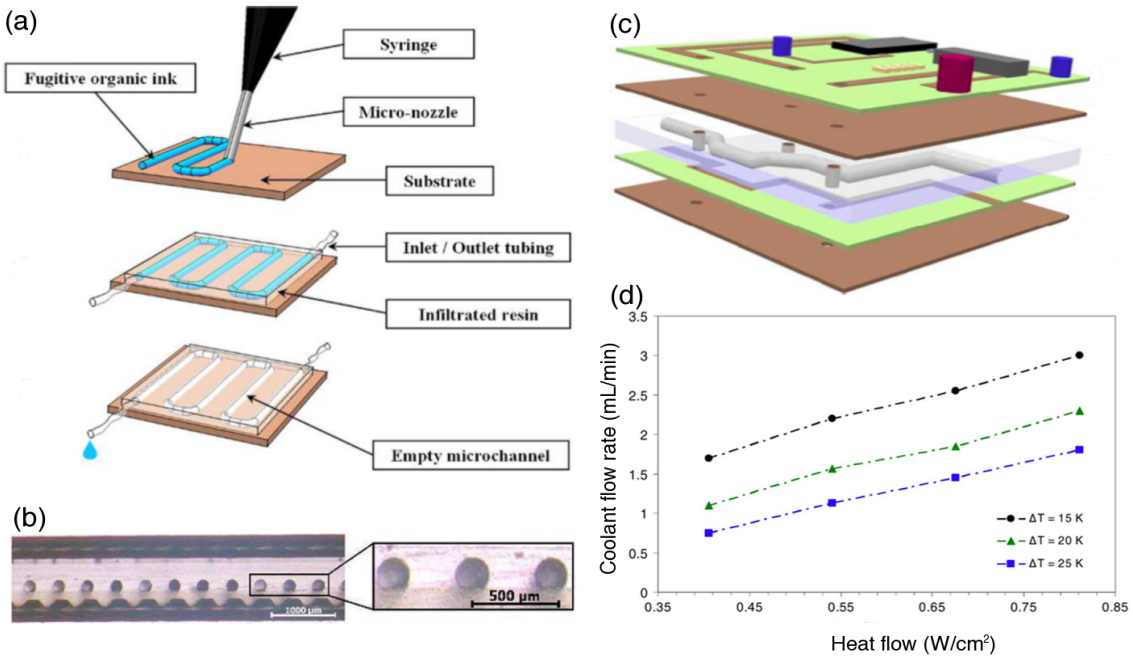

Figure 2.11. (a) Schematic representation of fabrication of 2D microchannel for temperature control. (b) Cross-section of 200 µm diameter channel embedded between copper sheets. (c) Exploded schematic of four-layer printed-circuit board (PCB) surrounding embedded microchannel. (d) Experimental water flow rates to dissipate heat created by PCB.[87]

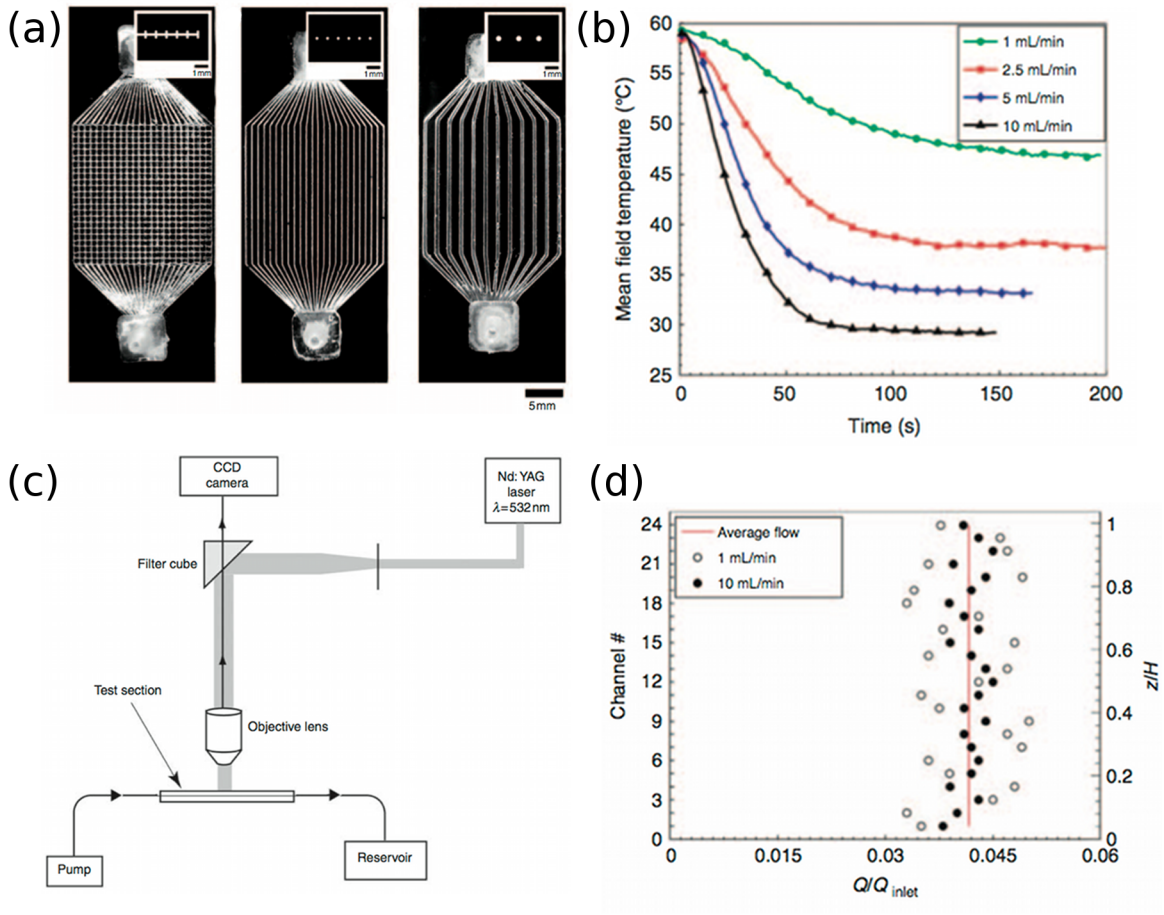

Figure 2.12. (a) Microchannels networks for cooling with geometries (from left to right) of 3 layers with 24 microchannels, 1 layer with 24 microchannels, and 1 layer with 12 microchannels. (b) Transient response of mean temperature for 1 layer 24 microchannel array. (c) Micro-PIV experimental set-up for imaging fluid flow velocities. (d) Flow map of the 24 microchannel array network at low and high input flow rates.[88] Reproduced with permission from SAGE Publications.

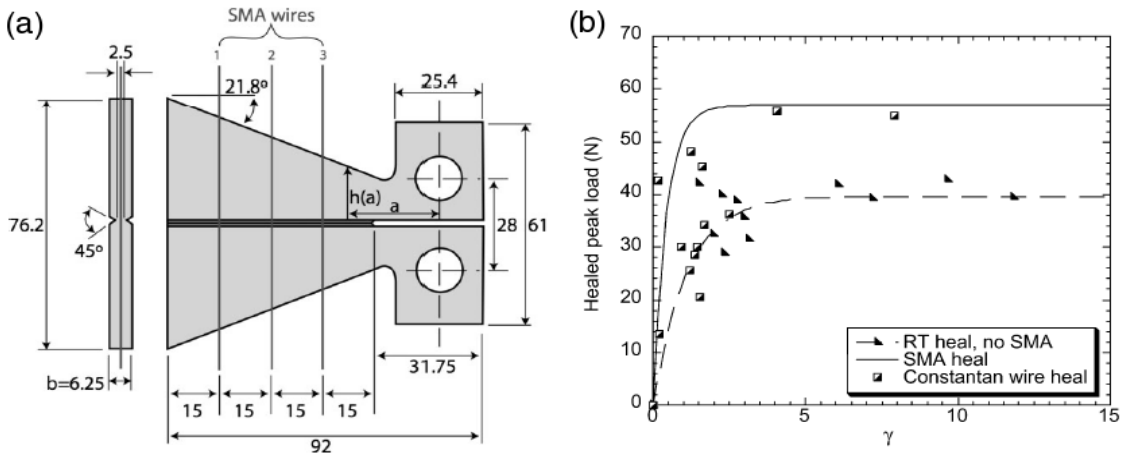

Figure 2.13. (a) TDCB geometry used to test use of shape-memory alloy (SMA) wires to enhance healing (units in mm). (b) Healed peak loads versus fill factor for different sample configurations. Triangles are room temperature heals with elastic bands to bring crack faces close. Squares are with constantan non-SMA wires to heat the specimen without affecting the crack opening. Wire heating recovers much of the healed value seen in SMA tests.[69] Reproduced with permission by John Wiley & Sons, Inc.

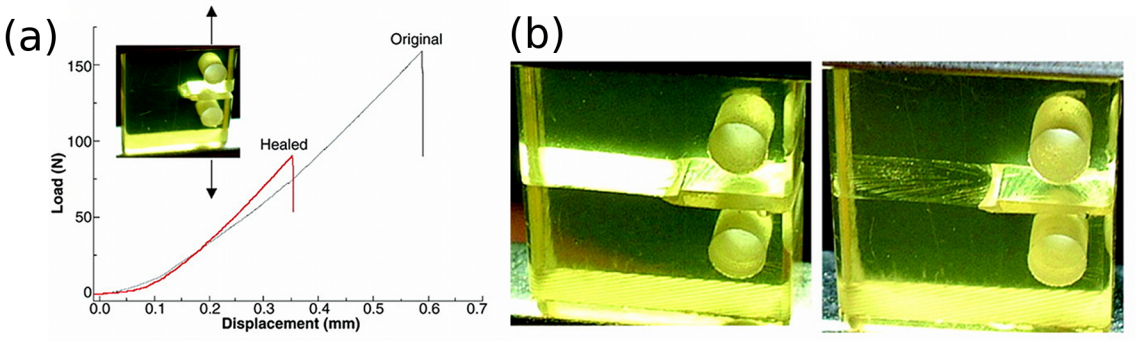

Figure 2.14. (a) Load-displacement curve for a thermally remendable specimen before and after healing. (b) Image of a broken specimen before (left) and after (right) thermal treatment at 120°C.[67] Reproduced with permission by the American Association for the Advancement of Science.

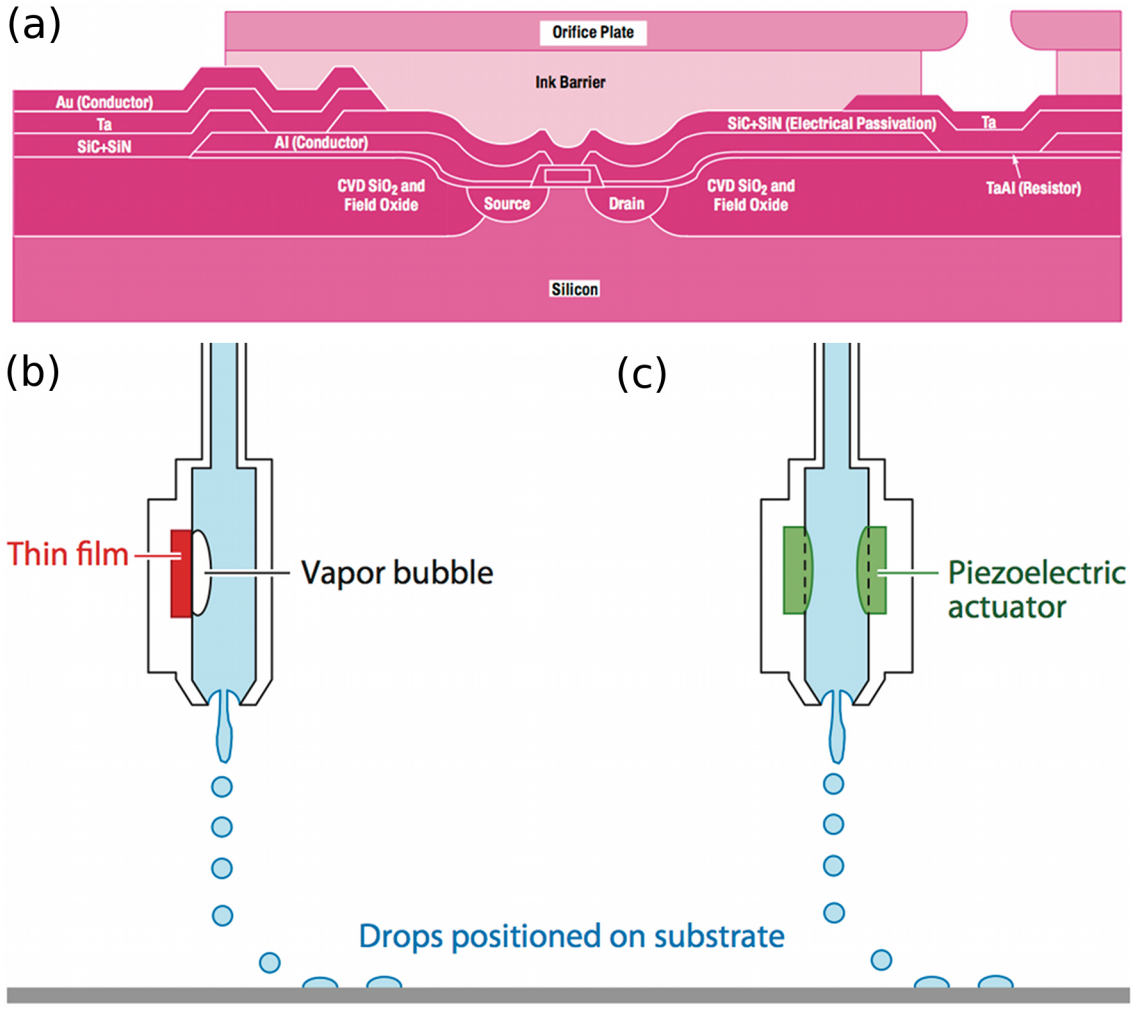

Figure 2.15. (a) Integrated circuit layers for Hewlett-Packard 104 nozzle DeskJet 1200C printhead. The design is a thermal inkjet printhead design. [99] Drop on demand printing is controlled by either (b) thin film resistive heating to create microbubbles or (c) piezoelectric actuators to mechanically induce droplet ejection.[100]

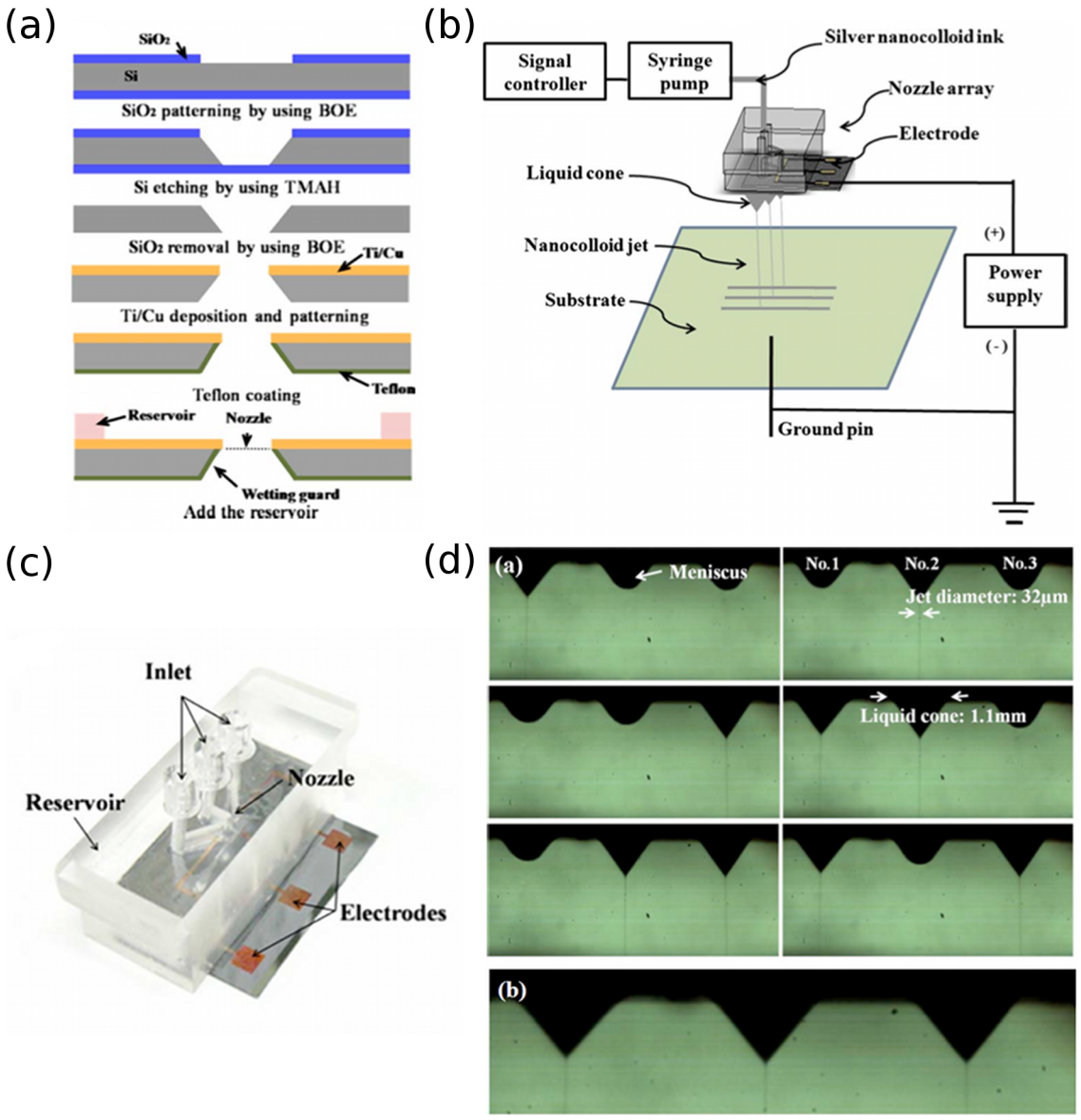

Figure 2.16. (a) Schematic for multinozzle electrospinning fabrication process. (b) Experimental apparatus for multinozzle electrospun filamentary deposition. (c) Fabricated device with three multinozzle openings. (d) Demonstration of addressable multinozzle printing.[101] Reproduced with permission from the American Institute of Physics.

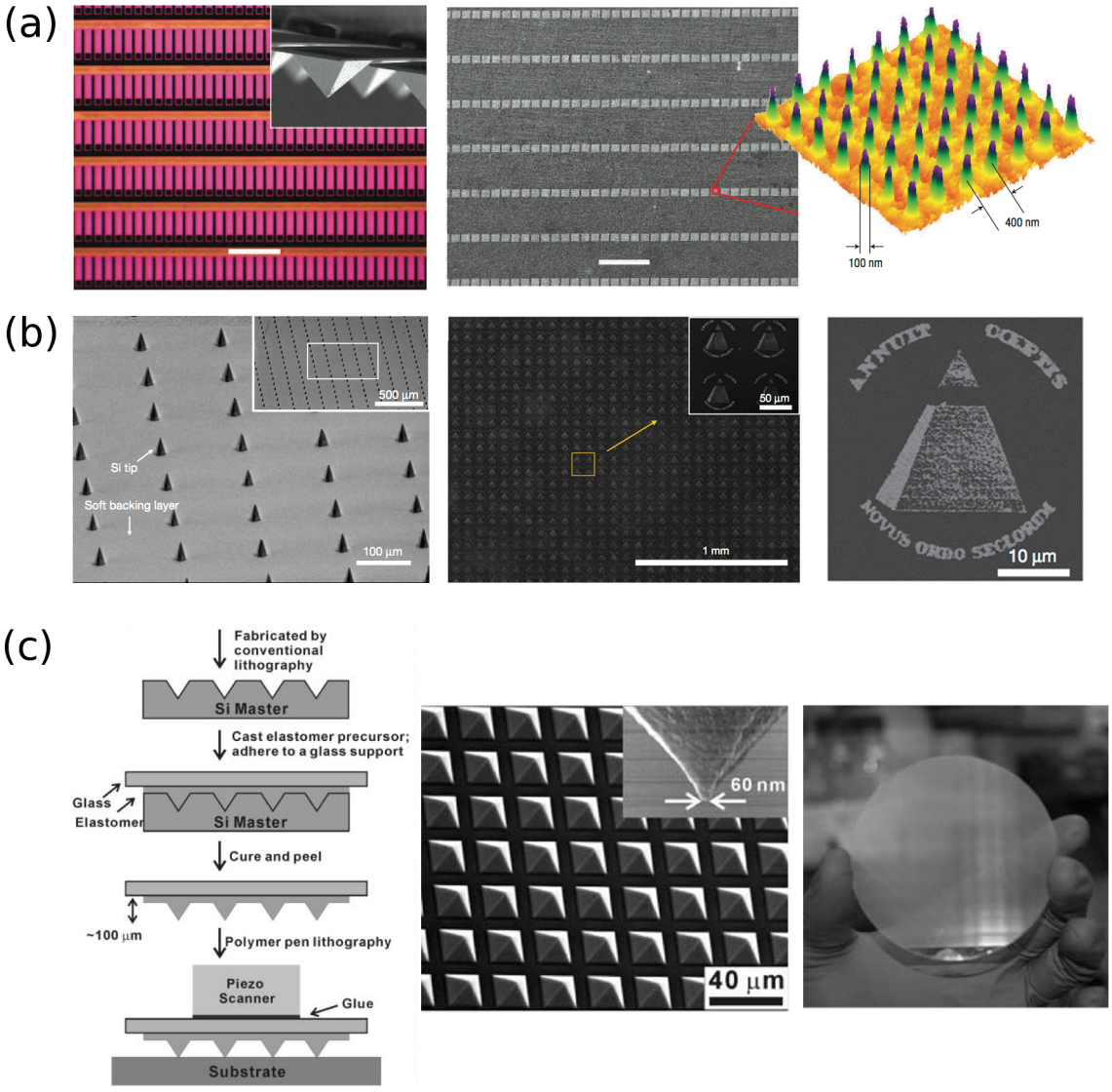

Figure 2.17. (a) Subset of a 55,000 cantilever dip pen nanolithography array (left) that fabricates 40 x 40 gold nanodot arrays (right).[124] Reproduced with permission from John Wiley & Sons, Inc. (b) Hard-tip, soft-spring lithography arrays consist of silicon tips on a PDMS substrate (left), which is used for massively parallel deposition (middle. ~19,000 individual patterns) of an intricate pattern (right).[109] Reproduced with permission from Nature Publishing Group. (c) Polymer pen lithography arrays are fabricated in PDMS (left) with fine tip dimensions (middle) and up to 11 million tips on a single wafer (right).[110] Reproduced with permission from the American Association for the Advancement of Science.

CHAPTER 3

SELF-HEALING MATERIALS WITH BINARY INTERPENETRATING NETWORKS[1]

3.1 Introduction

Complex microvascular networks, such as leaf venation[1-4] and blood vascularization,[5-7] are widely observed in biological systems. These networks enable targeted delivery of nutrients for growth and healing. Due to their complicated architecture, replication of these microvascular systems remains a significant challenge for those pursuing synthetic analogs. Various techniques including soft lithography,[8-10] laser ablation,[11, 12] and direct-write assembly[13] have been employed to create microvascular networks that consist of uniform, interconnected microchannels. However, to date, these fabrication techniques have mainly been used to construct simple networks composed of a single vascular pathway.

Of particular interest is the ability of microvascular networks to enable repetitive healing of damage in biological and synthetic systems. For example, human skin can undergo repeated repair of damage in a single location. The outer layer of skin (the epidermis) serves as a protective coating, preventing outside pathogens from infiltrating the body.[14] The dermis, which lies beneath this layer, contains a complicated microvascular network composed of larger blood vessels that branch into smaller capillaries, which deliver nutrients to and remove waste products from the dermal and epidermal regions. Several strategies for reliable network design enable healing over multiple damage cycles, including thrombosis, capillary rerouting of fluid, and

[1] Portions of the work and figures presented in this chapter have been reproduced from published work [15], with permission from John Wiley & Sons, Inc.

vasoconstriction in animals and multiple parallel xylem in plants.[16] Replication of biological self-healing in structural materials that suffer repeated mechanical damage could dramatically increase service lifetimes.[17-20]

Toohey *et al*.[14] reported a novel epoxy coating/substrate self-healing architecture with single microvasculature embedded via direct-write assembly.[13, 21] Using the original dicyclopentadiene/Grubbs' catalyst healing system, damage is repaired up to seven cycles. Toohey *et al*. subsequently modified this design by photolithographically patterning four isolated regions within the embedded microvascular network, which contain alternating epoxy resin and hardener components.[22] This architecture achieved up to 16 intermittent healing events out of 23 cycles. A key disadvantage of this approach is that healing agents must migrate and diffusively mix within the crack plane over long distances that correspond roughly to the half thickness of a given isolated microvascular region. Importantly, even these simple networks, which do not obey Murray's law, can greatly enhance the performance of self-healing materials.

In this chapter, we report a new biomimetic coating/substrate architecture design in which a binary interpenetrating microvascular network is embedded. This design allows the use of a two-part healing chemistry based on an epoxy resin and hardener, each of which are sequestered in the embedded microvascular networks until the come into contact in the crack plane upon fracture. To fabricate these interpenetrating microvascular networks, several advancements in direct ink writing are implemented including vertical printing and dual ink printing. Using this novel design, we demonstrate a significant enhancement in the ability to repeatedly heal mechanical damage at a given site.

3.2 Experimental Methods

3.2.1 Fugitive Ink Preparation

A microcrystalline wax ink is prepared by the addition of 60 w/w% microcrystalline wax (SP-19, Strahl & Pitsch, Inc.) and 40 w/w% heavy mineral oil (Fischer Scientific). The components are melted at ~100°C and stirred for 10 min. The melted solution is poured into 3 mL syringes (EFD Inc.) and placed in a 70°C oven until the ink solidifies, after which the syringe is air cooled to room temperature. A triblock-copolymer ink is prepared as 30 w/w% polymer (Pluronic F128, BASF) in deionized water. The copolymer is slowly added into aqueous solution over a 3 hr period while the solution is vigorously stirred and held at 5°C. After the copolymer is fully dissolved, the solution is covered with paraffin film (Parafilm, Pechiney Plastics) and refrigerated for a minimum of 12 hr to remove all air bubbles. The cooled solution is poured into refrigerated 3 mL syringes held at a 45° angle to ensure no air bubbles form on the syringe walls. The ink is then warmed to ambient temperature.

3.2.2 Fugitive Ink Rheology

The storage shear modulus, G', is measured using a controlled-stress rheometer (CVOR-200, Bohlin) fitted with a cone and plate geometry. An appropriate amount (<1 mL) of ink is placed in the testing geometry, which is maintained at the desired temperature using a controlled-temperature circulating bath (Model 9110, Polyscience). The wax ink is placed on the geometry as a solid and initially held at 25°C, with subsequent tests are performed at temperatures that increase in increments of 5°C. The pluronic ink is pipetted onto the geometry as a liquid and initially held at 5°C, with the temperature increased between tests. Oscillatory-shear experiments are measured at 1 Hz

in which the stress amplitude is incrementally increased from 0.5 to 2000 Pa for the wax ink and from 0.1 to 1000 Pa for the pluronic ink.

3.2.3 Vertical Ink Printing

To create vertical features, the nozzle is positioned over a desired location and pressure is applied to initiate ink deposition. The nozzle position is maintained until deposition commences (usually ≈0.2 s), after which the nozzle is raised at a rate equal to the deposition rate. This rate requires approximately 1 s to reach equilibrium, so the translation speed is increased in 3 steps, with 0.5 s at 50% and 0.5 s at 80% of the equilibrium translation rate. After the desired feature height is achieved, ink deposition is stopped by reducing the applied air pressure to zero; concomitantly, the nozzle is raised vertically until the deposited ink feature is disconnected from the nozzle. An array of vertical features deposited through nozzle diameters ranging from 100 to 510 μm are produced and imaged using a digital camera (PowerShot S2 IS, Canon) less than 5 min after deposition. The filament diameter, aspect ratio, and stability are measured with the image processing software ImageJ (NIH). To determine if a filament is stable, a tangent to the filament base and perpendicular to the substrate is superimposed on the image. If this tangent is crossed by the entire feature diameter at the top of the feature height, the column is considered to be bent (buckled); otherwise it is considered straight (stable).

3.2.4 Direct Ink Writing of Binary Interpenetrating Microvascular Networks

Binary interpenetrating microvascular networks are fabricated using a three-axis robotic deposition stage (ABL9000, Aerotech Inc.) whose motion is controlled by customized software (RoboCAD version 3.1). Wax and pluronic ink are housed in syringes that are fitted with 330 and 100 μm nozzles (EFD Inc.), respectively. The

syringes are mounted side-by-side in air-pressure multiplier dispensing systems (HP7X, EFD Inc.). Each ink is extruded at a rate of 4 mm s^{-1} onto pre-cured, polished epoxy substrates (Envirotex Lite, Environmental Technologies Inc.) The wax ink is patterned first, followed by the pluronic ink, which serves as a supporting layer for further ink deposition. This process is repeated as needed to construct the desired interpenetrating microvascular network. Upon completion, the patterned structures are infiltrated with the same epoxy matrix material as the substrate. The epoxy is mixed and sits for 30-40 min prior to infiltration to (1) remove a majority of the bubbles and (2) minimize the epoxy reaction with the pluronic ink. Epoxy is deposited from the structure edge and wicks to fill the interstitial spaces. Only after the base of each vertical filament is surrounded is the epoxy level increased to cover the entire structure; otherwise, capillary forces will cause neighboring filaments to clump together. After infiltration, the epoxy is cured for 24 hr at 20°C. Specimens are cut with a diamond saw (IsoMet 1000, Buehler Inc.) to provide access to the embedded pluronic ink, and the pluronic is removed via dissolution in water for 24 to 36 hr at room temperature. Upon completely removing the pluronic ink, the specimens are dried and reinfiltrated using a 10 mL syringe filled with epoxy matrix material and fitted with a 510 μm nozzle. After fully curing (≈24 hr), the specimens are cut and polished to final dimensions for 50 x 12 x 6 mm. The samples are then heated to 80°C to melt the wax ink, which is removed upon the application of a light vacuum. Any residual wax ink is removed via ultrasonication for 5 min with a heated 20 w/w% aqueous degreaser solution (VCPI-411, Cortec). The final substrate sample contains two interpenetrating microvascular networks.

3.2.5 Coating Application

A low melting temperature fugitive wax (Purester 24, Strahl & Pitsch) is infiltrated in the vertical conduits to prevent the uncured coating mixture from infiltrating the microvascular network. The coating, a mixture of 12 p.p.h. diethylenetriamine (Air Products Inc.) in EPON 828 resin (Miller Stephenson Inc.), is degassed under vacuum for 30 min. The substrate surface is thoroughly cleaned with ethanol to remove surface contaminants and then wrapped in a plastic-backed adhesive tape (Scotch Magic removable tape, 3M) to form a surface reservoir ~1 mm in thickness. The coating is applied and subsequently cured for 6 hr at 25°C, followed by 9 hr at 30°C. The coating is polished to a final thickness of approximately 700 μm. The fugitive wax is removed by briefly heating to 35°C and applying a light vacuum.

3.2.6 Fracture Testing and Healing Efficiency

The specimen is filled with epoxy resin (EPON 8132, Miller-Stephenson) in one network and with epoxy hardener (Epikure 3046, Miller-Stephenson) in the other network. The specimen coating is notched by a scribe under constant load (6-10 N) using a test panel scratcher (Corrocutter 639, Erichsen). The notch depth is approximately 5-10 μm as measured by an optical profilometer (CHR-150, STIL). The notch is specifically located above a row of network vertical features. The specimen is loaded in four-point bending, as reported in Toohey et al. [14, 22]. The load-time data are collected using LabVIEW software (v6.5, National Instruments). An acoustic-emission sensor (model SE2MEG-P, Dunegan Engineering Company) is used to detect the occurrence of crack events during the healed-specimen tests. Data from the acoustic-emission sensor are collected with a digital oscilloscope (model LC584A, LeCroy) and exported to a

computer for correlation with the load-time data in order to determine the load at which the crack reopened. The heal efficiency η is defined as the ratio of the healed facture toughness to that of the original fracture toughness. For the 4-point bend geometry, the healing efficiency simplifies to a ratio of the fracture loads, given by $\eta = P^{Healed} / P^{Original}$. Subsequent to fracture, the specimen undergoes 50 flexural cycles at 50 μm/s, with crosshead amplitude of 100 μm (≈20 N) and an R-ratio of 0.17±0.04. The amplitude of 100 μm is deemed optimal based on visual observation of the fluid within the crack plane. The samples are placed in an oven and are held at 30°C for 48 hr to cure material in the crack plane between the testing cycles.

3.2.7 Fluid Imaging in the Crack Plane

To investigate fluid flow and mixing in the crack plane, a modified binary interpenetrating microvascular specimen geometry is filled with two fluorescently dyed fluids for imaging on a fluorescence microscope. The resin viscosity (1070 cP) is matched with a red-dyed glycerol-water mixture (98.5 w/w% glycerol, 1070 cP) and the hardener viscosity (445 cP) is matched with a green-dyed glycerol-water mixture (96.5 w/w% glycerol, 457 cP). The surface tension of both mixtures is lowered by the addition of 0.05 w/w% Tween 85 surfactant to promote fluid wetting of the crack plane.

The specimen design closely approximates the binary interpenetrating microvascular networks design embedded in a coating-substrate architecture, but is modified in two ways for the imaging experimental set-up. First, to block background fluorescence from the underlying microvascular network, carbon black (<1 w/w%) (Mitsubishi Chemical Corporation) is added to the EPON 828 epoxy resin via ultrasonication prior to the addition of the curing agent. Second, to fracture and rapidly image these specimens, it is

necessary to increase the substrate flexibility and to embrittle the coating. The substrate is made flexible with the addition of 5 w/w% acetone to the Envirotex Lite resin prior to mixing with the hardener. The coating was embrittled through the addition of 7.5 p.p.h. Epikure 3253 to the prior formulation of EPON 828 and 12 p.p.h. diethylenetriamine. During the application of the coating mixture, minimal heating of the fugitive wax in the microvascular networks causes melting and the coating material would infiltrate the networks. Hence, the greater exotherm associated with this coating formulation requires both the crack specimens and the coating mixture to chill at approximately 5°C for 15 min prior to application of the coating material. The coating is cured for 24 hr and then polished to a smooth surface. The coating thickness is measured by a transmission light microscope to verify that the thickness variation from one side to the other is less than 30 μm. The location above the vertical channel access is scored as previously discussed.

The specimen is placed in the 4-point bending geometry, with the downward force applied by hand in a steady manner. Immediately upon cracking, the specimen is placed in the predefined stage location and fluorescent imaging is begun. The initial stages of the crack diffusion are imaged at a higher rate to capture any rapid changes, with reduced imaging rates at longer times (Table 3.1). The location of both the resin and hardener mimics is identified by the local red and green fluorescence intensities, respectively, and the time evolution of fluid mixing in the crack plane is imaged for neighboring underlying spikes. Regions of fluid composition correlating to 1:1 and 2:1 ratio of resin:hardener are filtered according to color, using a ±2.5% color band in Photoshop (Adobe, Inc). Images are also filtered for all compositions within a 1:1 and 2:1 ratio of resin:hardener, corresponding to the compositional range that will cure in a 48 hr period.

Quantitative image analysis is carried out to determine the fraction of the crack width filled with mixed fluid. This fraction is denoted I/I_{max}, where I_{max} corresponds to the crack plane filled with fully mixed fluid. Line plots of the mixed fluid fraction are constructed along the x-distance between neighboring resin- and hardener-mimic fluid inputs. A time series of the mixing fraction at the mid-plane between the resin and hardener-mimic inputs provides an approximate mixing time for full fluid mixing, which occurs when the I/I_{max} value approaches unity in that location.

3.3 Results and Discussion

3.3.1 Dual Fugitive Inks

We pursue the fabrication route shown schematically in Figure 3.1 to produce epoxy substrates with embedded binary interpenetrating microvascular networks. Two fugitive organic inks are required to construct the desired interpenetrating, yet isolated, microvascular networks by direct-write assembly. Next, vertical posts are deposited that connect each underlying network within the substrate, to the coating thereby providing conduits that supply both healing agents to the crack plane when damage occurs. Two key advances in direct-write assembly are required to successfully create these architectures: (1) dual ink deposition and (2) vertical ink writing.

Both fugitive inks must flow through a fine deposition nozzle under high shear, and form self-supporting filaments upon exiting the nozzle. Furthermore, to maintain network isolation, both inks must be removed independently from the epoxy substrate. To meet these challenging demands, we used two fugitive organic inks that possess

similar viscoelastic behavior under ambient (printing) conditions, yet have vastly different temperature-dependent rheological responses.

The primary fugitive ink is composed of a mixture of microcrystalline wax and heavy mineral oil, which represents a modified form of the wax-based ink reported previously.[21, 23] Under ambient conditions, this ink exhibits a plateau shear elastic modulus, G', of 10^5 Pa, and pronounced shear thinning when the applied stress exceeds the shear yield stress, τ_y (Fig. 3.2a). When the temperature is raised to 50°C, both the plateau G' and τ_y are significantly reduced. Above ~80°C, the ink liquefies and can removed from the epoxy matrix under a light vacuum leaving behind the desired microchannels.

The secondary fugitive ink is composed of an aqueous, triblock copolymer solution. The triblock copolymer, known as Pluronic F127, consists of poly(ethylene oxide) (PEO) and poly(propylene oxide) (PPO) arranged in an ABA configuration of $PEO_{106}PPO_{70}PEO_{106}$, with an average molecular weight of $M_W \approx 12{,}600$.[24] The copolymer species assemble into micelles at temperatures above ~10°C, yielding a physical gel when the copolymer concentrations exceeds approximately 20 w/w%.[25-28] For a copolymer concentration of 30 w/w%, a G' plateau value of approximately 10^4 Pa is observed under ambient conditions (Fig. 3.2b). However, unlike the wax-based ink, this copolymer ink softens as the temperature is decreased. Importantly, below the micellization temperature, the secondary fugitive ink becomes fully liquefied, such that the plateau G' is reduced by six orders of magnitude at 8°C.[26]

3.3.2 Vertical Ink Printing

The second key fabrication advance necessary to pursue the fabrication scheme (Fig. 3.1) is vertical ink printing. To deposit vertical features, the ink is printed through a nozzle as it translates along the *z*-axis, with integrated valve-controlled pressure application to repeatedly start and stop ink flow. Vertical ink printing depends critically on the ink elasticity, nozzle diameter (D), and filament height (h). To determine the aspect ratios (h/D) achievable from the primary fugitive ink, we printed vertical features of varying height through a wide range of nozzle diameters (Fig. 3.3). We find that stable vertical features with $h/D \sim 25\text{-}35$ can be produced using nozzles that range from 510 μm to 100 μm in diameter, respectively. As the value of h/D is further increased, the vertical filaments first undergo buckling followed by complete collapse. For the self-healing specimens studied, vertical filaments with an $h/D \sim 15$ were patterned using a 330 μm nozzle.

To understand the observed buckling behavior, we invoke classic concepts of buckling stability under self-weight. The vertical feature must have the weight of each section along its length elastically supported by the sections below. However, at some given height, the column becomes unstable with respect to buckling, such that an infinitesimal perturbation to the feature will cause it to deflect from the vertical position.

To calculate the critical aspect ratio for buckling under self-weight, we assume that the vertical features of interest consist of constant cross-section, are composed of a homogeneous material, and are subject to their own weight with no external applied loads. When the lower end of a column is rigidly fixed and the upper end is free to lateral

and rotational movement, the governing equation for the critical height, h_c, at the onset of buckling is given by:

$$h_c = \left(\frac{9}{4} \frac{EI}{\rho g A} j_{-1/3}^2 \right)^{1/3}, \tag{3.1}$$

where E is the elastic modulus, I is the second moment of inertia, ρ is the column density, g is gravitational acceleration, A is the column cross-sectional area, and $j_{-1/3}$ is the least positive root of the Bessel function to the -1/3 power, approximately equal to 1.8663.[29-32] Using equation 3.1 and assuming the column to be circular in cross-section, the critical length and critical aspect ratio are defined by:

$$h_c = \left(\frac{1.9594 E r^2}{\rho g} \right)^{1/3} \tag{3.2}$$

$$\frac{h_c}{D} = \left(\frac{0.2449 E}{\rho g r} \right)^{1/3}, \tag{3.3}$$

where the wax ink density is ρ=0.92 g cm^{-3}, and $E = (1 + 2\upsilon)G'$, where $\upsilon = 0.5$ and G' is an average of the storage modulus plateau (1.59×10^5 Pa).[33] Above this critical aspect ratio, the vertical features will buckle.

The predicted critical aspect ratio, shown as a function of nozzle diameter in Figure 3.3b, is approximately 25% higher than the observed buckling transition region. The discrepancy between our experimental observations and the predicted behavior likely arise from a combination of the ink rheology and the fabrication method. First, our analysis does not adequately account for the viscoelastic nature of the fugitive ink. As the ink flows through the nozzle, it experiences high shear stresses near the nozzle walls. After deposition, a finite time is needed for the sheared material to recover its plateau modulus. This time, measured by pre-shearing wax ink and probing the recovery after

shear under small strain oscillatory conditions, is found to be greater than 180 s. During this period, the column is subject to buckling at a reduced aspect ratio. Second, although the nozzle vertically patterns the ink filaments, as the applied pressure is released the nozzle position moves sideways slightly prior to the filament disconnecting from the nozzle. This motion likely introduces an additional driving force for instability, which lowers the maximum aspect ratio for stable filamentary printing.

3.3.3 Direct Ink Writing of Binary Interpenetrating Microvascular Networks

The binary interpenetrating microvascular network design (Fig. 3.1) is fabricated via direct-write assembly of two fugitive inks. In this approach, the primary and secondary inks are mounted side-by-side on a 3D robotic deposition stage and each ink is patterned independently. The primary ink is used to define the resin (Fig. 3.4a) and hardener (Fig. 3.4c) microvascular networks with vertical conduits, while the secondary fugitive ink serves to separate each network so they remain isolated in the final coating/substrate architecture (Fig. 3.4b). The vertical conduits are deposited through a 330 μm nozzle, with up to 420 vertical features printed per specimen.

To create the desired self-healing specimens, we first fill the void space between patterned ink filaments with a low-viscosity epoxy resin.[13, 14, 21] Next, we cut open the specimen (Fig. 3.5a) to remove the secondary fugitive ink from the epoxy substrate by cooling the specimen to approximately 5°C (Fig. 3.5b). The resulting microchannels are then infiltrated with the epoxy resin and the specimen is again cured. The primary fugitive ink, whose pattern defines the two interpenetrating microvascular networks, remains within the substrate, but is now fully surrounded by the epoxy matrix (Fig. 3.5c). Finally, upon heating the specimen to approximately 80°C, the primary fugitive ink is

liquefied and removed to yield the desired interpenetrating, yet isolated, microvascular networks (Fig. 3.5d).

3.3.4 Repeated Healing via Binary Interpenetrating Microvascular Networks

To investigate autonomic healing of coating/substrate architectures with interpenetrating microvascular architectures, we fill each network with one component of a two-part epoxy chemistry previously identified by Toohey *et al*.[22] Specifically, one network is filled with the epoxy resin, while the other network is filled with epoxy hardener. Because the networks are isolated from one another within the substrate, these fluids will only react when they come in contact within the crack plane of the coating layer. The samples are easy to infiltrate with resin or hardener and remove entrained air due to the simplified design of a single inlet and outlet per network, unlike the previous design that required multiple inlets and outlets for each alternating network.[22] Eight specimens are produced, each of which contain vertical posts that deliver a 2:1 ratio of resin:hardener approximating the optimal stoichiometry (2.2:1).[34]

Prior to mechanical testing, the crack location is specifically defined by producing a horizontal notch on the coating surface using a scribe tool under constant load, which is placed above an array of vertical posts beneath the coating (Fig. 3.6). Following the procedure reported previously,[14] each specimen is then placed in a four-point bend geometry and loaded until the coating fractures (Fig. 3.7). There is a small (10%) difference between the critical loads observed for specimens that have been scored (114±23 N) relative to those that are unscored (129±57 N). Scoring the specimen surface increases repeatability and produces a single straight crack that propagates through the

coating to the coating/substrate interface, yet does not propagate into the underlying substrate.

Once the crack reaches this interface and makes contact with the interpenetrating microvascular network, both epoxy resin and hardener wick into the crack plane due to capillary forces. The specimens are then subject to cyclic flexural loading (50 cycles at 100 μm displacement) to enhance mixing of the fluids in the crack plane prior to healing at 30°C for 48 hr. After healing, each specimen is tested again, and the original crack reopens at a new critical load. This process is repeated for 30 cycles. The load curves for the original crack and the 30 subsequent heal cycles are shown for a representative specimen in Figure 3.8a. These data demonstrate the remarkable ability of interpenetrating microvascular networks to enable repeated healing of a single crack for thirty sequential cycles.

Healing was tested for eight specimens for 30 consecutive cycles, for a total of 240 cycles. During testing, there was no detectable acoustic emission event in nearly 33% of the cycles and those specimens were considered to have not healed for that cycle. The fraction of non-healing cycles increased with increasing number of healing cycles, rising from an initial average of 0.25 to 0.46 for the last three cycles (Fig. 3.8b). Similar to previously reported results,[22] we observe no increase in the healing loads with mixing, but rather an increase in the number of consecutive healing cycles.

The healing efficiency, η, is defined as the ratio of the coating fracture toughness for a specific heal cycle to the original fracture toughness. For the specimen geometry used in this study, the healing efficiency simplifies to a ratio of the heal fracture load to the original fracture load, calculated as $\eta = P^{Healed} / P^{Original}$. The average healing efficiency

for the eight specimens tested is provided in Fig. 3.8c. Non-healed samples were assigned a value of $\eta = 0$ and were averaged with the healed samples for each test cycle. The value of η approaches 100% in some early cycles, and a healing efficiency of ~50% is retained after 30 cycles of healing. This compares favorably with the previous self-healing microcapsule and single-network geometries, also shown in Fig. 3.8c. The interpenetrating network specimens display healing efficiencies comparable to that of the microcapsule specimen for the initial healing cycle, demonstrating no sacrifice in healing efficiency due to the new geometry. For the first seven cycles, the interpenetrating network matches or exceeds the healing efficiency of the single-network geometry, again showing no sacrifice in healing efficiency with the new design. Finally, the total number of observed healing cycles is unparalleled, demonstrating the superiority of this new interpenetrating microvascular network design.

The variability in self-healing behavior of these samples is likely due to differences in fluid transport and diffusive mixing within the crack plane. Toohey and coworkers examined the crack plane under scanning electron microscopy and discovered incomplete mixing, with preferential polymerization located nearest the resin channels.[22] However, no direct observations have been made of the initial stages of fluid flow and mixing within the crack plane, which would aid in designing improved self-healing embedded microvascular architectures.

3.3.5 Fluid Flow and Mixing in Crack Plane

To better understand the variability in self-healing behavior, we analyze the microscale mixing of two model fluids in the crack plane that are directly observed by fluorescence microscopy. Ideally, these model fluids should match the resin and

hardener healing agent viscosities, yet, to simplify analysis of initial fluid flow and mixing, be inert to avoid polymerization effects. These requirements are fulfilled by dyed glycerol-water mixtures, whose respective viscosities match those of the resin and hardener healing agents, and whose surface tension are tuned to be equal. A linear dependence of intensity on concentration, predicted to be $I_{green} / I_{red} = \phi_{green} / \phi_{red}$, is observed from 10 vol% < ϕ_{red} < 80 vol% (Fig. 3.9). This covers the range of resin volume fractions required for proper epoxy curing. In these networks, vertical features are arrayed in a ratio of 2:1 resin:hardener to supply the crack plane with fluid, analogous to the interpenetrating self-healing architectures (Fig. 3.10). Our observations of microscale mixing behavior reveal that there are competing transport phenomena that affect whether strong mixing, and thus healing, takes place.

Figure 3.11a shows representative fluorescent images acquired on a specimen that demonstrates good fluid mixing within the crack plane. The image shows the location between two neighboring fluid conduits, one that contains the resin-mimic (red) and the other that contains the hardener-mimic (green). Prior to cracking, no fluorescence is observed, indicating that the fluids remain sequestered within the microchannels. After crack formation, the dyed mixtures enter the crack plane and wick towards one another via capillary action. At t = 40 s, the fluids contact and mixing begins. Intermixing proceeds quickly and by t = 5 min, the fluids have effectively mixed so that the local stoichiometry lies mostly within the curable range (resin:hardener = 1:1 to 2:1) for the healing agents. This mixing is quantified with line plots of the fraction of fluid mixed along the length of the crack plane, which show that this value approaches unity across the entire imaged region by t = 5 min (Fig 3.11b). Likewise, the mixing time evolution at

the midplane between fluid inputs indicates that the fluid fully mixes in this location by $t \approx 100$ s (Fig. 3.11c). These results indicate this specimen would likely demonstrate strong healing during mechanical testing.

Figure 3.12 shows crack-plane images for specimens that would likely not exhibit autonomic healing of damage in the crack coating. As seen, the crack plane is dominated primarily by either the hardener- or the resin-mimic, with little mixing observed after 5 minutes and even up to an hour after the crack opening. This behavior contrasts sharply with the nearly complete mixing observed for the other specimen after 5 min (Figure 3.11). This divergent mixing behavior may explain the inconsistent healing witnessed in binary interpenetrating microvascular self-healing samples, where even for the first observed cycle approximately 25% of the samples do not exhibit healing.

When the specimens are imaged from the side, the fluid is observed to exit the vertical conduits and enter the crack plane immediately after it forms. During this fluid transport process, air occasionally penetrates the vertical feature(s), thereby replacing the drained fluid. During this process, bubbles form that prevent additional fluid from entering the crack plane at those locations, such that the crack plane preferentially fills with fluid from those conduits that are devoid of bubbles. This phenomenon occurs more frequently in specimens that experience higher flexural loads prior to crack formation. In these samples, the higher bending strain at the time of fracture will create a wider crack with greater volume for fluid infiltration. Fluid will quickly fill the crack and may not be adequately supplied by the underlying network, thus entrapping air. Moreover, when the flexural load is released, the crack width will reduce and may push fluid and any entrapped air from the surface to deeper within the network. The reduction in the elastic

modulus of the substrate material for imaging specimens will also permit greater surface strain for a given flexural load and may explain the lack of observed bubble formation within the vertical conduits in self-healing specimens.

3.3.6 Analysis of Fluid Flow and Mixing

There are four relevant timescales for fluid flow and diffusion within the crack plane: (1) the capillary flow time, t_{flow}, (2) the taper migration time, t_{taper}, (3) the diffusion time, $t_{diffusion}$ and (4) the vertical conduit fill time, t_{fill}. The first timescale, t_{flow}, describes the time required for fluid(s) to wick via capillary forces into and fill the crack plane. Immediately after crack formation within the brittle coating, capillarity drives each fluid from the vertical conduits (330 μm in diameter) into the crack plane (width ≈ 45–75 μm). The pressure drop (ΔP) that drives fluid flow is given by:

$$\Delta P = P_{crack} - P_{network} \tag{3.4}$$

$$\Delta P = 2\gamma \cos\theta\left(\frac{1}{D_1} + \frac{1}{D_2}\right) - 2\gamma \cos\theta\left(\frac{1}{R}\right) \tag{3.5}$$

where γ is the liquid-vapor surface energy, θ is the contact angle, D_1 and D_2 are the principal diameters of curvature for the crack opening, and R is the radius of the network channels. This driving force is opposed by the viscous resistance to fluid flow, as described by the Hagen-Poiseuille relationship for cylindrical channels:

$$\Delta P = \frac{32\mu L_{network} U_{network}}{D_{network}^2} \tag{3.6}$$

where μ is the dynamic viscosity, $L_{network}$ is the fluid path length within the network, and $U_{network}$ is the linear velocity of the fluid in the network. Equating Eqs. (3.5) and (3.6), and assuming conservation of fluid volume, the linear velocity of fluid U_{flow} is calculated for crack widths characteristic of those observed specimens for self-healing and direct

imaging. For the range of crack widths from w = 15 to 75 μm, t_{flow} varies over an order of magnitude, from 0.1 s to 5 s for the resin-mimic, respectively (see Table 3.2). The predicted times are in good agreement with direct imaging of fluid flow, in which cracks are filled within 10 s. Note, t_{flow} for the hardener-mimic is approximately half that of the resin-mimic due to their viscosity difference.[35] This predicted difference in capillary flow times is also observed experimentally, where we find that the hardener-mimic fluid is more likely to dominate within the crack plane.

The second timescale, t_{taper}, describes the motion of fluid within a crack plane whose width is not uniform. Ideally, the four-point bend test should yield uniform crack widths; however, sometimes the crack propagates through the brittle coating into the matrix, leading to a crack that is wider in that region. The pressure drop across a crack of tapered width and of uniform thickness is given by:

$$\Delta P = 2\gamma \cos\theta \left(\left(\frac{1}{D_{w,1}} + \frac{1}{D_t} \right) - \left(\frac{1}{D_{w,2}} + \frac{1}{D_t} \right) \right) \tag{3.7}$$

$$\Delta P = 2\gamma \cos\theta \left(\frac{1}{D_{w,1}} - \frac{1}{D_{w,2}} \right) \tag{3.8}$$

where $D_{w,1}$ and $D_{w,2}$ are the crack widths at locations 1 and 2 respectively, and D_t is the coating thickness. The viscous resistance to flow for rectangular channels is given by:

$$\Delta P = 4 f\left(\frac{a}{b}\right) \frac{\mu L U_{crack}}{b^2} \tag{3.9}$$

where $f(a/b)$ is a characteristic constant, $2a$ and $2b$ are the sides of the rectangular cross-section, μ is the dynamic viscosity, L is the fluid plug length, and U_{crack} is the linear velocity of the fluid.[36] Equating eqs. 3.8 and 3.9 yields:

$$U_{taper} = \frac{\gamma \cos\theta}{\mu} \frac{b^2}{2f(a/b)L}\left(\frac{1}{D_{w,1}} - \frac{1}{D_{w,2}}\right) \tag{3.10}$$

Calculated t_{taper} values for a variety of crack tapers are provided in Table 3.3. As the crack width becomes more uniform, t_{taper} increases due to lower fluid velocity. For a representative length (L=2 mm) and taper ($D_{w,1}$=68 μm, $D_{w,2}$=58 μm), the fluid is predicted to migrate at a velocity of 420 $\mu\mathrm{m/s}$ within this non-uniform crack. By contrast, the experimental data in Figure 3.11 reveals a front of resin-mimic (red) advancing into the hardener-mimic (green) region at 21 $\mu\mathrm{m/s}$. Hence, it appears likely that fluid migration within the crack is limited by the supply of fluid from the underlying microvascular network, since $t_{flow} \approx 2t_{taper}$.

The third timescale, $t_{diffusion}$, defines the time for a given fluid to diffuse across a characteristic length scale, which in this case corresponds to half the center-to-center distance between vertical conduits (500 μm). The Einstein-Smoluchowski equation for molecular diffusion is given by:

$$t_{diffusion} = \frac{\langle x^2 \rangle}{2D} \tag{3.11}$$

where $\langle x^2 \rangle$ is the root-mean square net displacement of the molecule. Using Eq. (3.11) along with reported values for glycerol-water diffusion coefficients,[37-40] we estimate a $t_{diffusion}$~3 hr, which is substantially longer than both t_{flow} and t_{taper}.

The final timescale of interest, t_{fill}, defines the time required to fill the partially drained vertical conduits with fluid from the network, thereby circumventing bubble formation. The pressure drop across the vertical conduits and the horizontal channels within the network is given by:

$$\Delta P = 2\gamma \cos\theta \left(\frac{1}{R_{vertical}} - \frac{1}{R_{network}} \right) \tag{3.12}$$

where $R_{vertical}$ and $R_{network}$ are their respective radii of curvature. The pressure drop due to the viscous resistance to fluid flow is:

$$\Delta P = 8\mu \left(\frac{L_{network} U_{network}}{R_{network}^2} + \frac{L_{vertical} U_{vertical}}{R_{vertical}^2} \right) \tag{3.13}$$

where $L_{network}$ and $L_{vertical}$ are the channel lengths in the underlying microvascular network. Solving for the fluid velocity $U_{vertical}$ by equating Eqs. (3.12) and (3.13) allows calculation of a fill time t_{fill} to maintain fluid within the vertical conduits (~1 mm), i.e., to prevent bubble formation. For the current network design, $t_{fill} = \infty$, since the vertical conduits and horizontal channels possess the same diameter. This is consistent with experimental observations that bubbles persist in the vertical conduits for at least 24 hr. In microvascular networks that suffer from bubble formation, bio-inspired hierarchical designs are needed that lead to a finite t_{fill}. Hierarchical networks, such as those based on the biological principle of Murray's law [41] will exhibit a preferential filling of the smallest capillary channels at the expense of channels with larger diameters.

3.4 Conclusions

In summary, we have demonstrated the ability to fabricate embedded binary interpenetrating microvascular networks by extending the direct ink write technique with dual and vertical ink printing. Using these two key advancements, novel coating/substrate architectures were created for application to self-healing materials that can independently supply multiple healing agents to a given damage site. This platform enables the use of inexpensive two-part epoxies to achieve repeated healing of a single

damaged location in excess of 30 continuous cycles. Imaging studies are performed with resin and hardener mimics to investigate mixing behavior within the crack plane. Results indicate that short timescale transport processes, such as capillary transport between the network to the crack plane and within a tapered crack plane, dominate the mixing relative to long timescale processes, such as diffusion.

3.5 References

1. G. B. West, J. H. Brown, and B. J. Enquist, *A general model for the structure and allometry of plant vascular systems*. Nature, 1999, 400, p. 664-667.
2. A. Roth-Nebelsick, D. Uhl, V. Mosbrugger, and H. Kerp, *Evolution and Function of Leafe Venation Architecture: A Review*. Annals of Botany, 2001, 87, p. 553-566.
3. N. M. Holbrook and M. A. Zwieniecki, *Vascular Transport in Plants,* 2005: Elsevier Academic Press.
4. L. Sack and K. Frole, *Leaf Structural Diversity Is Related to Hydraulic Capacity in Tropical Rain Forest Trees*. Ecology, 2006, 87, p. 483-491.
5. G. B. West, J. H. Brown, and B. J. Enquist, *A General Model for the Origina of Allometric Scaling Laws in Biology*. Science, 1997, 276, p. 112-126.
6. B. Sapoval, M. Filoche, and E. R. Weibel, *Smaller is Better - but Not Too Small: A Physical Scale for the Design of the Mammalian Pulmonary Acinus*. Proceedings of the National Academcy of Sciences, 2002, 99, p. 10411-10416.
7. R. K. Jain, *Normalization of Tumor Vasculature: An Emerging Concept in Antiangiogenic Therapy*. Science, 2005, 307, p. 58-62.
8. N. W. Choi, M. Cabodi, B. Held, J. P. Gleghorn, L. J. Bonassar, and A. D. Stroock, *Microfluidic scaffolds for tissue engineering*. Nature Materials, 2007, 6, p. 908-915.
9. M. K. Runyon, B. L. Johnson-Kerner, C. J. Kastrup, T. G. V. Ha, and R. F. Ismagilov, *Propagation of Blood Clotting in the Complex Biochemical Network of Hemostasis Is Described by a Simple Mechanism*. Journal of the American Chemical Society, 2007, 129, p. 7014-7015.
10. J. M. Higgins, D. T. Eddington, S. N. Bhatia, and L. Mahadevan, *Sickle Cell Vasoocclusion and Rescue in a Microfluidic Device*. Proceedings of the National Academy of Sciences, 2007, 104, p. 20496-20500.
11. D. Lim, Y. Kamotani, B. Cho, J. Mazumder, and S. Takayama, *Fabrication of microfluidic mixers and artificial vasculatures using a high-brightness diode-pumped Nd:YAG laser direct write method*. Lab on a Chip, 2003, 3, p. 318-323.
12. D. H. Kam and J. Mazumder, *Three-dimensional biomimetic microchannel network by laser direct writing*. Journal of Laser Applications, 2008, 20, p. 185-191.

13. D. Therriault, S. R. White, and J. A. Lewis, *Chaotic mixing in three-dimensional microvascular networks fabricated by direct-write assembly*. Nature Materials, 2003, 2, p. 265-272.
14. K. S. Toohey, N. R. Sottos, J. A. Lewis, J. S. Moore, and S. R. White, *Self-healing materials with microvascular networks*. Nature Materials, 2007, 6, p. 581-585.
15. C. J. Hansen, W. Wu, K. S. Toohey, N. R. Sottos, S. R. White, and J. A. Lewis, *Self-healing Materials with Interpenetrating Microvascular Networks*. Advanced Materials, 2009, 21, p. 4143-4147.
16. P. Martin, *Wound Healing - Aiming for Perfect Skin Regeneration*. Science, 1997, 276, p. 75-81.
17. E. N. Brown, S. R. White, and N. R. Sottos, *Retardation and Repair of Fatigue Cracks in a Microcapsule Toughened Epoxy Composite - Part II: In situ Self-Healing*. Composites Science and Technology, 2005, 65, p. 2474-2480.
18. R. S. Trask, H. R. Williams, and I. P. Bond, *Self-Healing Polymer Composites: Mimicking Nature to Enhance Performance*. Bioinspiration and Biomimetics, 2007, 2, p. P1-P9.
19. A. S. Jones, J. D. Rule, J. S. Moore, N. R. Sottos, and S. R. White, *Life Extension of Self-Healing Polymers with Rapidly Growing Fatigue Cracks*. Journal of the Royal Society Interface, 2007, 4, p. 395-403.
20. J. P. Youngblood and N. R. Sottos, *Bioinspired Materials for Self-Cleaning and Self-Healing*. MRS Bulletin, 2008, 33, p. 732-738.
21. D. Therriault, R. F. Shepherd, S. R. White, and J. A. Lewis, *Fugitive inks for direct-write assembly of three-dimensional microvascular networks*. Advanced Materials, 2005, 17, p. 395-399.
22. K. S. Toohey, C. J. Hansen, J. A. Lewis, S. R. White, and N. R. Sottos, *Delivery of two-part self-healing chemistry via microvascular networks*. Advanced Functional Materials, 2009, 19, p. 1399-1405.
23. D. Therriault, S. R. White, and J. A. Lewis, *Rheological behavior of fugitive organic inks for direct-write assembly*. Applied Rheology, 2007, 17, p. 10112-10120.
24. E. Hecht and H. Hoffman, *Interaction of ABA Blcok Copolymers with Ionic Surfactants in Aqueous Solution*. Langmuir, 1994, 10, p. 86-91.
25. G.-E. Yu, Y. Deng, S. Dalton, Q.-G. Wang, D. Attwood, C. Price, and C. Booth, *Micellisation and Gelation of Triblock Copoly(oxyethylene/oxypropylene/ oxyethylene), F127*. Journal of the Chemical Society, Faraday Transactions, 1992, 88, p. 2537-2544.
26. P. Linse and M. Malmsten, *Temperature-Dependent Micellization in Aqueous Block Copolymer Solutions*. Macromolecules, 1992, 25, p. 5434-5439.
27. M. Bohorquez, C. Koch, T. Trygstad, and N. Pandit, *A Study of the Temperature-Dependent Micellization of Pluronic F127*. Journal of Colloid and Interface Science, 1999, 216, p. 34-40.
28. J. J. Escobar-Chávez, M. López-Cervantes, A. Naïk, Y. N. Kalia, D. Quintanar-Guerrero, and A. Ganem-Quintanar, *Applications of Thermoreversible Pluronic F-127 Gels in Pharmaceutical Formulations*. Journal of Pharmacy and Pharmaceutical Sciences, 2006, 9, p. 339-358.

29. K. Kato, *Mathematical Investigation on the Mechanical Problems of Transmission Line*. Journal of the Japan Society of Mechanical Engineers, 1915, 19, p. 41.
30. J. Ratzersdorfer, *Die Knickfestigkeit von Stäben und Stabwerken*. J. Springer, 1936, ch. 3, p. 107-109.
31. S. J. Cox and C. M. McCarthy, *The shape of the tallest column*. Society for Industrial and Applied Mathematics, 1998, 29, p. 547-554.
32. W. H. Duan and C. M. Wang, *Exact Solution for Buckling of Columns Including Self-Weight*. Journal of Engineering Mechanics, 2008, 134, p. 116-119.
33. J. E. Smay, J. Cesarano, and J. A. Lewis, *Colloidal inks for directed assembly of 3-D preiodic structures*. Langmuir, 2002, 18, p. 5429-5437.
34. H. R. Williams, R. S. Trask, and I. P. Bond, *Self-Healing Sandwich Panels: Restoration of Compressive Strength After Impact*. Composites Science and Technology, 2008, 68, p. 3171-3177.
35. E. W. Washburn, *The dynamics of capillary flow*. The Physical Review, 1921, 17, p. 273-283.
36. L. G. Loitsyanskii, *Mechanics of Liquids and Gases*. International Series of Monographs in Aeronautics and Astronautics, ed. W.P.J. R. T. Jones. Vol. 6. 1966, London: Pergamon Press.
37. F. H. Garner and P. J. M. Merchant, *Diffusivities of associated compounds in water*. Transactions of the Institution of Chemical Engineers, 1961, 39, p. 397-408.
38. G. O. Y. Nishijima, *Diffusion in glycerol-water mixture.* Bulletin of the Chemical Society of Japan, 1960, 33, p. 1649-1651.
39. V. A. Marinin, *Diffusion coefficients of some substances in glycerol alcohol mixtures.* Zhurnal Fizika Khimii, 1955, 29, p. 1564-1568.
40. G. D'Errico, O. Ortona, F. Capuano, and V. Vitagliano, *Diffusion Coefficients for the Binary System Glycerol + Water at 25 C. A Velocity Correlation Study.* Journal of Chemical Engineering Data, 2004, 49, p. 1665-1670.
41. W. Wu, C. J. Hansen, A. M. Aragón, P. H. Geubelle, S. R. White, and J. A. Lewis, *Direct-write assembly of biomimetic microvascular networks for efficient fluid transport*. Soft Matter, 2010, 6, p. 739-742.
42. S. R. White, N. R. Sottos, P. H. Geubelle, J. S. Moore, M. R. Kessler, S. R. Sriram, E. N. Brown, and S. Viswanathan, *Autonomic healing of polymer composites*. Nature, 2001, 409, p. 794-797.

3.6 Tables

Table 3.1. Imaging rates for crack-plane diffusion experiments

Time from initial crack initiation [min]	Imaging rate [min/capture]
0 – 2	0.1
2 – 10	0.5
10 – 20	1
20 – 60	5

Table 3.2. Values of $t_{capillary}$ into crack plane from 330 μm channels

Crack width [μm]	Resin-mimic, t_{wick} [s]	Hardener-mimic, t_{wick} [s]
15	0.12	0.07
30	0.50	0.28
45	1.2	0.67
60	2.4	1.3
75	4.2	2.3

Table 3.3. Values of t_{taper} within a crack of non-uniform width, with 330 μm conduits, a 330 μm path length and a 500 μm migration length.

Crack width [μm]		Resin-mimic, t_{plane} [s]	Hardener-mimic, t_{plane} [s]
Wide end	Narrow end		
30	15	0.016	0.007
	20	0.03	0.013
	25	0.08	0.03
	29	0.45	0.19
75	60	0.15	0.06
	65	0.24	0.10
	70	0.52	0.22
	74	2.77	1.18

Table 3.4. Values of $t_{diffusion}$ for varying center-to-center spacings between vertical conduits

Center-to-center spacing [mm]	Resin-mimic, $t_{diffusion}$ [h]	Hardener-mimic, $t_{diffusion}$ [h]
0.5	0.82	0.76
1	3.3	3.0
2	13.2	12.1

3.7 Figures

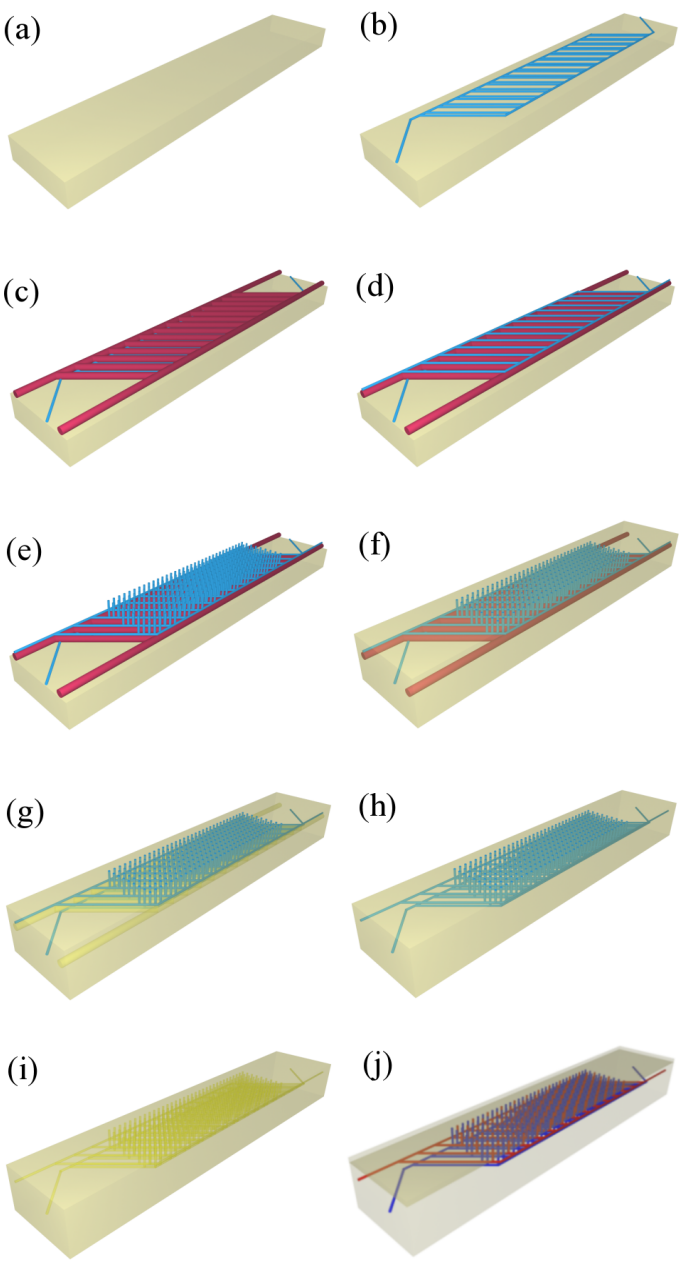

Figure 3.1. Schematic view of the dual fugitive ink process. (a) An epoxy substrate is leveled for writing. (b) Wax ink (blue) is deposited to form one microvascular network. (c) Pluronic ink (red) is deposited to separate microvascular networks. (d) Wax ink is deposited to form the second microvascular network. (e) Wax ink vertical features are printed in connection with both networks. (f) Void space is infiltrated with low-viscosity epoxy. (g) After matrix curing, pluronic ink is removed. (h) Void space is re-infiltrated with low-viscosity epoxy. (i) Wax ink from both microvascular networks is removed. (j) Microvascular networks are filled with epoxy resin (blue) in one network and hardener (red) in the second network.

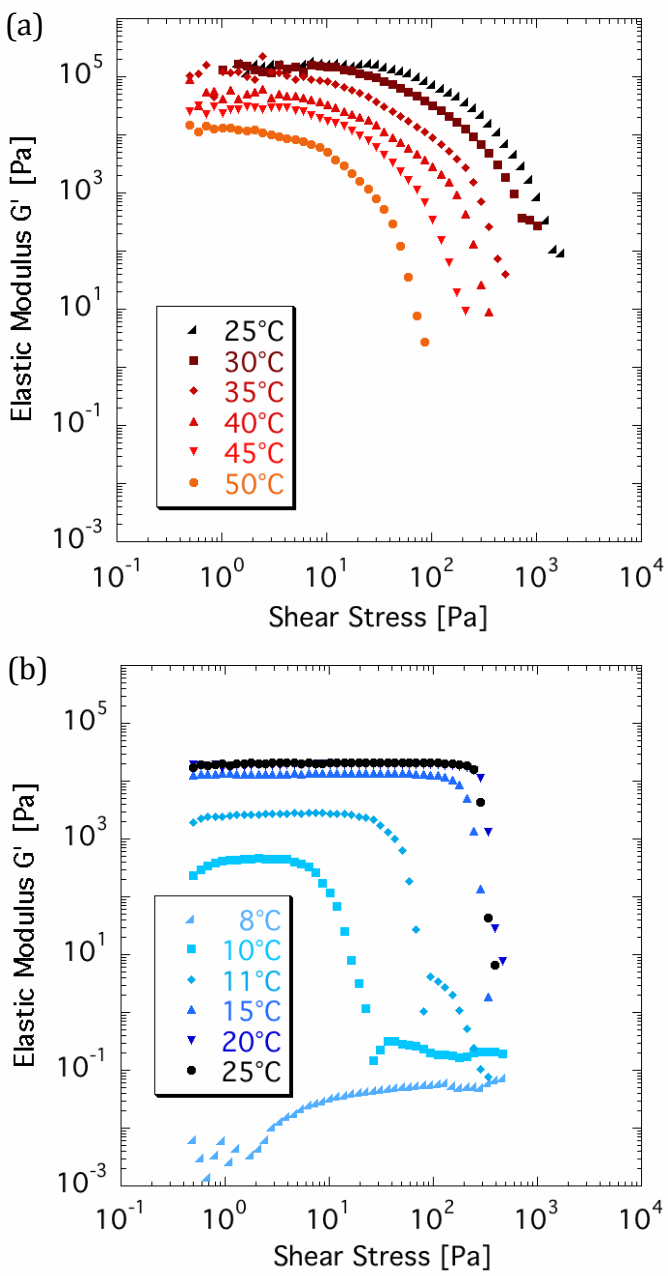

Figure 3.2. Log-log plots of shear elastic modulus as a function of applied shear stress for (a) wax- and (b) pluronic-based fugitive inks at varying temperatures.[15]

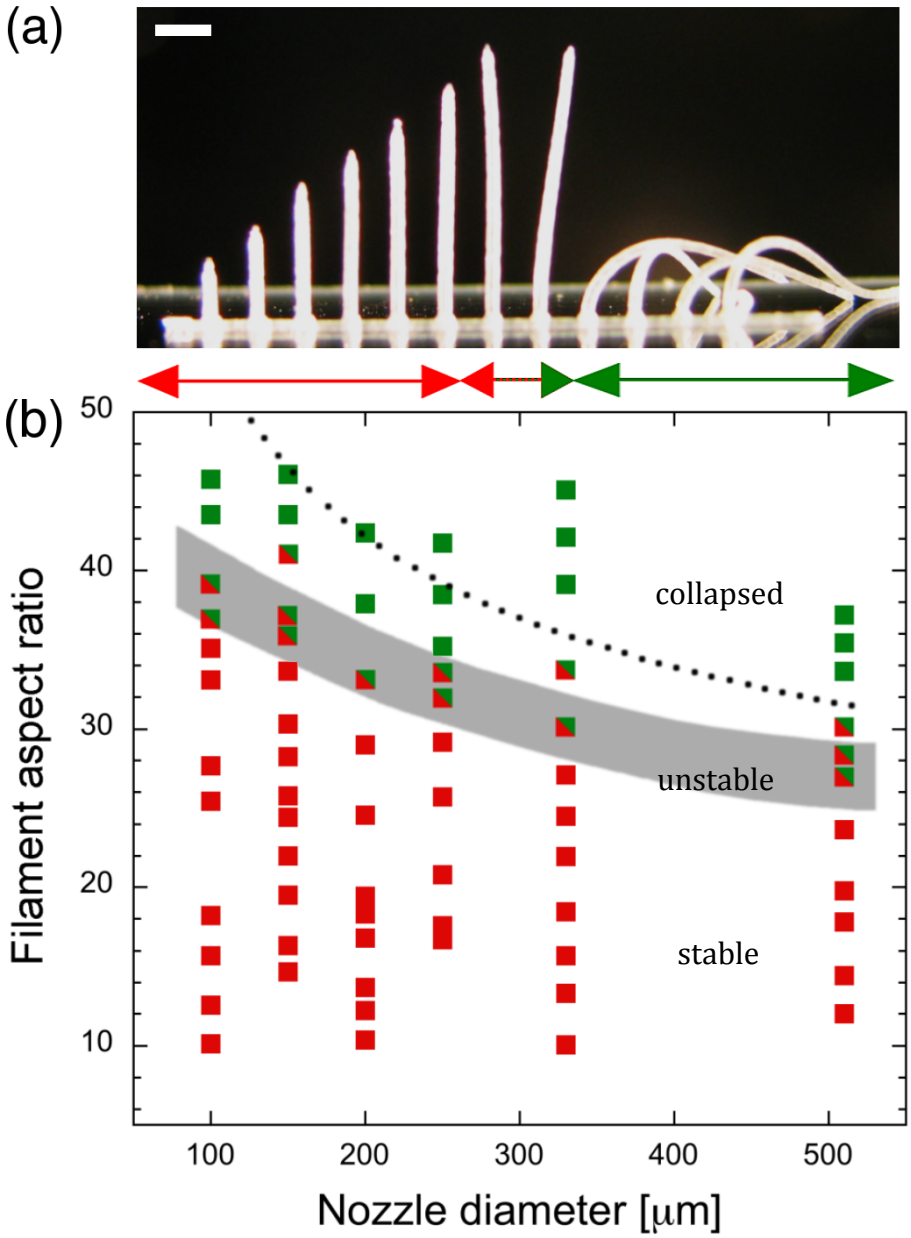

Figure 3.3. (a) Optical image of printed vertical features with varying aspect ratios that demonstrate the transition from stable to buckled form, scale bar 1 mm. (b) Stability map of printed vertical features. Stable features (red squares) become unstable at increasing aspect ratios (red/green squares), finally collapsing at yet higher aspect ratios (green squares). Prediction for onset of buckling under self-weight for linear elastic materials is denoted by the dotted line.

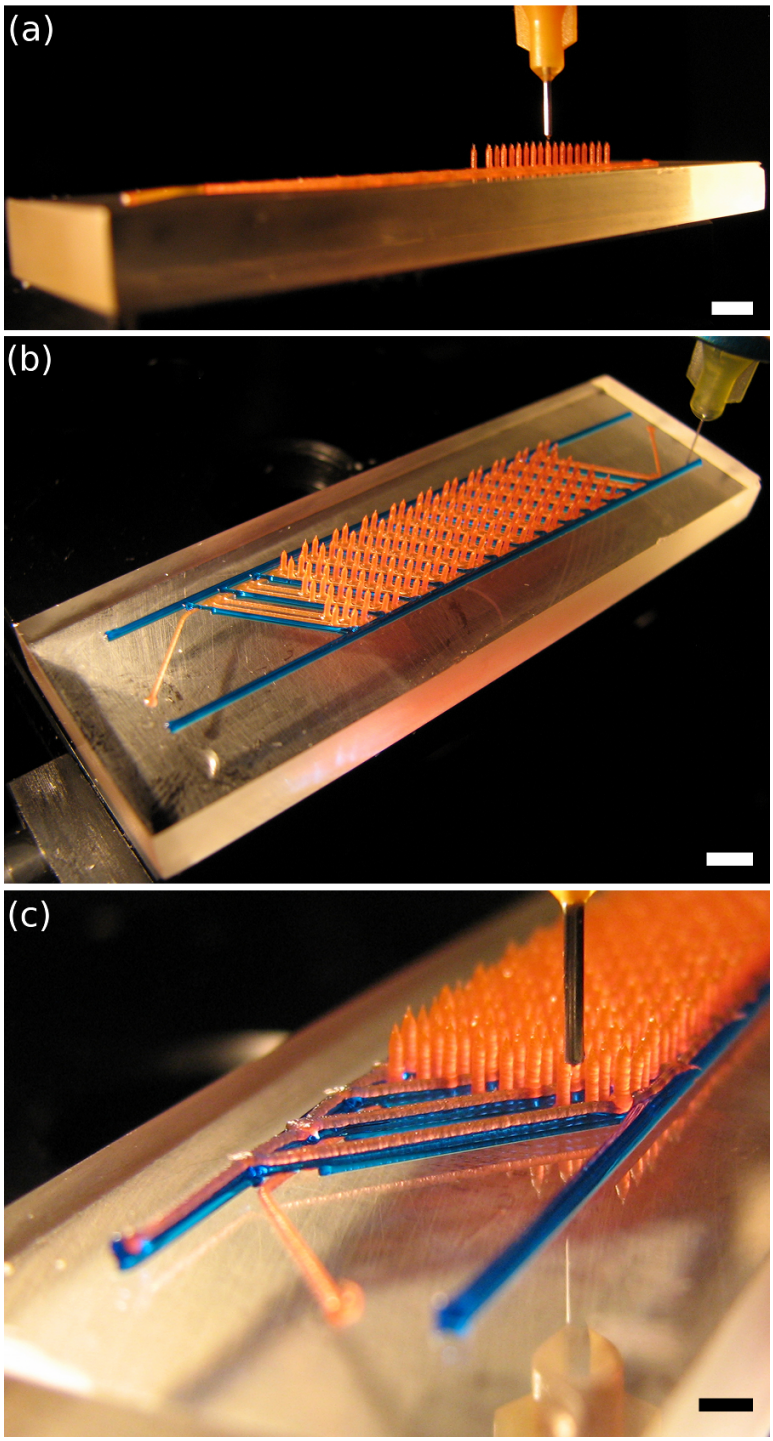

Figure 3.4. Interpenetrating microvascular network fabricated by direct-write assembly of wax (orange)- and pluronic (blue)-based fugitive inks. Printing of (a) the wax ink network for resin channels (scale bar = 2 mm), followed by (b) the pluronic ink spacer network (scale bar = 2 mm), and finally (c) the wax ink network for hardener network deposited on top of pluronic (scale bar = 1 mm).

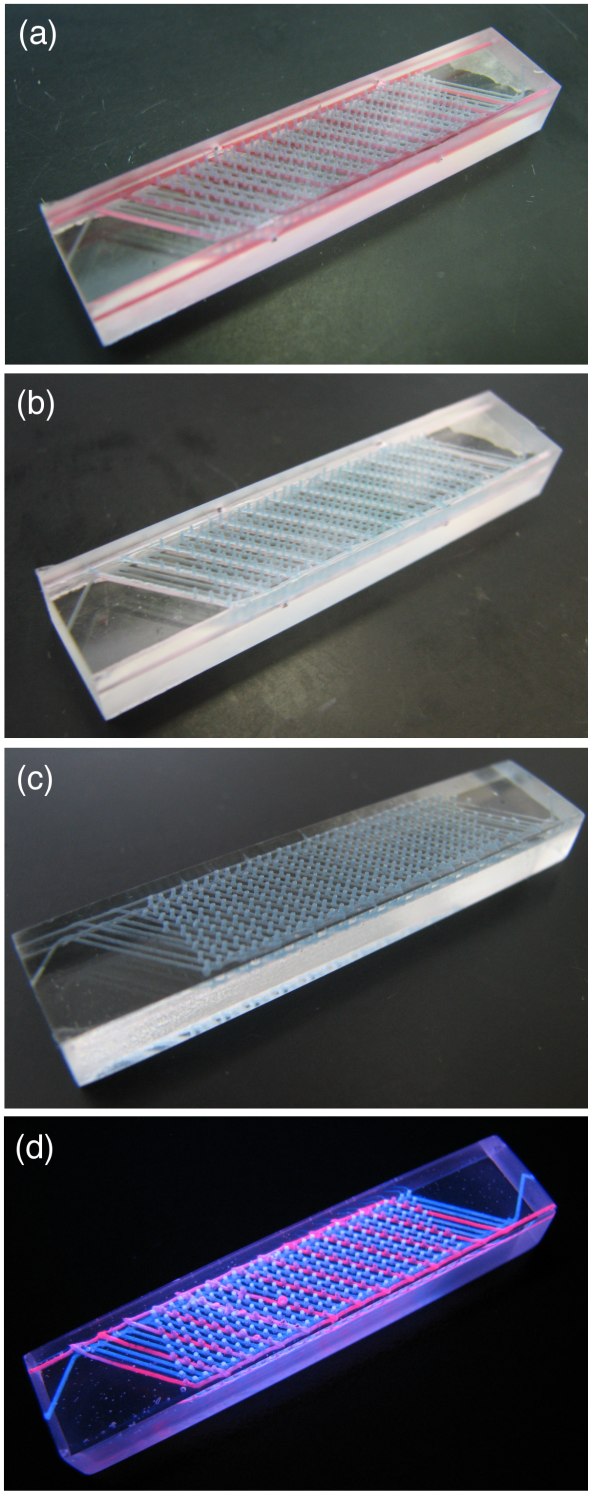

Figure 3.5. Images of interpenetrating self-healing specimens. (a) Specimen with wax (blue) and pluronic (red) inks embedded in epoxy matrix. (b) Specimen with pluronic ink removed. (c) Specimen reinfiltrated with epoxy matrix to remove pluronic network porosity. (d) Interpenetrating networks filled with different fluid compositions, with blue in resin network and red in curing agent network.

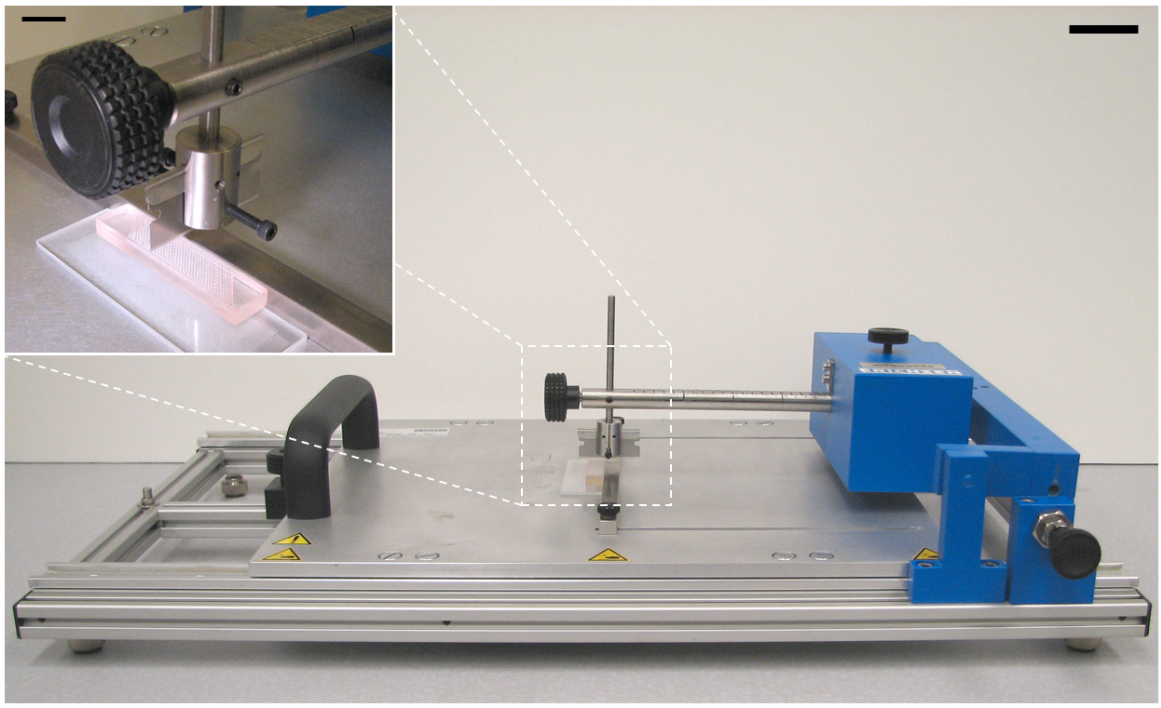

Figure 3.6. Constant load test panel scratcher with razor blade scribe (scale bar = 50 mm). Inset: Razor blade scribe positioned over row of vertical spikes (scale bar = 15 mm).

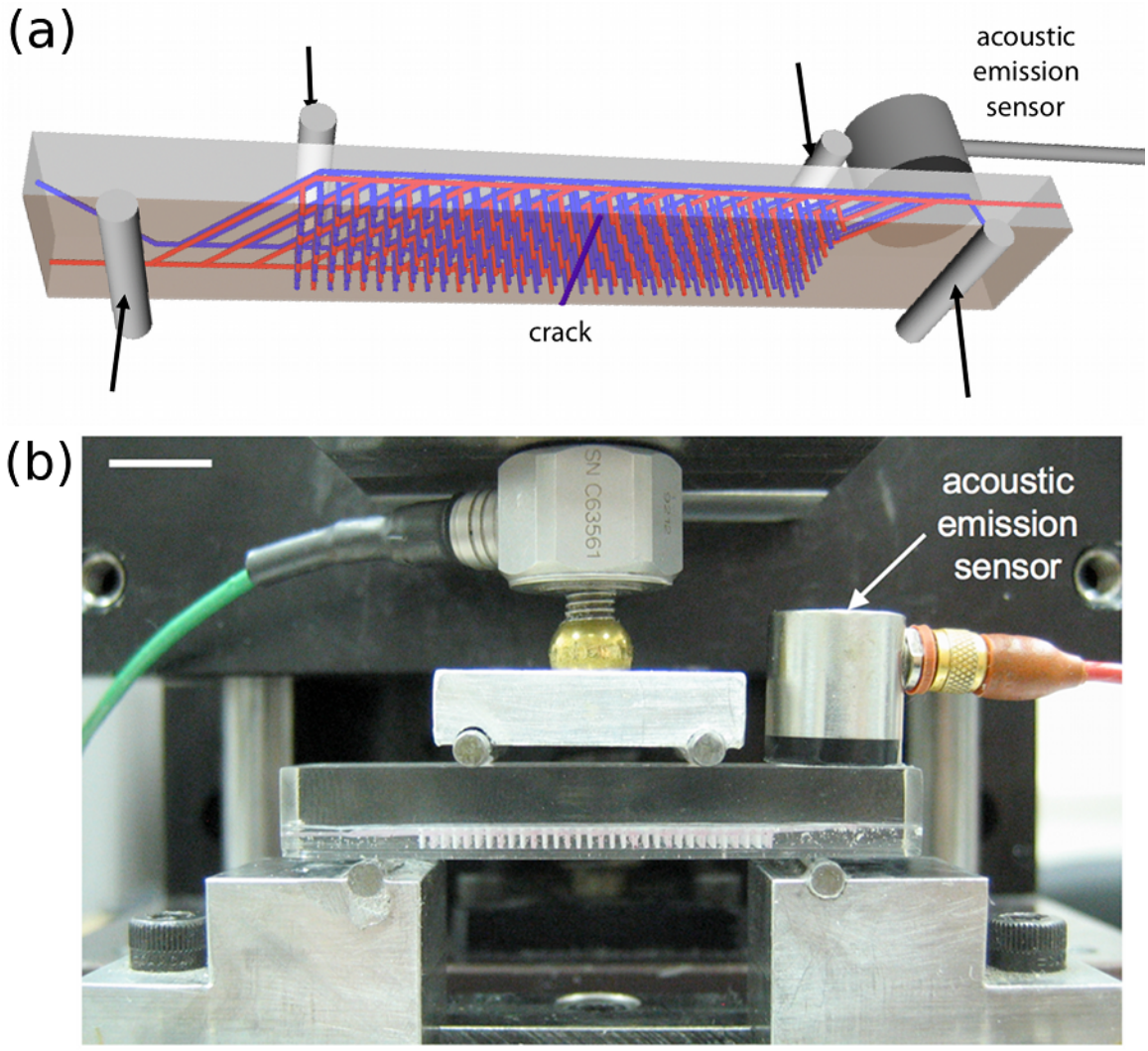

Figure 3.7. (a) Schematic of interpenetrating network sample in 4-point bending with crack formation in brittle coating layer. (b) Binary interpenetrating network specimen placed in 4-point bend geometry with acoustic emission sensor (scale bar = 10 mm).

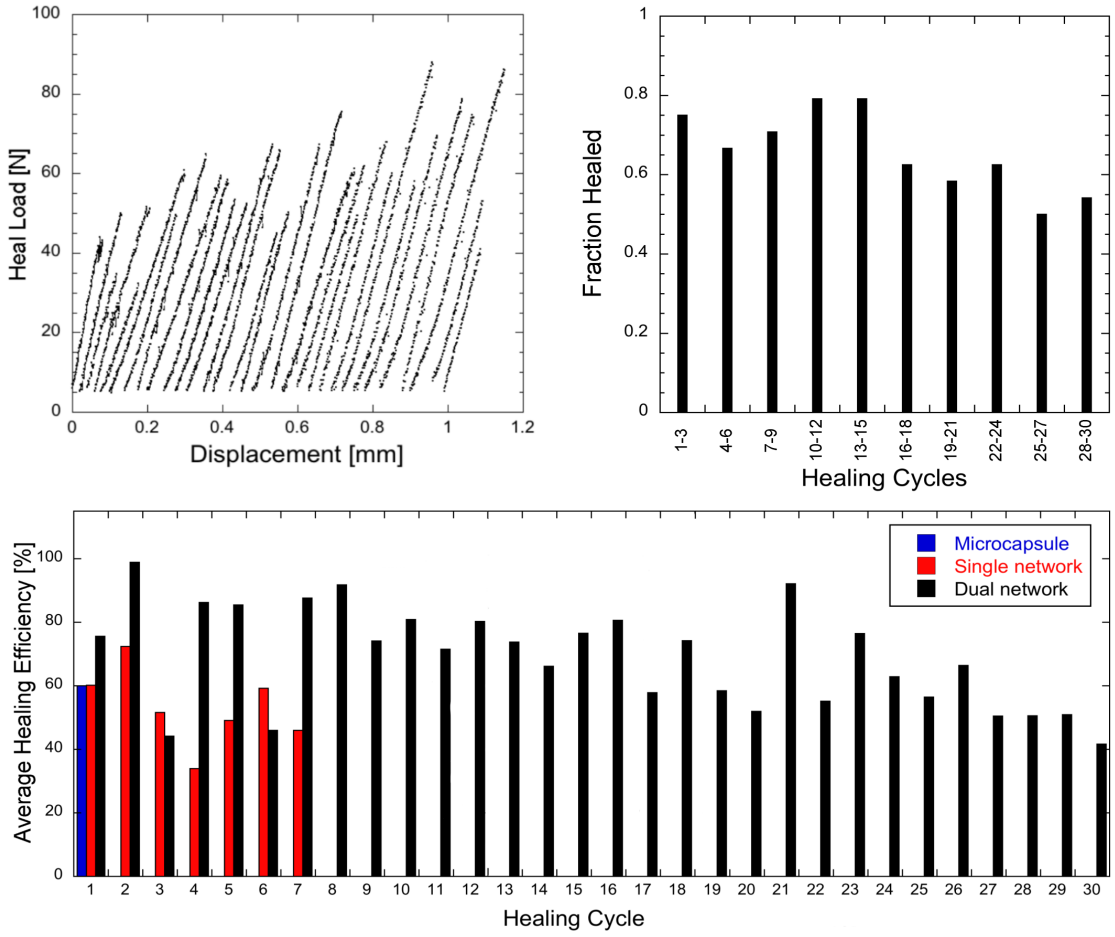

Figure 3.8. (a) Load-displacement curves for one specimen exhibiting over 30 continuous healing cycles, where the first curve denotes the virgin fracture. (b) Fraction of specimens (out of 8 total) demonstrating healing per cycle. (c) Average healing efficiency for these specimens over 30 heal cycles, compared with prior data from microcapsule (blue) [42] and single-network microvascular (red) [14] systems.

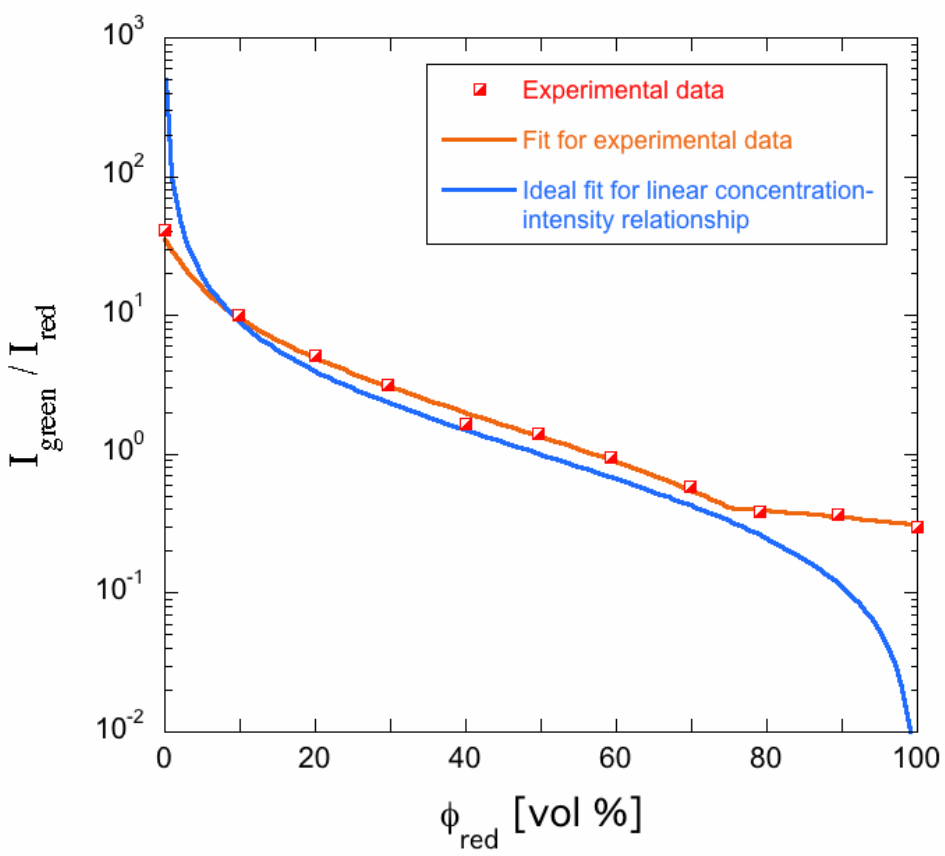

Figure 3.9. Dependence of red and green fluorescence for water-glycerol resin and hardener mimics, respectively. The experimental data matches the fit for a linear relationship between intensity and fluid volume fraction for a range of 10 to 80 vol% resin mimic.

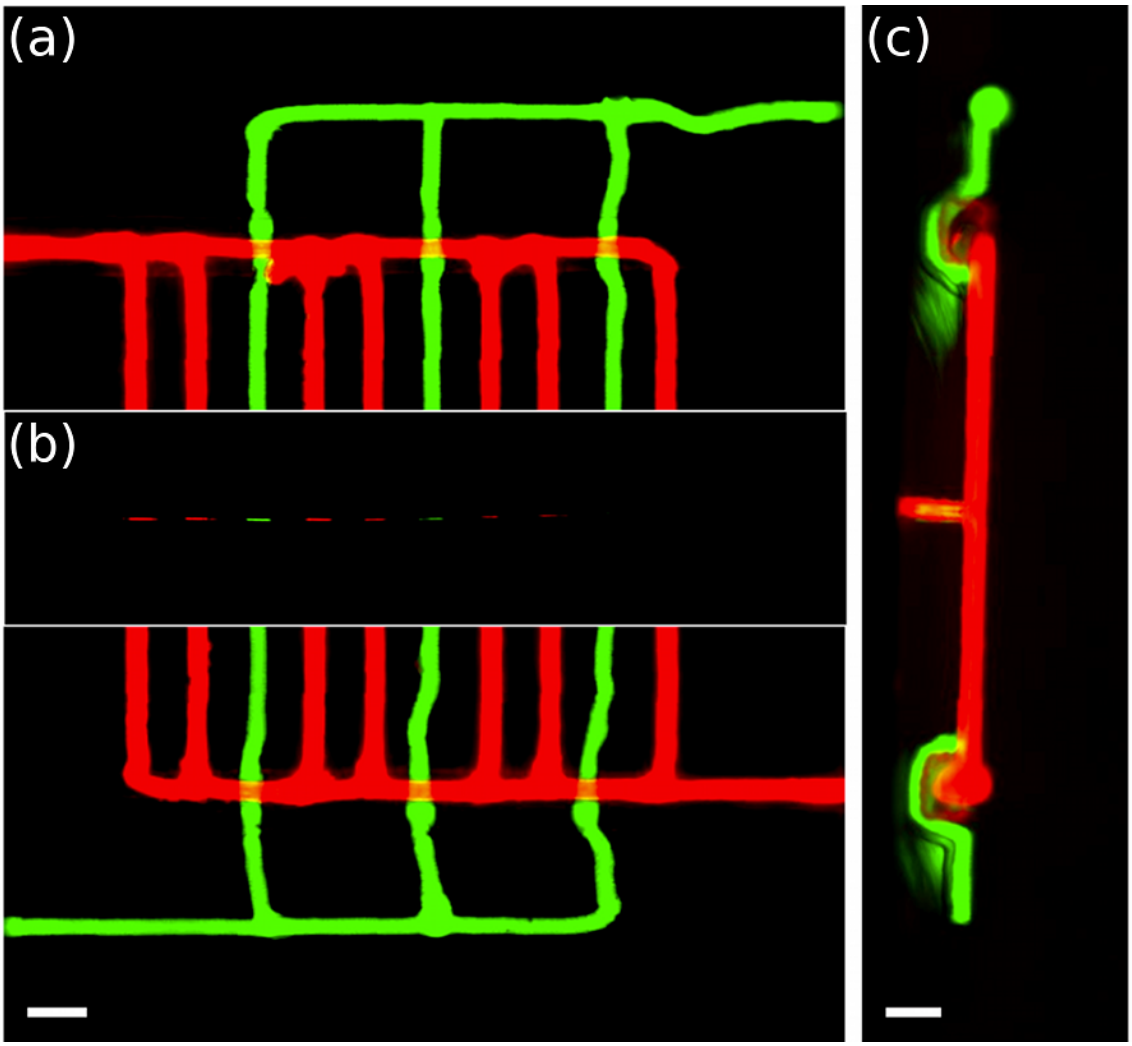

Figure 3.10. Fabricated microvascular network design for fluid transport imaging and analysis. (a) Bottom view of the network infiltrated with resin (red) and hardener (green) mimics (scale bar = 1 mm) (b) Top view of a single crack in the coating superimposed on view (a). (c) Side view of embedded microvascular network.

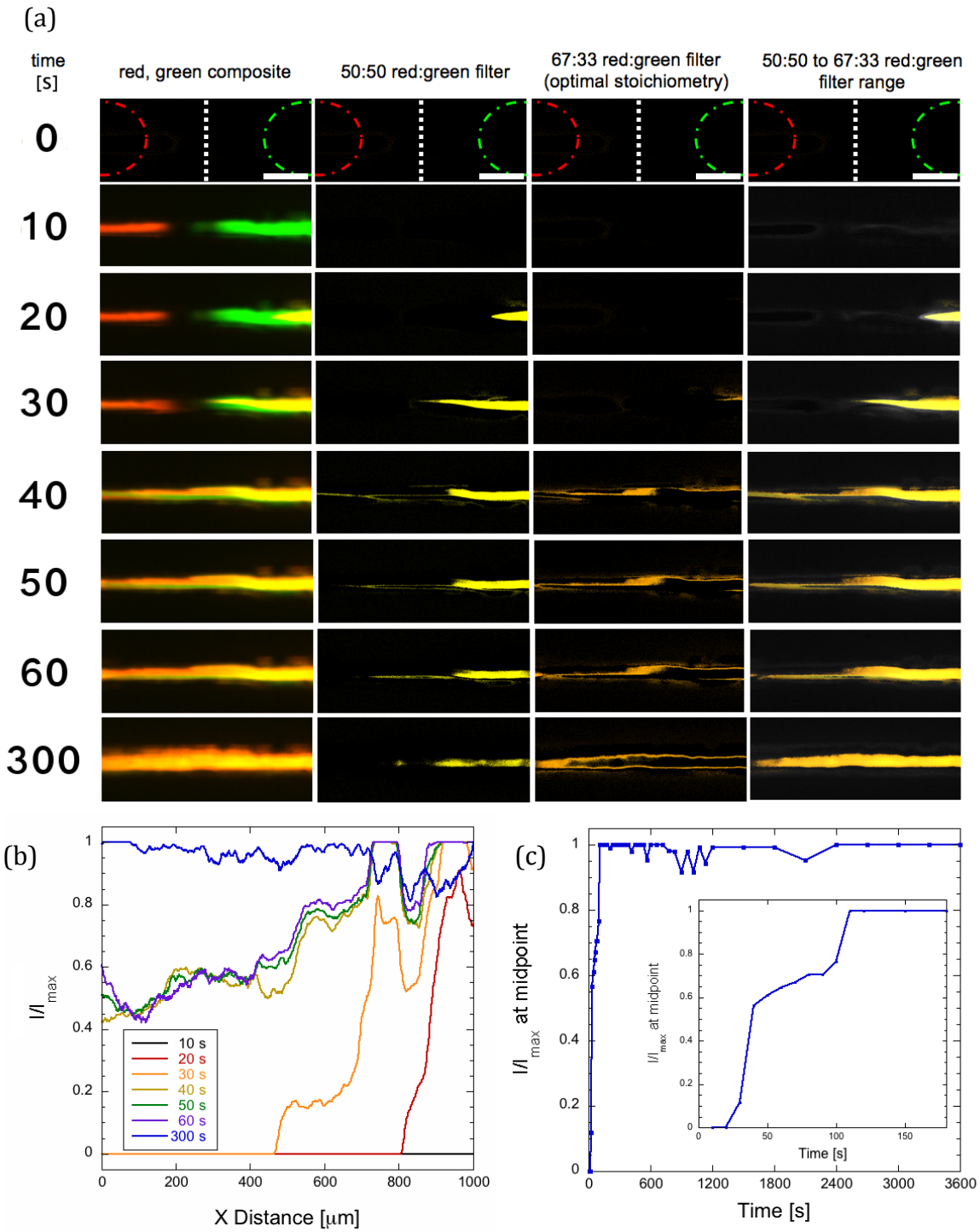

Figure 3.11. (a) Microscope images of mixing in crack plane, where mixing is shown by filtering for 50:50 (yellow) and 67:33 (orange) compositions. The midpoint between vertical features is indicated by the dotted line. Scale bar is 200 μm. (b) Intensity of mixed fluid (I) normalized by (I_{max}) versus distance between underlying vertical features. (c) Fraction of crack width mixed at midpoint versus time. Full mixing is achieved within ~100 s.

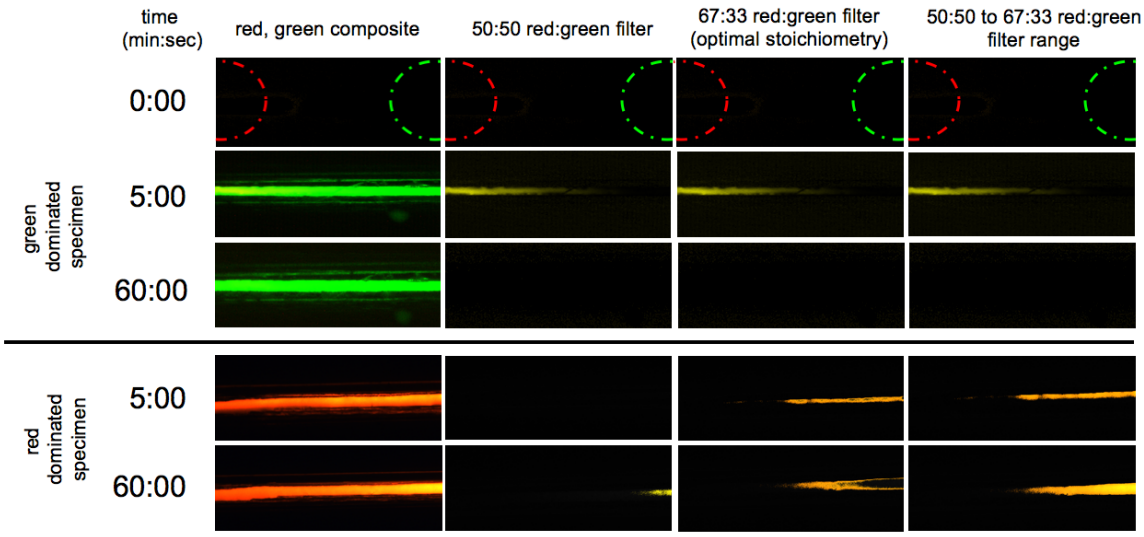

Figure 3.12. Crack plane images of specimens that exhibited poor mixing behavior. The top images indicate the location of fluid conduits that feed red and green water-glycerol solutions to the surface. Center-to-center distance of red and green fluid conduits is 1 mm.

CHAPTER 4

THERMALLY ENHANCED SELF-HEALING VIA TERNARY INTERPENETRATING MICROVASCULAR NETWORKS

4.1 Introduction

Biological systems employ pervasive microvasculature to accomplish a range of critical functions, including tissue regeneration, thermal regulation, and nutrient transport. Biomimicry of these diverse functions in materials systems can be achieved by embedding a pervasive network of interconnected microchannels. Several emerging applications have recently been demonstrated, including self-healing materials,[1, 2] active cooling networks,[3, 4] and tissue cultures.[5] For example, self-healing materials benefit from the introduction of microvascular networks, as they allow both repetitive healing and new healing chemistries to be utilized.[2, 6, 7] By embedding isolated microvascular networks in close proximity to one another, two-part liquid healing systems are sequestered within the substrate and react only after damage induces their release to the crack plane. To date, dual microvascular networks have been integrated in multiple structural geometries, including substrates with brittle coatings,[2, 7] bulk structural polymers,[8] and sandwich composite structures.[9, 10] From the broad range of suitable healing chemistries, epoxy resin and amine hardener systems are typically chosen due to their low cost and wide availability in bulk quantities. However, these systems exhibit slow reaction rates, diffusion, and mixing within the crack plane. Current microvascular healing therefore requires substantial intervals ($\geq$48 hr) to recover a significant fraction of their original mechanical strength.[2, 7, 8, 10]

Acceleration of mechanical recovery requires an increase in the epoxy reaction kinetics to quicken the rebonding of the fracture plane. Reaction kinetics for monomeric and oligomeric epoxides in the presence of amines are characterized by an Arrhenius temperature dependence.[11] As such, small temperature increases can produce significant acceleration of the epoxy cure rate. The ability to thermally accelerate mechanical restoration has been demonstrated in the microcapsule-based healing system[12] through the incorporation and resistive heating of shape-memory alloy wires across the fracture interface. However, this approach is not readily compatible with current microvascular fabrication techniques.

Successful implementation of thermally accelerated healing depends critically upon the integration of a localized heating capability. Many engineered structures that would benefit from accelerated healing are large-scale, including wind turbine blades or aircraft wings, which preclude bulk thermal annealing. Moreover, these structures often contain integrated components, such as microelectronics, that cannot tolerate excessive thermal loads. Hence, targeted, localized heating offers an efficient approach to accelerate healing of the damage region *in situ*, while leaving a majority of the surrounding structure undisturbed.

Here, we report the fabrication and characterization of self-healing materials with embedded ternary interpenetrating microvascular networks in an epoxy coating/substrate architecture. The networks are fabricated by direct-write assembly of two fugitive inks, in which the primary ink defines the three microvascular networks and the secondary ink functions solely as a spacer to isolate each network. Two of the microvascular networks are devoted to supplying the epoxy resin and hardener healing agents, while the third

network circulates a thermally regulated fluid. We first characterize the bulk curing kinetics of this epoxy system over the temperature range of interest. Next, we investigate the effect of thermally accelerated healing on mechanical restoration of these coating/substrate architectures. Finally, we evaluate the extent of healing agent mixing in the crack plane as well as the integrity of network flow using fluorescence microscopy.

4.2 Experimental Methods

4.2.1 Interpenetrating Microvascular Network Fabrication

Microcrystalline wax ink composed of 60 w/w% microcrystalline wax (SP-19, Strahl & Pitsch, Inc.) and 40 w/w% heavy mineral oil (Fischer Scientific) is prepared by stirring the molten components at 100°C for 10 min. The heated solution is poured into 3 mL syringes (EFD, Inc.) and is rapidly quenched in an ice water bath to solidify the ink, after which the syringe is warmed to room temperature. The triblock-copolymer ink is prepared with 30 w/w% triblock copolymer (Pluronic F127, BASF) in deionized water. The copolymer is slowly added to an aqueous solution held at 5°C. Upon full dissolution of the copolymer, the solution is refrigerated for >12 h to remove all air bubbles. The cooled solution is poured into 3 mL syringes and then warmed to ambient temperature.

To properly infiltrate the inner portions of the written structures, the epoxy substrates must contain angled grooves in the surface. The positive of these grooves are deposited with wax filaments (330 μm diameter, 1 mm separation) at a 45° angle on a glass slide covered in mold release (Buehler Inc). The substrate epoxy (Envirotex Lite, Environmental Technologies Inc.) is mixed, poured over the glass slide in a mold, and cured. After curing, the substrate is polished and cleaned via ultrasonication in a 20

w/w% aqueous degreaser solution (VCPI-411, Cortec). Interpenetrating microvascular networks are deposited onto the grooved substrates via a three-axis motion-controlled robotic deposition stage (ABL9000, Aerotech Inc.). The fugitive wax and Pluronic F127 ink syringes are fitted with 200 μm and 100 μm nozzles (EFD Inc.), respectively, and mounted to the stage in air-pressure multiplier dispensers (HP7X, EFD Inc.) for extrusion at rates of 4 to 6 mm s^{-1}. The fugitive ink networks are deposited in an alternating fashion, whereby each subsequent fugitive wax network is patterned onto the previously deposited Pluronic F127 support material. The order of wax network deposition is first the epoxy resin network (330 μm feature diameter), followed by the epoxy curing agent network (330 μm feature diameter), and ending with the thermal fluid circulation network (200 μm feature diameter). The microchannel diameters are varied by dynamically controlling the applied extrusion pressure.[13] A detailed schematic fabrication flowchart is provided in Figure 4.1.

Envirotex Lite epoxy matrix material is prepared for infiltration by mixing 30 min prior to infiltration and degassing under vacuum for 10-15 min. The patterned structures are infiltrated with epoxy via pipetting the material evenly around the structure with a syringe fitted with a 330 μm tip. After the structure is fully covered, the epoxy is cured for 24 hr at room temperature. Access to the Pluronic F127 networks is provided via diamond saw cuts to enable preferential dissolution of this fugitive ink in a water bath held for 12 hr at ~5°C. The specimens are dried and the connected void volume is reinfiltrated with epoxy matrix material. Upon curing, the specimens are cut and polished to final dimensions of 50 mm x 14 mm x 7 mm. The fugitive wax ink is melted

at 85°C for removal from the specimen via application of a light vacuum and any wax residue dissolved via ultrasonication with a 20 w/w% aqueous degreaser solution.

4.2.2 Epoxy Fluid Measurements

The epoxy resin and hardener viscosities are measured using a controlled-stress rheometer (C-VOR, Malvern Instruments, Malvern, UK) equipped with a cup and bob (C14, 14 mm bob diameter, 0.4 mm gap width) geometry at 25°C. Contact angles for the components in contact with the brittle coating material are imaged with a digital camera (PowerShot S2 IS, Canon) and angles are measured with ImageJ (NIH). Surface energies of the liquid-vapor interfaces of the healing components are measured with a tensiometer (250-CA, Ramé-Hart Instrument Co.) and are averaged over 30 sample measurements each.

4.2.3 Differential Scanning Calorimetry (DSC)

Isothermal DSC tests are performed on a DSC (DSC821, Mettler-Toledo) at 30, 50 and 70°C under a nitrogen atmosphere. The epoxy resin and hardener are stoichiometrically mixed in a 2.29:1 ratio of EPON 8132:Epikure 3046 within 60 s of test initiation. The measurement cell is pre-heated to minimize the transient heating time (<30 s for 70°C) to accurately capture initial reaction rates. Tests are ended after 12 hr, when the reaction exotherm falls below the detection limits of the machine.

4.2.4 Rheological Measurements

The shear storage and loss moduli, G' and G'' respectively, of the epoxy system are measured with a controlled-strain rheometer (AR-G2, TA Instruments) using a parallel plate geometry (25 mm diameter). Stoichiometric mixtures of EPON 8132 and Epikure

3046 are placed in the geometry and isothermally held at 30, 50 or 70°C. Oscillatory measurements are performed at 1 Hz with 0.1% strain with a plate gap of ~600-800 μm.

4.2.5 Dynamic Mechanical Analysis (DMA)

The tensile storage and loss moduli, E' and E'' respectively, of polymerizing epoxy material are determined by dynamic mechanical analysis (RSA III, TA Instruments). Stoichiometric EPON 8132 and Epikure 3046 mixtures are cured in an oven at 30, 50 or 70°C until 30 min after the relevant gel point (G'/G'' crossover). The weakly elastic bars (dimensions ~45 mm x 12 mm x 2 mm thick) are placed on the DMA in a 3-point bend geometry with a 25 mm span. The bend specimens are isothermally held at their respective temperatures and probed at 1 Hz at 0.2% strain.

4.2.6 Thermal Imaging

The thermal surface profiles of specimens heated with circulating fluid are imaged with an infrared camera (DeltaTherm 1560, StressPhotonics Inc.). The specimen surface is painted black matte (Ultra-flat black, Krylon) for optimal imaging. A constant-temperature circulating bath (RTE-110, Neslab Instruments) with water is heated to 30, 50 or 70°C and connected to a peristaltic pump (Model 7523-00, Cole-Parmer) set to an average flow rate of 5 mL min^{-1}. Fluid flow is commenced ~15 s following the start of image recording, with thermal profiles imaged at an interval of 1 s for 15 min in order for the sample to reach thermal equilibrium.

4.2.7 Coating Application

The microvascular networks are infiltrated with a low-melting temperature wax (Purester 24, Strahl & Pitsch) to prevent the coating material from infiltrating the microchannels. The coating is composed of EPON 828 (Miller Stephenson Inc.),

diethylenetriamine (Air Products Inc.), and Epikure 3253 (Miller Stephenson Inc.) mixed in a 100:15:7.5 weight ratio with a 0.2 w/w% addition of carbon black (Alfa-Aesar, Inc.) to mask the underlying microvasculature during fluorescence imaging studies. The epoxy coating is applied to the specimen surface and is cured at room temperature for 20 hr. The coating is then polished to a final thickness of 680±30 μm. The fugitive wax is removed by heating the specimen to 40°C and flushing the specimen with petroleum ether (Fisher Scientific) three times, followed by flushing with xylenes (Acros Organics) three times.

4.2.8 Mechanical Fracture Tests

The two healing networks are filled with either epoxy resin (EPON 8132, Miller-Stephenson) or epoxy curing agent (Epikure 3046, Miller-Stephenson) that are fluorescently labeled with a rhodamine-based (DFSB-K87, Risk Reactor) or fluorescein-based dye (DFSB-K43, Risk Reactor), respectively. The coating is notched directly above vertical channel features using a test panel scratcher (Corrocutter 639, Erichsen) with a razor blade scribe under a constant load (6-10 N). The specimen is loaded in four-point bending and load-displacement data are recorded using LabVIEW (v.8.6, National Instruments) [6]. Crack events are detected by an acoustic-emission sensor (model SE2MEG-P, Dunegan Engineering Company) and data collected with a digital oscilloscope (model LC584A, LeCroy). Load-displacement data are correlated with the acoustic emission data to determine the peak load at fracture. The specimen undergoes 50 flexural cycles at 50 μm s^{-1} with an amplitude of 50 μm. Specimens are subsequently attached via tubing to a constant-temperature circulating bath (RTE-110, Neslab Instruments) and centrifugal pump (67705K36, McMaster-Carr) to circulate fluid at

temperatures of 30, 50 or 70°C. Specimens are returned to room temperature prior to testing of the healed coating. 8 specimens are averaged per final data point at each temperature and 5 specimens each for all other data points.

4.2.9 Fluorescence Imaging and Analysis

Directly following heating and prior to heal mechanical testing, specimens are fluorescently imaged on an inverted microscope (DMI 6000B, Leica Microsystems) with a mercury-lamp source set to 50% its maximum UV intensity. Images are captured over the length of the crack plane using red (λ= 595 nm) and green (λ= 520 nm) filters under a 5X objective. Images are natively captured in 12-bit grayscale. The exposure time is the same for all photos within a set of red and green images, with typical exposure times of 100 to 150 ms. Exposure times were chosen so as to use a large fraction of the dynamic range of the camera while avoiding image saturation. The microscope was set to 35% UV exposure for red images and 10% UV exposure for green images.

Using MATLAB (v.2009b, MathWorks, Inc.), the grayscale images recorded with red and green filters are merged into color images and scaled by a factor of 16 to be saved as 16-bit images (saving to a 12-bit TIFF format is not supported by MATLAB) (Fig. 4.2a). The color channels are resampled according to a composition calibration curve so that the resultant photo pixel colors linearly correspond to their composition (Fig. 4.2b). This calibration curve, shown in Figure 4.3, was experimentally constructed by imaging dyed epoxy resin and curing agent mixtures in 10% composition increments. The data is fit in MATLAB to produce equation 4.1:

$$\phi_{hardener} = 6\times10^{-5}\left(\frac{I_{red}}{I_{green}}\right)^3 - 4.5\times10^{-3}\left(\frac{I_{red}}{I_{green}}\right)^2 + 0.1131\left(\frac{I_{red}}{I_{green}}\right) \qquad (4.1)$$

where I_{red} is the red pixel intensity and I_{green} is the green pixel intensity. The composition fraction of red and green are scaled to the full available intensity range (Fig. 4.2c).

Composition distribution analysis is restricted to crack plane regions by (1) choosing a threshold level in MATLAB so the resulting image crack width matches the crack width observed transmission light microscopy (Fig. 4.2c) and (2) removing any extraneous, non-crack plane intensity data by using regions of interest in ImageJ (NIH). These non-crack plane fluorescence regions are caused by residual epoxy after using a KimWipe to remove epoxy that overflowed the crack plane during the 50 flexural cycles. The composition distribution curves are computed with MATLAB (MathWorks, Inc.) by dividing pixel (1.5 μm x 1.5 μm) composition data into 100 bins of width equal to 1% change in composition, and then dividing each bin by the total number of pixels to produce composition fractions.

To determine full occlusion of vertical conduits, the coating material is removed via a polish wheel to expose the conduit openings. All non-polymerized material is removed via solvent flushing with either petroleum ether for the hardener network or with xylenes for the resin network. Specimens are reimaged in the crack region and the photos are manually examined for fluorescent polymerized material partially or fully covering channel openings. Channels exhibiting full occlusion were recorded as containing polymerized material within the entirety of the circular exit (area fraction occluded $\phi_{occluded} = 1$), while $\phi_{occluded}$ for channels exhibiting partial occlusion was estimated by equation 4.2:

$$\phi_{occluded} = 1 - \left(\frac{r_{open}}{r_{conduit}} \right)^2 \tag{4.2}$$

where $r_{occluded}$ is the non-occluded radius and $r_{conduit}$ is the radius of the vertical conduit.

4.3 Results and Discussion

4.3.1 Thermal Curing of Two-Part Epoxy Healing Chemistry

We investigate the curing kinetics of an epoxy system that has been previously utilized in microvascular-based, self-healing systems.[7] This system is composed of a 2.29:1 ratio of diglycidyl ether of bisphenol-A resin (EPON 8132) and an aliphatic amidoamine (Epikure 3046), both of which are commercially formulated with diluents to reduce their viscosity. To determine the effect of temperature on the healing reaction kinetics, studies are carried out at 30, 50, and 70°C. Temperatures above 70°C are not explored to avoid a substantial weakening of the substrate material (see Fig. 4.4).

The initial conversion of liquid monomer to polymer is probed using differential scanning calorimetry under isothermal conditions. The conversion fraction of reactive groups, α, is obtained via measuring the cumulative heat evolved as a fraction of the heat of full reaction (490.5 J g^{-1} with 10°C min^{-1} ramp). The empirical data show the initial conversion rate, $d\alpha/dt = 7.1\times10^{-6}\ \ s^{-1}$, at 70°C is two orders of magnitude greater than at 30°C, such that nearly three times the monomer (74%) is reacted at 70°C relative to 30°C (27%) after 6 hr (see Fig. 4.5). Epoxy-amine reaction kinetics are often successfully described by the Kamal model,[11, 14, 15] which is an autocatalytic phenomenological model given by:

$$\frac{d\alpha}{dt} = \left(k_1 + k_2\alpha^m\right)(1-\alpha)^n \tag{4.3}$$

where k_1 and k_2 are rate constants with Arrhenius temperature dependencies, and m and n are temperature-independent constants. The parameters, provided in Table 4.1, are iteratively solved.[16] Activation parameters are determined from the slope of the rate constants versus inverse temperature (Fig. 4.6). By averaging the rate constants and

exponents with the activation energy parameters,[16] the Kamal model is generalized as a function of temperature by:

$$\frac{d\alpha}{dt} = \left(k_{0,1} \exp\left(\frac{-E_1}{RT} \right) + k_{0,2} \exp\left(\frac{-E_2}{RT} \right) \alpha^{3.46} \right) \left(1 - \alpha^{0.25} \right)$$

where $k_{0,1} = 4.36 \times 10^9$ s^{-1}, $k_{0,2} = 2.17 \times 10^6$ s^{-1}, $E_1 = 97.5$ kJ mol^{-1}, $E_2 = 63.0$ kJ mol^{-1}, R is the universal gas constant, and T is the temperature.

At intermediate times, we determine the effects of accelerated healing kinetics on epoxy gelation under isothermal conditions (Fig. 4.7a). The gel point defines the transition from a predominately viscous liquid to a spanning gel network, as denoted by the crossover in shear storage (G') and loss (G'') moduli. At 30°C, the epoxy gel point occurs at approximately 21 hr, after which polymerized material spans the width of the crack plane. By contrast, the gel point occurs at 3.1 hr and 0.9 hr for 50 and 70°C, respectively. The twenty-fold reduction in the onset of gelation at 70°C greatly shortens the residence time of the fully liquid regime within the crack plane. As a result, self-healing specimens would spend less time in a compromised mechanical state, during which any additional loading may exacerbate the damage incurred.

To probe the final stage of the healing kinetics after gelation, flexure bars of the weakly elastic material are measured by dynamic mechanical analysis (DMA). At their respective temperatures, each bar is probed in a 3-point bend geometry starting approximately 0.5 hr after the onset of gel formation. For fully cured epoxy material, the complex modulus, E^*, is 1.06 GPa at 30°C and drops by a factor of 4.5 at 50°C and a factor of 49.0 at 70°C (Fig. 4.8). To easily compare the complex moduli at elevated temperatures during polymerization, the 50°C and 70°C data are scaled by 4.5 and 49.0, respectively, to yield an effective E^* at 30°C (Fig. 4.7b). At each temperature, the E^*

plateaus near 10^9 Pa, but the time required to reach this stiffness is dramatically shortened from greater than 48 hr at 30°C to ~8 hr at 70°C. From the perspective of repetitive healing, a specimen healed at 70°C will complete at least seven cycles in the same time required to heal a specimen at 30°C.

4.3.2 Direct-Write Assembly of Ternary Interpenetrating Microvascular Networks

To create self-healing materials capable of *in situ* thermal regulation, we designed an epoxy coating/substrate architecture with three interpenetrating microvascular networks (Fig. 4.9a). Similar to the first self-healing system with dual interpenetrating microvascular networks,[2] two of these discrete networks are filled with an epoxy resin and amine hardener, respectively. In each case, vertical conduits are patterned that facilitate the transport of these healing agents from the underlying microvasculature to the brittle coating. The third microvascular network is designed to interdigitate between the vertical features, such that its circulation pathway is spatially located near the damage region within the coating. Each network has a single input and output connected to a macroscale reservoir that supplies the healing or thermal fluids.

These novel self-healing architectures are fabricated by direct-write assembly[17, 18] of microcrystalline wax-based and aqueous Pluronic F127 fugitive inks, whose rheological behavior has been reported previously.[2] The desired microvascular networks are patterned by depositing wax ink filaments that are separated by the deposition of the Pluronic F127 ink. Using this dual ink printing approach, an arbitrary number of isolated microvascular networks can be constructed. The microvascular networks that house the epoxy resin and hardener are composed of microchannels of 330 μm in diameter, while the network that circulates fluid for thermal control consists of

microchannels that are 200 μm in diameter to facilitate their interdigitation between the printed vertical features. After the patterning is complete, the printed structure is first infiltrated with the substrate resin and cured and the inks are sequentially removed. The Pluronic F127 ink is removed first and the resulting microchannels are infiltrated with substrate resin and cured. For aid in visualization, the three microvascular networks are infiltrated with dyed fluids to demonstrate their isolated nature (Fig. 4.9b). Finally, a brittle polymer coating, which is made opaque by the addition of carbon black, is applied to the specimen substrate. The coating opacity is designed to block background fluorescence from the underlying network during imaging of the healing fluids in the crack plane.

4.3.3 Thermal Regulation via Embedded Microvasculature

To demonstrate that this novel microvascular design provides sufficient thermal control in localized regions of damage, an epoxy/coating substrate architecture with an embedded ternary interpenetrating microvascular network is connected to a water circulation reservoir maintained at constant temperature ranging from 30-70°C. The heated water is circulated within the third interdigitated network at a flow rate of 5 mL min^{-1}.[4] The specimen is imaged with an infrared camera as a function of time to determine its surface temperature. Thermal images are acquired continuously at each temperature of interest. The samples achieve thermal equilibrium in 5 min or less for each temperature explored, with values approximately 3 to 5°C lower than the water reservoir. Sample images obtained after 10 min are shown in Figure 4.10a-c, in which the location of the fluid microchannels are highlighted by the dashed white lines in Figure 4.10a. Water is used as the thermal fluid due to its high conductivity and heat capacity.

However, this fluid may introduce small bubbles into the microvascular channels that divert flow and lead to minor variations in the temperature profiles. To obviate this, an alternative fluid, such as polyalphaolefin oil, could be used.[4]

4.3.4 Self-Healing of Ternary Interpenetrating Network Systems

To demonstrate the self-healing behavior of these epoxy coating/substrate architectures with ternary interpenetrating microvascular networks, we tested them under 4-point bending using the test protocol reported previously.[6] The brittle coating is fractured at room temperature in a single location and fluorescently dyed epoxy resin and hardener wick into the crack plane. After healing for specified times while continuously circulating the heated fluid (Fig. 4.11), samples are cooled to room temperature and mechanically tested to assess their healing efficiency. A heal stress (σ) based on the healed peak load (P_{peak}) at fracture is calculated using equation 4.5:

$$\sigma = \frac{3P_{peak}(L - L_i)}{2wt^2} \tag{4.5}$$

where L is the support span (40 mm), L_i is the inner loading span (20 mm), w is the specimen width, and t is the specimen thickness. The average heal stress values are plotted as a function of time for the three temperature conditions explored (see Fig. 4.12).

In these samples, healing is not observed prior to the onset of epoxy gelation. At 30°C, t_{gel} ≈21 hr and intermittent healing is observed after 24 hr to 36 hr. These samples required heal times of at least 42 hr to achieve consistent mechanical restoration. By contrast, t_{gel} ≈ 3.1 and 0.9 hr at 50 and 70°C, respectively. At 50°C, samples exhibit consistent healing after approximately 4 hr, whereas only 1 hr is required for samples held at 70°C. Moreover, in each case, their average heal stress increases with time, because the epoxy curing reaction continues well beyond the gel point. To obtain the

same degree of mechanical restoration, defined as σ = 2.03 MPa to match the average original fracture stress, total healing times of 40, 4, and 1.5 hr are required for samples held at 30, 50 and 70°C, respectively. In addition to increased reliability at elevated temperatures, the concomitant decrease in healing times by an order of magnitude greatly accelerates mechanical recovery thereby reducing the downtime for damaged structures.

To investigate the epoxy resin and hardener mixing in the crack plane upon fracture, the samples are imaged using fluorescence microscopy to determine the location of the dyed epoxy components. A representative image of the fracture region is shown in Figure 4.13a, where green and red fluorescence indicate the presence of epoxy resin and hardener, respectively. Clearly, a substantial fraction of the fluid is in either highly resin- or hardener-rich regions (Fig. 4.13b). The average composition within the crack plane is 70% epoxy resin and 30% hardener, closely matching the 2-to-1 ratio of vertical conduits that deliver these healing agents to the crack plane. The composition distributions for comparable healing strengths are displayed in Figure 4.13c for healing times of 48, 8 and 4 hr at 30, 50 and 70°C, respectively. The distribution curves have strong peaks near both the pure hardener and pure resin compositions, which are irrespective of time or temperature (Figure 4.14). Two-part epoxy healing strongly depends upon the epoxy stoichiometry and mixing within the damaged region. Substantial polymerization only occurs for fully mixed compositions composed of 40-75 w/w% resin. As seen in Figure 4.13b-c, only ~20-30% of the crack plane volume contains compositions within this desired range. Prior self-healing studies based on single[6] and dual[7] microvascular network architectures have revealed similar incomplete curing, with only ~50% of the crack plane covered with polymerized epoxy material after multiple healing cycles.[7]

Note, in poorly mixed fluid regions, a weak gel with minimal elasticity likely forms, which is unable to contribute significantly to the overall recovery of mechanical strength.

To compare these observations to the predicted behavior, we estimate the characteristic timescales associated with epoxy flow within the crack plane, t_{flow}, diffusion, $t_{diffusion}$, and curing kinetics upon fracture, t_{cure}, as discussed in Chapter 3.3.6. Immediately upon crack formation within the brittle coating, capillary forces induce fluid migration from the vertical conduits (330 μm in diameter) to the crack plane (width ≈ 50–100 μm). The pressure drop (ΔP) that drives fluid flow is given by equation 4.6:

$$\Delta P = 2\gamma\cos\theta\left(\frac{1}{D_1}+\frac{1}{D_2}\right)-2\gamma\cos\theta\left(\frac{1}{R}\right) \tag{4.6}$$

where γ is the liquid-vapor surface energy, θ is the contact angle, D_1 and D_2 are the principal diameters of curvature for the crack opening, and R is the radius of the network channels.[19] The capillary driving force is opposed by a viscous resistance to fluid flow, as described by the Hagen-Poiseuille relationship for cylindrical channels:

$$\Delta P = \frac{32\mu LU}{D^2} \tag{4.7}$$

where μ is the dynamic viscosity, L is the fluid path length within the microvascular network, and U is the linear velocity of the fluid within the network. The minimum fluid velocity within the crack plane, U_{crack}, is determined for the longest path length, L, of ~28 mm for both the epoxy resin (γ=35.3 mN m^{-1}, θ=9°, μ=1.07 Pa-s) and hardener (γ=32.8 mN m^{-1}, θ=20°, μ=0.44 Pa-s) by equating Eqs. (4.6) and (4.7), and assuming conservation of fluid volume. For typical crack widths ranging from ~50 to 100 μm, t_{flow} ranges, respectively, from 3.3 to 18.5 s for the resin and from 1.5 to 8.2 s for the hardener at

room temperature. The predicted times are in good agreement with direct imaging of fluid flow, in which cracks fully filled within ~15 s.

The second timescale, $t_{diffusion}$, defines the time for a given fluid to diffuse across the characteristic length scale, i.e., half the center-to-center distance between vertical conduits (500 μm). The Einstein-Smoluchowski equation for molecular diffusion is given by:

$$t_{diffusion} = \frac{\langle x^2 \rangle}{2D} \tag{4.8}$$

where $\langle x^2 \rangle$ is the root-mean square net displacement of the molecule. From Eq. 4.8, we estimate $t_{diffusion} \approx 6.5$ hr for an initial D of 5.2×10^{8} cm^2/s,[20] which is substantially longer than t_{flow}, but lower than t_{cure} (using the gelation time as a proxy). However, it is well known that the diffusivity decreases by a few orders of magnitude as the initial reaction proceeds to t_{cure},[21] which results in $t_{diffusion} >> t_{cure}$. As shown in Figure 4.14, the extent of mixing does not depend strongly on t_{cure} because diffusion is greatly hindered within the crosslinked epoxy network. The true value for $t_{diffusion}$ is therefore much greater than t_{cure}. Mixing is also relatively independent of temperature increases, though the resin-rick peak broadens and shifts slightly to lower resin-to-hardener ratios (Figure 4.13c). Hence, the exponential increase in diffusivity with temperature is largely counterbalanced by an analogous increase in epoxy viscosity. Nevertheless, our observations reveal a slight difference between these two activation energies that weakly favors diffusive mixing at higher temperatures, and thus, further enhances healing.

To retain the repeated self-healing benefits of microvasculature, minimal obstruction of the channels to further fluid flow is required. To ascertain the extent of blocked vertical conduits, the specimen brittle coating is removed and all non-polymerized material removed by flushing with solvents miscible with the epoxy components. When

imaged with fluorescence microscopy, any polymerized material remaining in the access channels fluoresces and indicates obstructed pathways. Channels display a variety of obstruction patterns, including one-sided peripheral, circumferential, and complete polymerization (Fig. 4.15a-b). As seen in Figure 4.15c, the prevalence of fully obstructed channels increases with time, as well as with temperature, due to the ongoing polymerization reaction. Fewer than 20% of channels are obstructed at 48 hours in the 30°C case, while nearly 20% of channels are obstructed at the shortest healing time (0.5 hr) at 70°C. The resin channels show a slightly greater propensity to full channel blockage than do the curing agent channels, possibly due to the decreased fluid fraction that must be reach the resin conduits (0.305 curing agent fraction transported) as compared to curing agent conduits (0.695 resin fraction transported) in order to achieve a stoichiometric gel. Note that the addition of partially occluded channels to does not significantly change the results (Fig. 4.15d). The observation of obstructed channels indicates 50°C may be an optimal temperature for rapid self-healing while retaining obstruction rates comparable to those of the 30°C case.

At 70°C for the longest healing times tested (i.e., 4 and 6 hr), propagation of the surface crack into the substrate material is occasionally observed (Fig. 4.16). If the crack propagates to a depth sufficient to intersect the water circulation network, the integrity of the network is compromised and further fluid circulation will leak through the crack. Hence, for testing at elevated temperatures, it is necessary to monitor for sudden loss of . Biological systems employ thrombosis to prevent catastrophic loss of microvascular fluids.[22] Likewise, in several specimens that experienced compromised networks at a

time near to the gel point, the epoxy continued its polymerization and effectively stopped a majority of the fluid loss.

4.4 Conclusions

We have constructed self-healing materials with ternary interpenetrating microvascular networks by direct-write assembly of fugitive inks. Thermal characterization of the bulk two-part epoxy healing system revealed healing kinetics are accelerated by over an order of magnitude as the temperature increases from 30 to 70°C. Localized heating in the damage regions is enabled by a temperature-controlled fluid through the embedded microvasculature. Their mechanical behavior shows that the healing times are reduced by over an order of magnitude with increased dependability of restoration at elevated temperatures. This flexible design may find widespread use in large-scale structural applications that would benefit from accelerated autonomic healing via localized, *in situ* thermal regulation.

4.5 References

1. S. R. White, N. R. Sottos, P. H. Geubelle, J. S. Moore, M. R. Kessler, S. R. Sriram, E. N. Brown, and S. Viswanathan, *Autonomic healing of polymer composites*. Nature, 2001, 409, p. 794-797.
2. C. J. Hansen, W. Wu, K. S. Toohey, N. R. Sottos, S. R. White, and J. A. Lewis, *Self-healing Materials with Interpenetrating Microvascular Networks*. Advanced Materials, 2009, 21, p. 4143-4147.
3. R. B. Oueslati, D. Therriault, and S. Martel, *PCB-integrated heat exchanger for cooling electronics using microchannels fabricated with the direct-write method*. IEEE Transactions on components and packaging technologies, 2008, 31, p. 869-874.
4. B. D. Kozola, L. A. Shipton, V. K. Natrajan, K. T. Christensen, and S. R. White, *Characterization of Active Cooling and Flow Distribution in Microvascular Polymers*. Journal of Intelligent Material Systems and Structures, 2010, 21, p. 1147-1156.

5. N. W. Choi, M. Cabodi, B. Held, J. P. Gleghorn, L. J. Bonassar, and A. D. Stroock, *Microfluidic scaffolds for tissue engineering*. Nature Materials, 2007, 6, p. 908-915.
6. K. S. Toohey, N. R. Sottos, J. A. Lewis, J. S. Moore, and S. R. White, *Self-healing materials with microvascular networks*. Nature Materials, 2007, 6, p. 581-585.
7. K. S. Toohey, C. J. Hansen, J. A. Lewis, S. R. White, and N. R. Sottos, *Delivery of two-part self-healing chemistry via microvascular networks*. Advanced Functional Materials, 2009, 19, p. 1399-1405.
8. A. R. Hamilton, N. R. Sottos, and S. R. White, *Self-Healing of Internal Damage in Synthetic Vascular Materials*. Advanced Materials, 2010, 22, p. 5159-5163.
9. H. R. Williams, R. S. Trask, and I. P. Bond, *Self-Healing Composite Sandwich Structures*. Smart Materials and Structures, 2007, 16, p. 1198-1207.
10. H. R. Williams, R. S. Trask, and I. P. Bond, *Self-Healing Sandwich Panels: Restoration of Compressive Strength After Impact*. Composites Science and Technology, 2008, 68, p. 3171-3177.
11. A. Yousefi, P. G. Lafleur, and R. Gauvin, *Kinetic Studies of Thermoset Cure Reactions: A Review*. Polymer Composites, 1997, 18, p. 157-168.
12. E. L. Kirkby, J. D. Rule, V. J. Michaud, N. R. Sottos, S. R. White, and J.-A. E. Månson, *Embedded shape-memory alloy wires for improved performance of self-healing polymers*. Advanced Functional Materials, 2008, 18, p. 2253-2260.
13. W. Wu, C. J. Hansen, A. M. Aragón, P. H. Geubelle, S. R. White, and J. A. Lewis, *Direct-write assembly of biomimetic microvascular networks for efficient fluid transport*. Soft Matter, 2010, 6, p. 739-742.
14. M. R. Kamal and S. Sourour, *Kinetics and Thermal Characterization of Thermoset Cure*. Polymer Engineering & Science, 1973, 13, p. 59-64.
15. M. R. Kamal, *Thermoset Characterization for Moldability Analysis*. Polymer Engineering & Science, 1974, 14, p. 231-239.
16. J. M. Kenny, *Determination of Autocatalytic Kinetic Model Parameters Describing Thermoset Cure*. Journal of Applied Polymer Science, 1994, 51, p. 761-764.
17. D. Therriault, S. R. White, and J. A. Lewis, *Chaotic mixing in three-dimensional microvascular networks fabricated by direct-write assembly*. Nature Materials, 2003, 2, p. 265-272.
18. D. Therriault, R. F. Shepherd, S. R. White, and J. A. Lewis, *Fugitive inks for direct-write assembly of three-dimensional microvascular networks*. Advanced Materials, 2005, 17, p. 395-399.
19. E. Delamarche, A. Bernard, H. Schmid, A. Bietsch, B. Michel, and H. Biebuyck, *Microfluidic networks for chemical patterning of substrates: design and application to bioassays*. Journal of the American Chemical Society, 1998, 120, p. 500-508.
20. D. W. Larsen and J. H. Strange, *Pulsed NMR Study of Molecular Motion in the Uncured Diglycidyl Ether of Bisphenol-A*. Journal of Polymer Science, 1973, 11, p. 65-74.
21. Y. Deng and G. C. Martin, *Diffusion and Diffusion-Controlled Kinetics during Epoxy-Amine Cure*. Macromolecules, 1994, 27, p. 5147-5153.

22. H. R. Williams, R. S. Trask, A. C. Knights, E. R. Williams, and I. P. Bond, *Biomimetic Reliability Strategies for Self-Healing Vascular Networks in Engineering Materials*. Journal of the Royal Society Interface, 2008, 5, p. 735-747.

4.6 Tables

Table 4.1. Empirically derived parameters for the Kamal model (see Equation 4.2)

Temperature [°C]	k_1 [s^{-1}]	k_2 [s^{-1}]	m	n
30	7.70×10^{-8}	2.95×10^{-5}	3.20	0.1704
50	5.57×10^{-7}	1.46×10^{-4}	3.79	0.264
70	7.14×10^{-6}	5.44×10^{-4}	3.40	0.3089

4.7 Figures

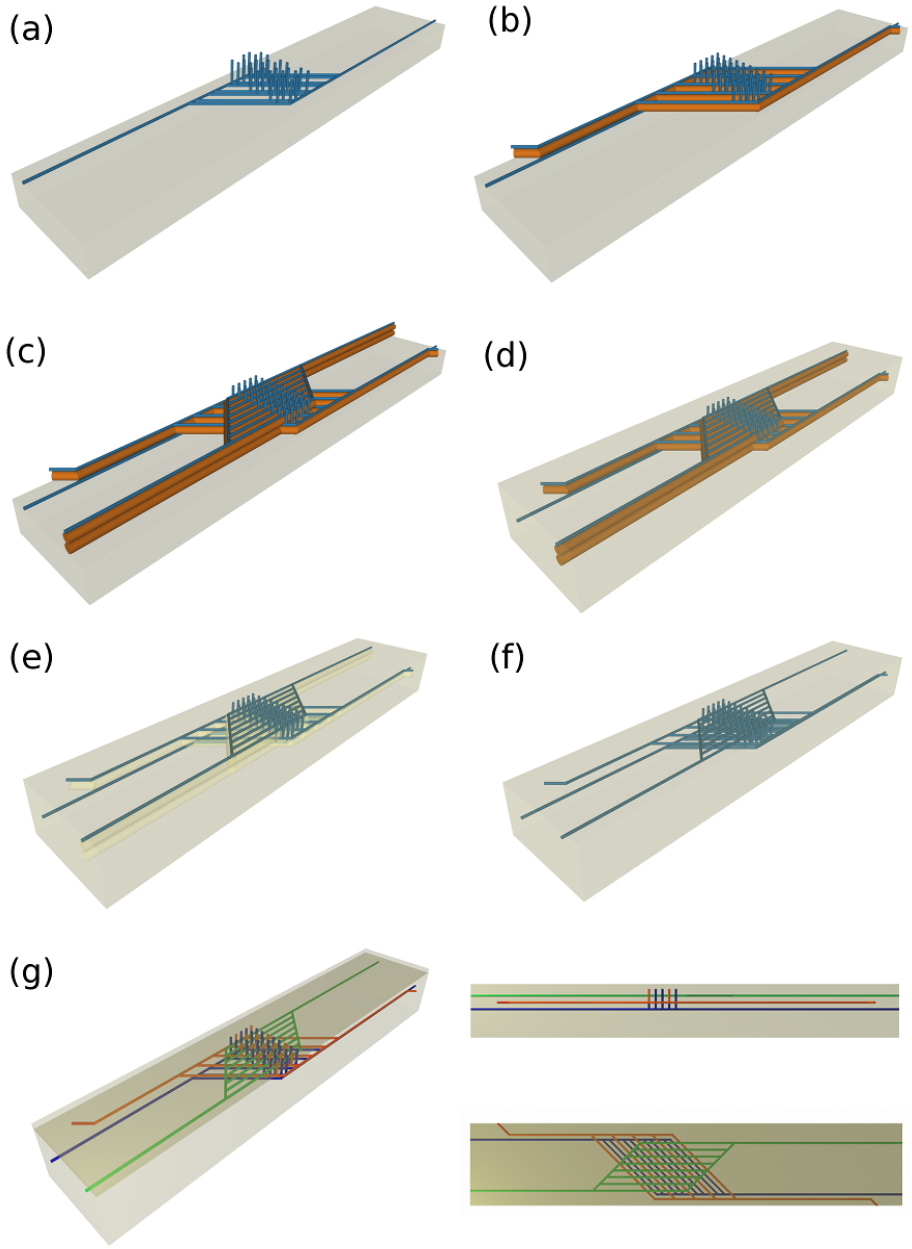

Figure 4.1. Schematic view of the printing process for patterning the three embedded interpenetrating microvascular networks. (a) Wax ink (blue) is deposited to form the resin microvascular network. (b) Pluronic F127 ink (orange) is deposited to provide support for the wax ink deposited for the hardener microvascular network. (c) Pluronic F127 ink is deposited to support the wax ink network that forms the circulating fluid network. (d) The networks are infiltrated with the substrate epoxy resin, which is then cured. (e) After curing, printed Pluronic F127 ink is preferentially removed leaving behind voids that are (f) filled with the substrate epoxy resin and then cured. (g) Wax ink is removed from the structure yielding three networks, which are filled with epoxy resin (blue), hardener (orange), and circulating fluid (green), respectively.

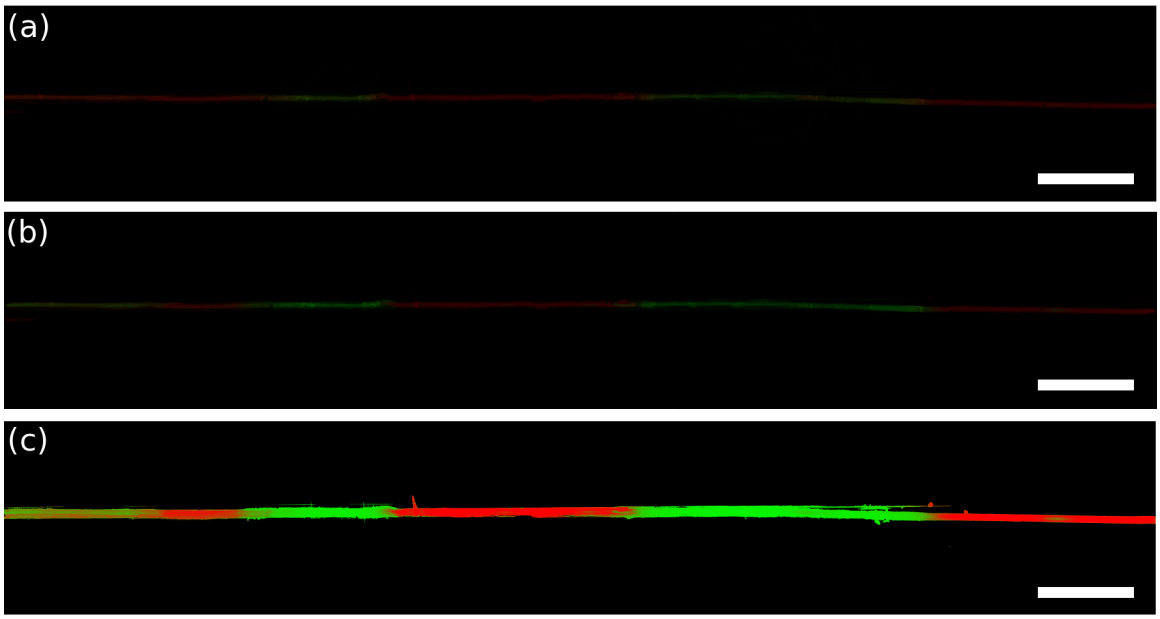

Figure 4.2. (a) Composite image created by tiling the grayscale images recorded with red and green filters as the red and green color channels, respectively. (b) Color channels are resampled according to Eq. S2 to produce photo pixel colors that linearly correspond to their composition. (c) Image is thresholded so that the resulting image crack width matches the crack width observed transmission light microscopy, composition data is scaled to use the full intensity range, and extraneous intensity data outside of the crack region are removed.

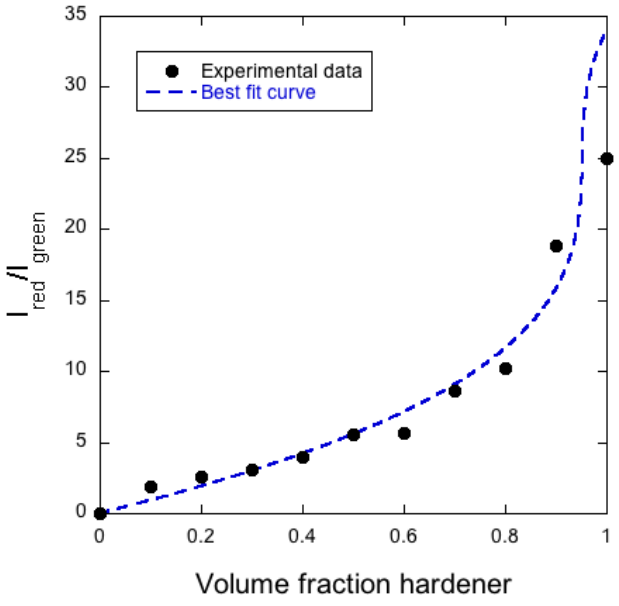

Figure 4.3. Calibration curve relating the red-green intensity ratio to the volume fraction of hardener present in dyed epoxy mixtures.

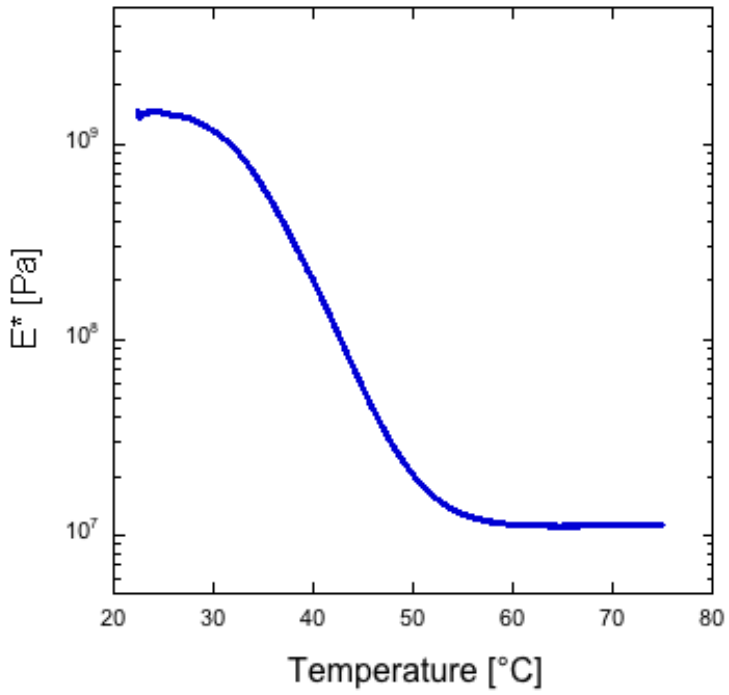

Figure 4.4. Complex modulus E^* for substrate material Envirotex Lite determined by dynamic mechanical analysis. The specimen bar is placed in 3-point bending and heated at a rate of 0.2°C min^{-1}.

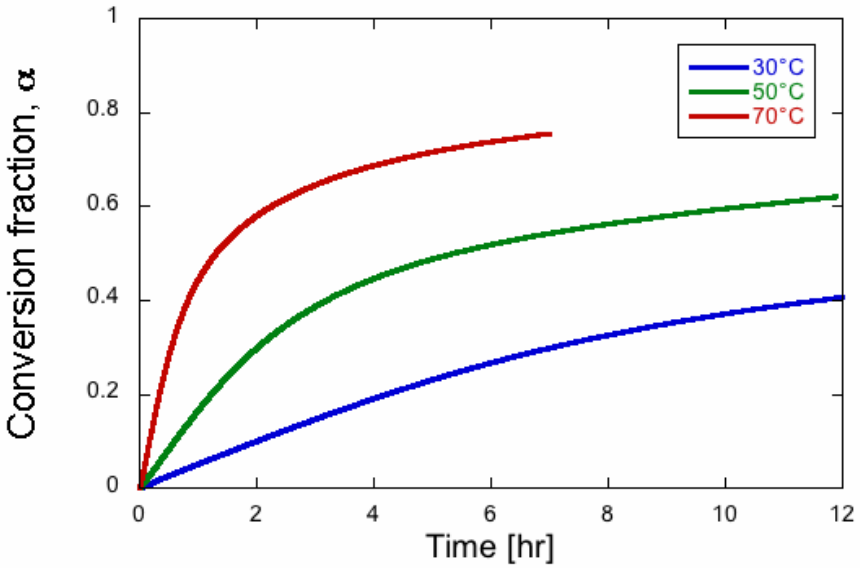

Figure 4.5. Initial epoxy curing reaction as a function of temperature. Data for degree of conversion, α, is collected under isothermal conditions for stoichiometric mixtures of epoxy resin and hardener.

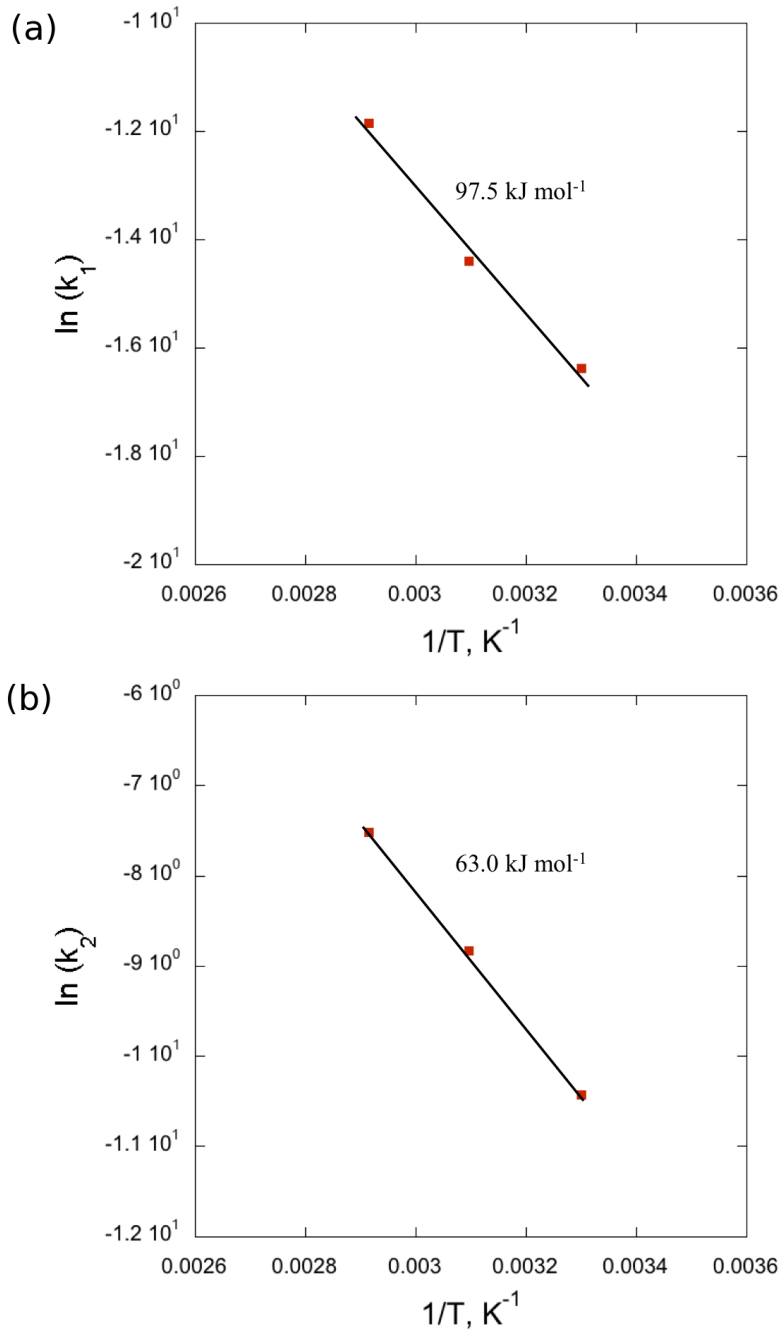

Figure 4.6. Determination of the (a) E_1 and (b) E_2 activation Kamal model parameters for the Epon 8132 – Epikure 3046 epoxy healing system.

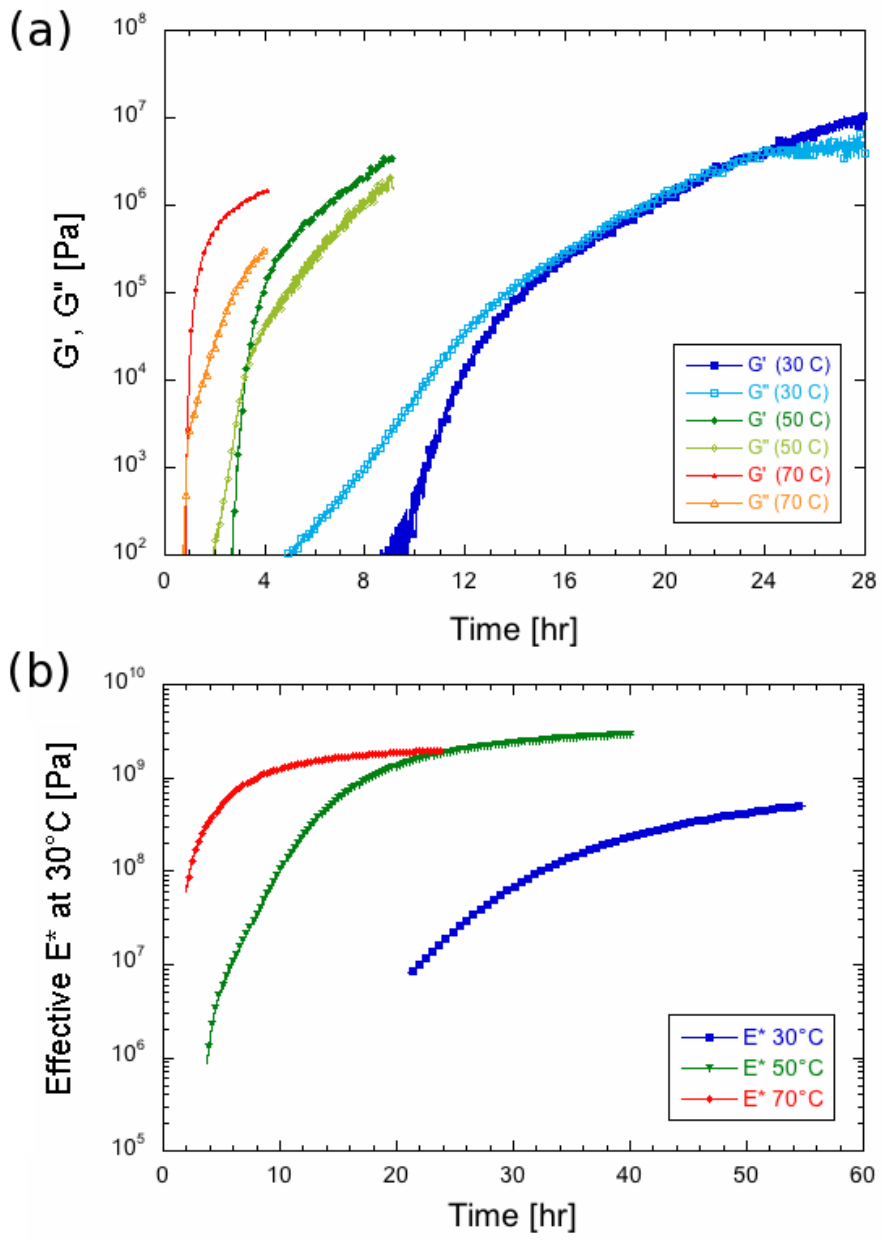

Figure 4.7. Semilog plots of (a) epoxy shear storage (G') and loss (G'') moduli and (b) complex modulus E^* for stoichiometric epoxy resin and hardener mixtures. The E^* data are measured at elevated temperatures and then scaled by ratios of $E^*(50°C)/E^*(30°C)$ or $E^*(70°C)/E^*(30°C)$ for a fully cured sample.

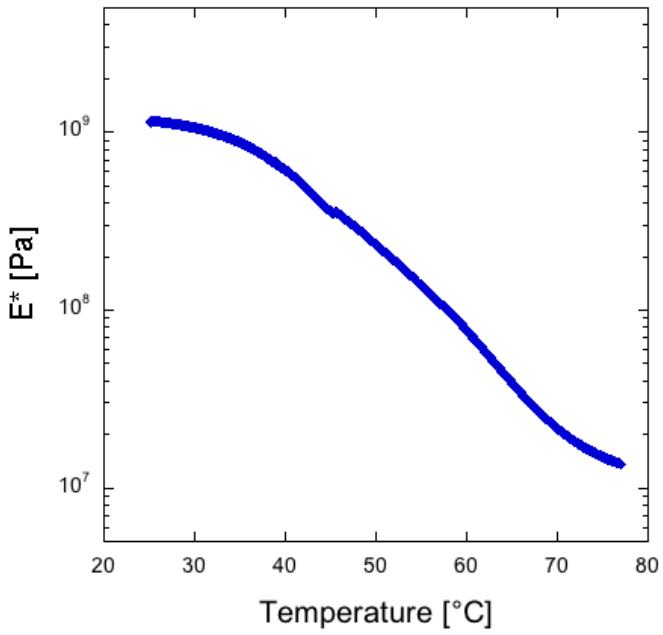

Figure 4.8. Complex elastic modulus E^* for fully cured epoxy material measured by dynamic mechanical analysis with varying temperature.

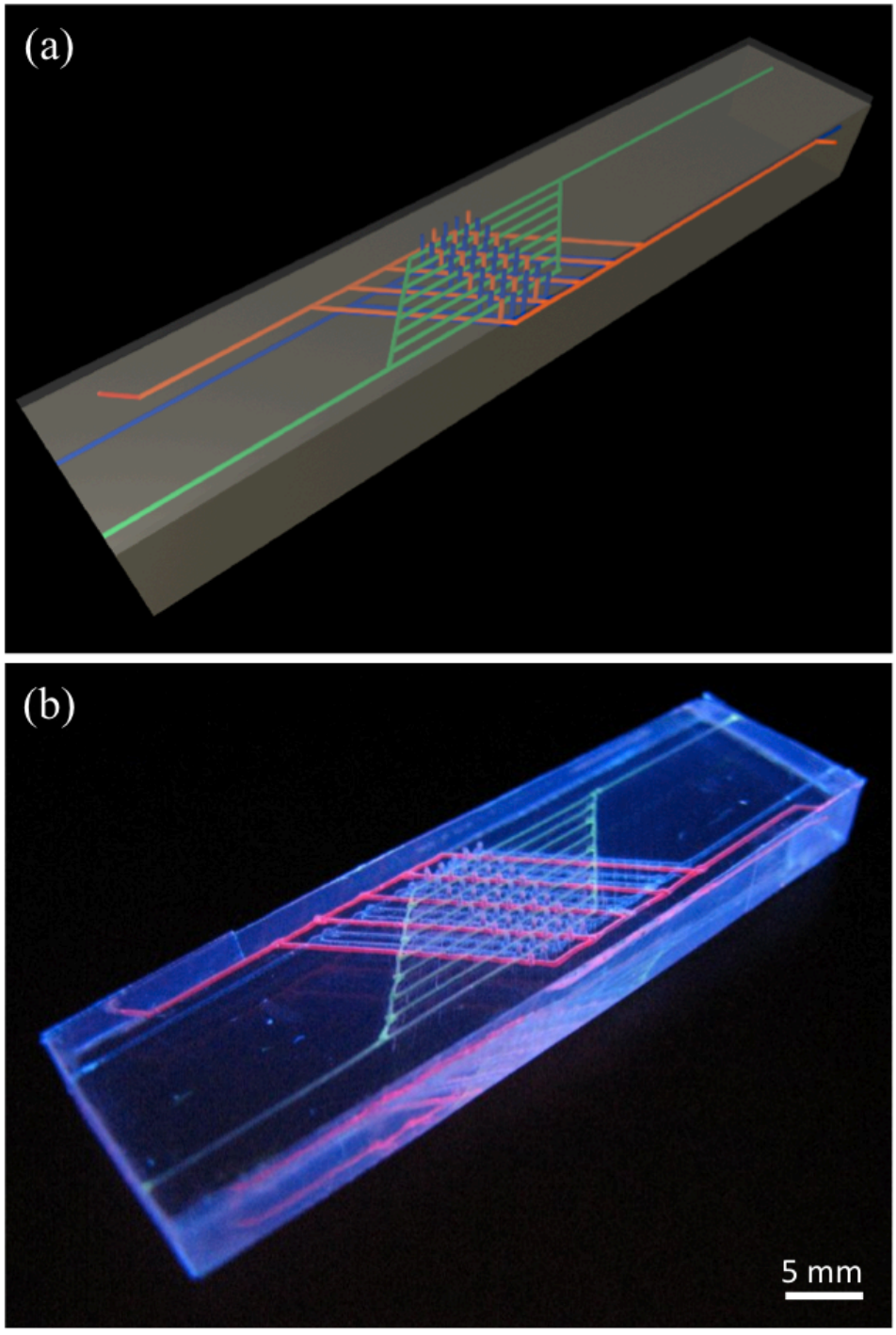

Figure 4.9. (a) Schematic view of epoxy coating/substrate architecture with embedded interpenetrating microvascular networks. Two of these networks house epoxy resin (blue) and hardener (red), while the third network provides thermal control (green) to accelerate healing kinetics after damage occurs. (b) Corresponding optical image of this novel self-healing system fabricated by direct-write assembly and then imaged with different fluorescent dye solutions within each network.

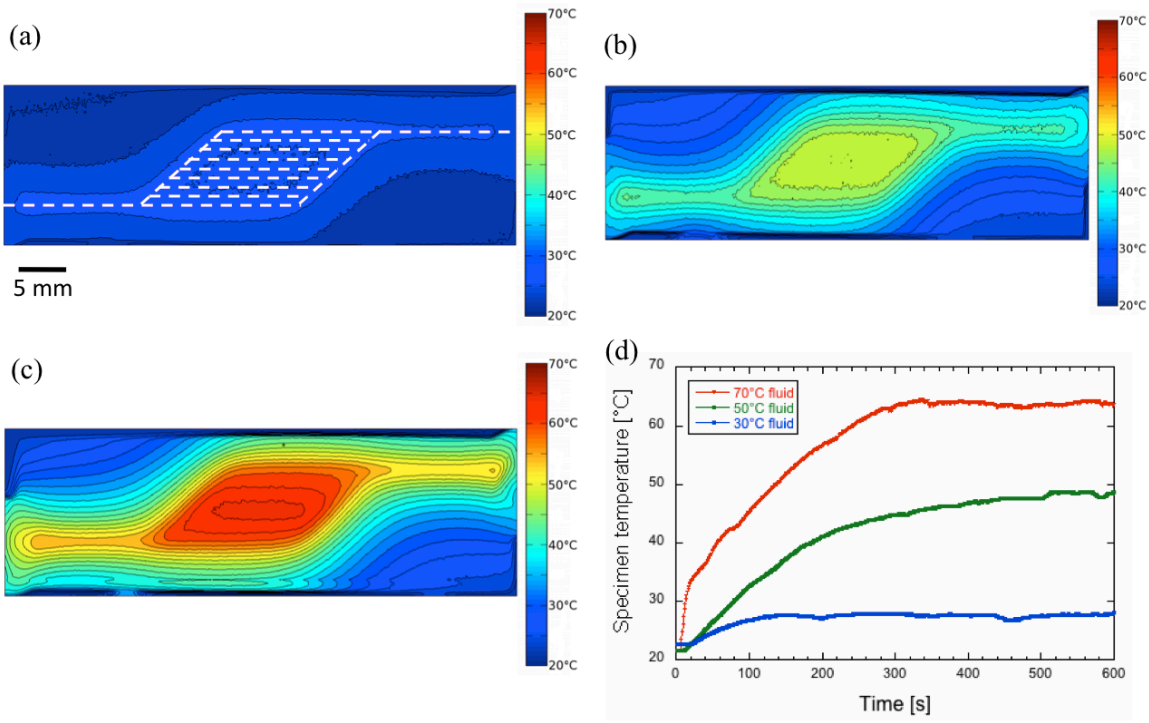

Figure 4.10. Infrared thermal imaging of epoxy coating/substrate architecture with embedded ternary microvascular networks acquired after circulating heated water for 10 minutes at a flow rate of 5 mL/min of varying temperature; (a) 30°C, (b) 50°C and (c) 70°C. Contour lines denote temperature change of 2°C. The location of the thermal regulating, microvascular network is indicated by dashed lines in (a), with flow direction from left to right. (d) Plot of the time-dependence of the average temperature of the region above the vertical conduits.

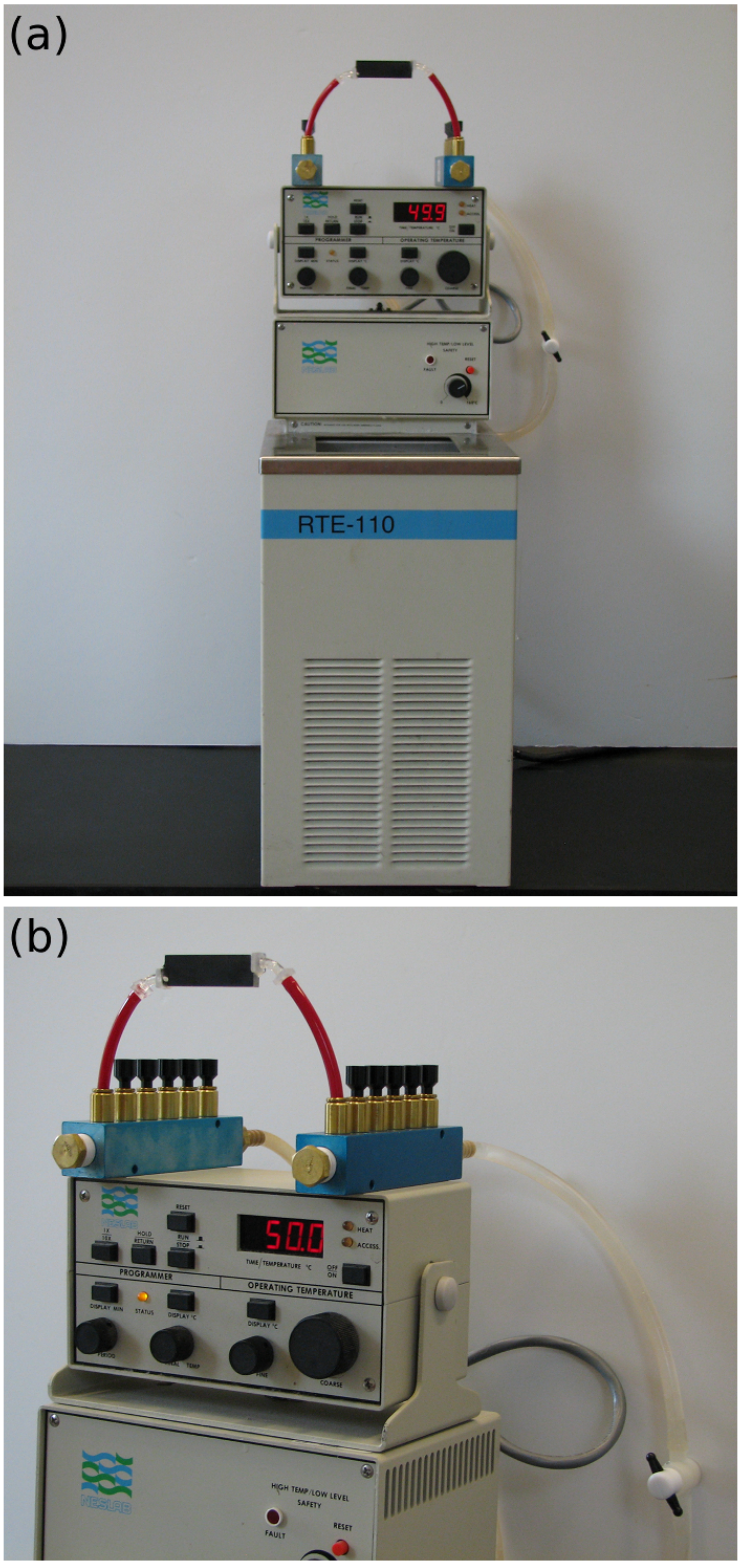

Figure 4.11. (a) Thermally regulated circulating bath connected via tubing to circulate heated fluid. (b) One specimen connected to heated circulating water, with up to 5 additional sample connections for parallel testing.

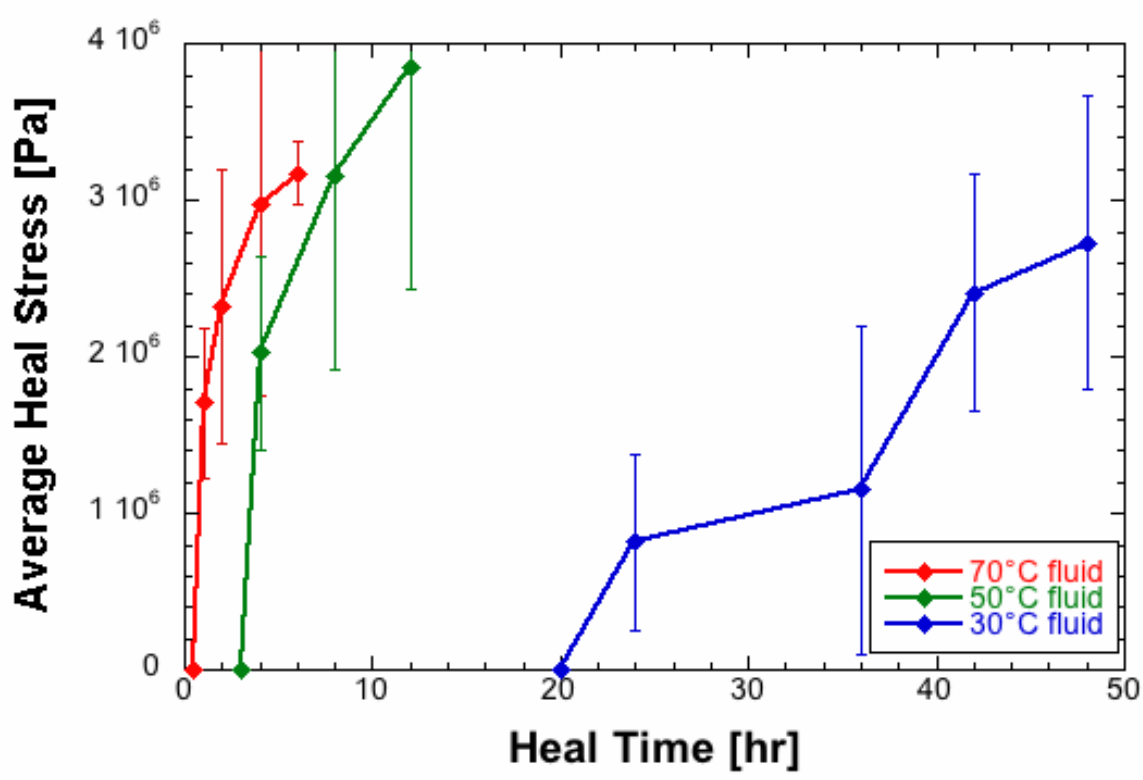

Figure 4.12. Average heal stress for epoxy coating/substrate architectures with embedded ternary interpenetrating microvasculature locally heated to 30, 50, or 70°C as a function of time. Error bars denote one standard deviation for the samples tested.

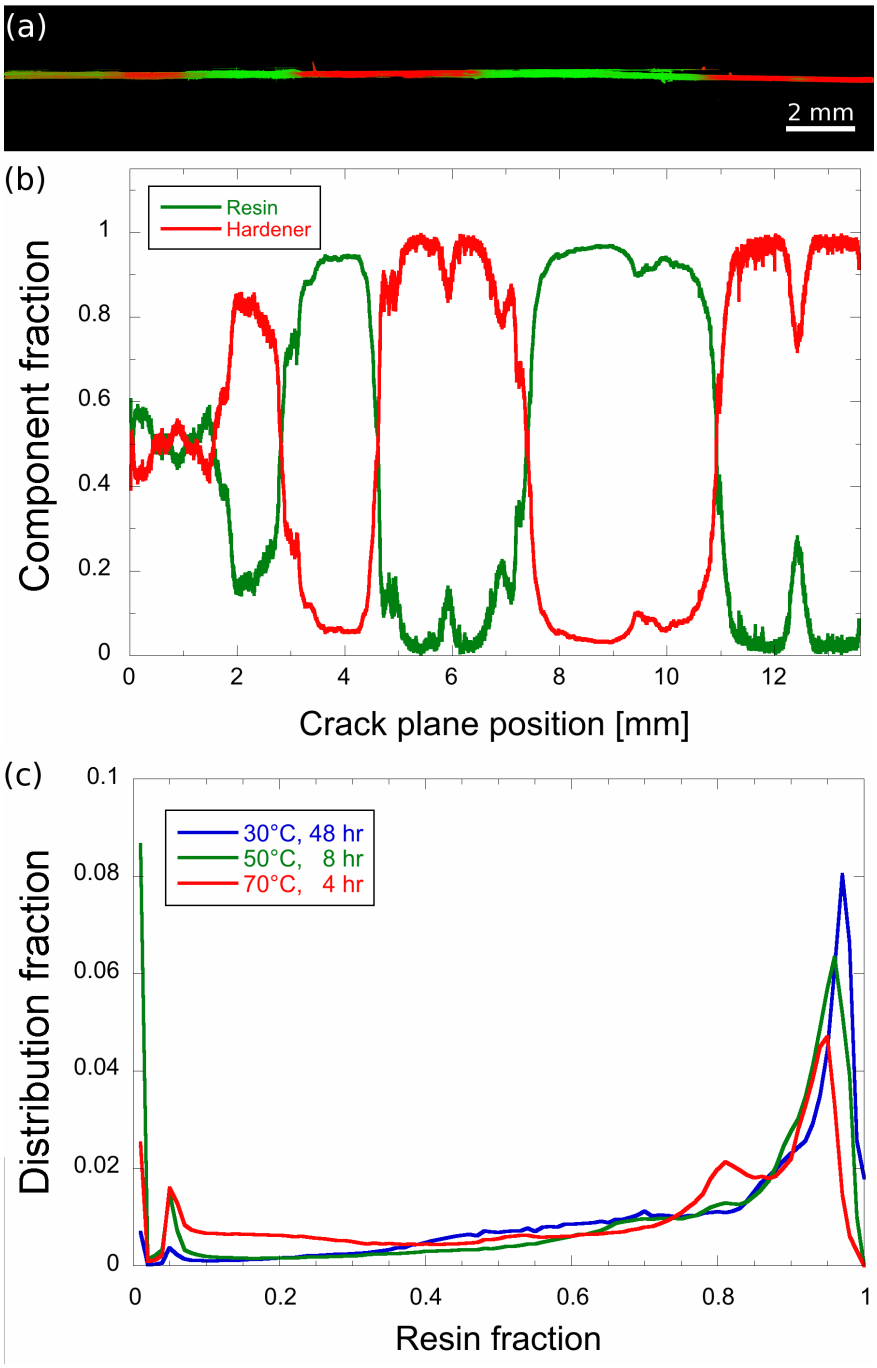

Figure 4.13. Epoxy mixing in the specimen. (a) Representative tiled image of fluorescently dyed epoxy resin (green) and hardener (red) that fill a crack region. (b) Resin and hardener composition fractions along the length of the damaged region. Compositions are sampled every 1.5 μm. (c) Composition distribution of epoxy resin and hardener that have partially mixed within the crack plane. Each line is the average for all specimens at the respective temperature.

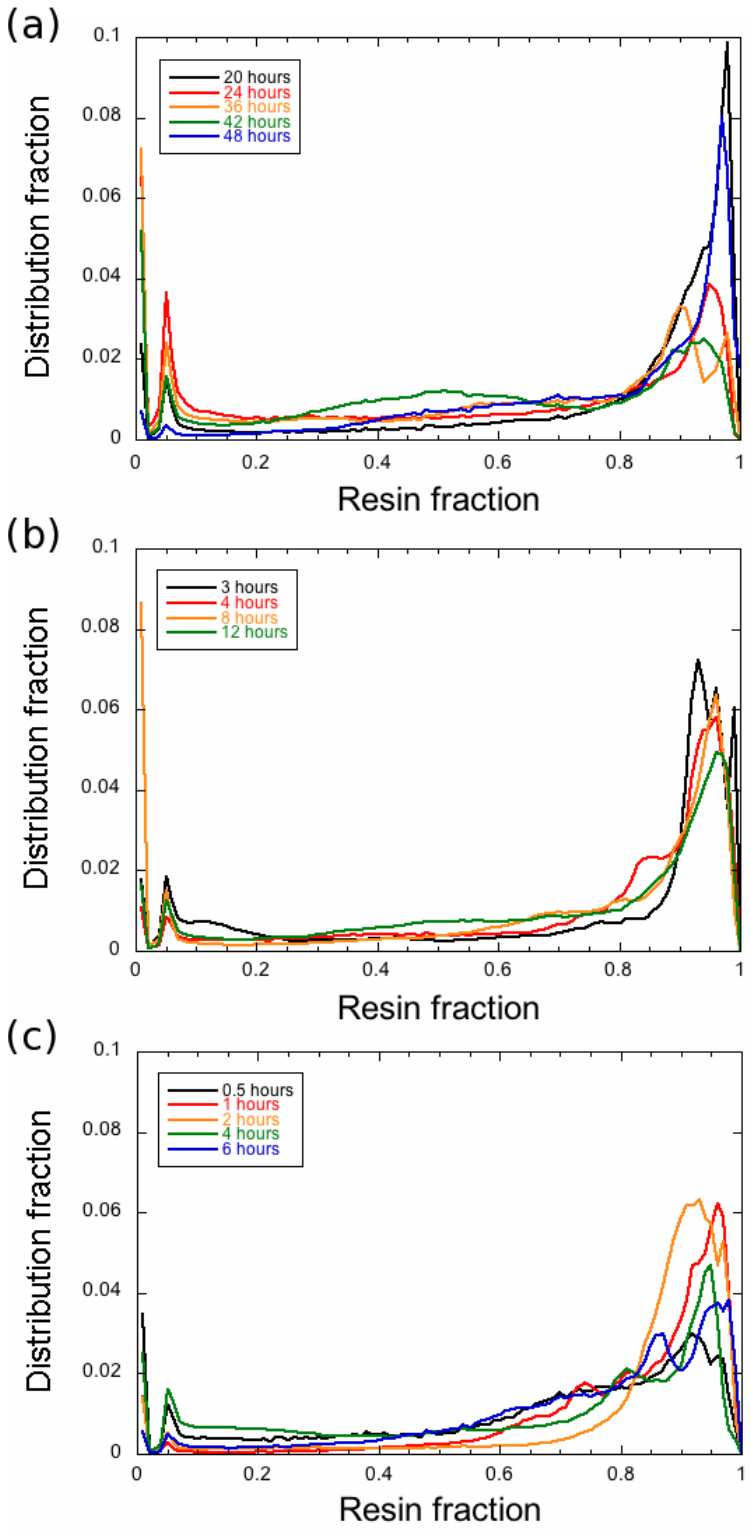

Figure 4.14. Average distribution of epoxy constituents observed in the crack planes of samples held at (a) 30°C, (b) 50°C and (c) 70°C for varying times.

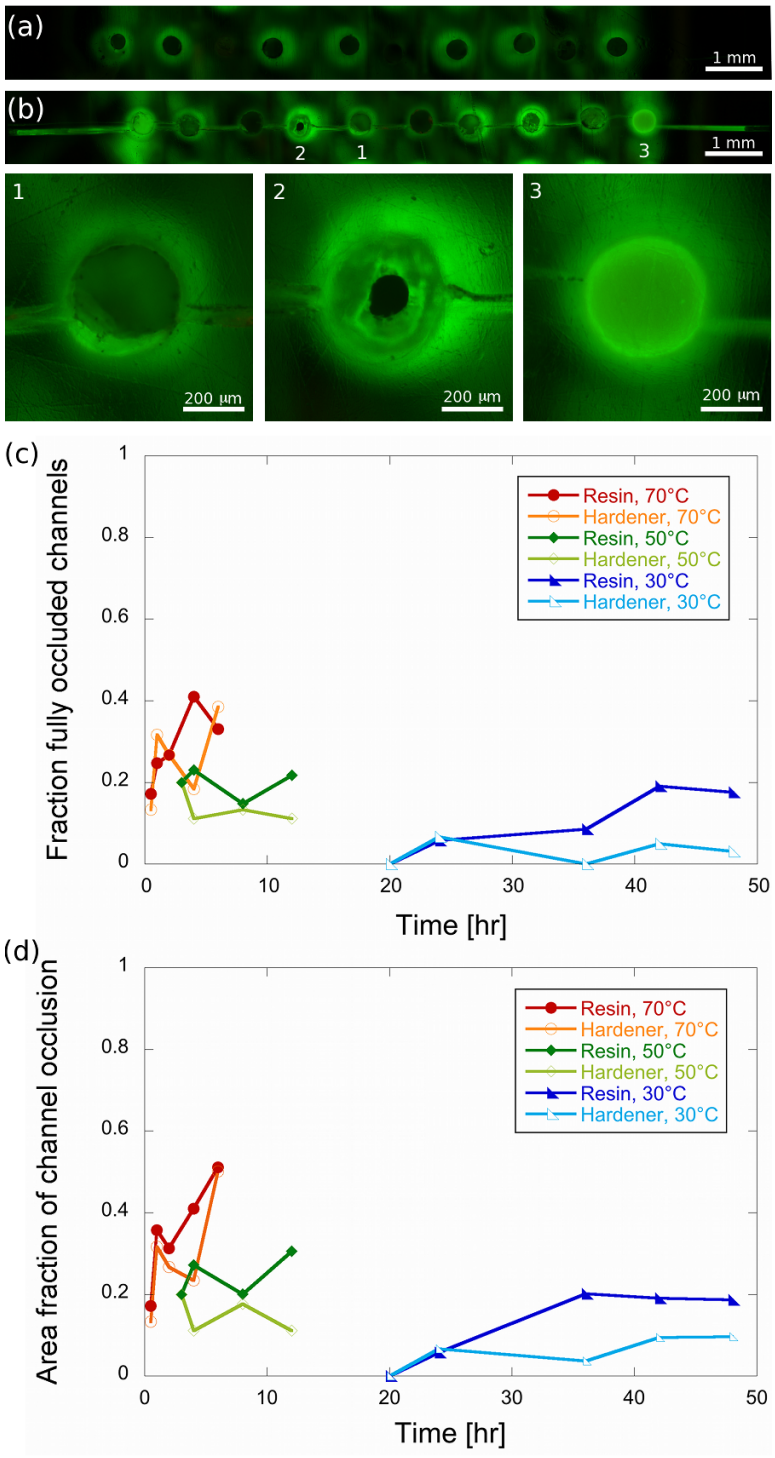

Figure 4.15. (a) Fluorescence image for conduits that do not intersect a crack. (b) Fluorescence image for conduits underneath a crack. Significant polymerized material is present and includes both partial (conduits labeled 1 and 2) and full (conduit labeled 3) obstructions. (c) Fraction of fully occluded conduits. (d) Fraction of partially occluded conduits.

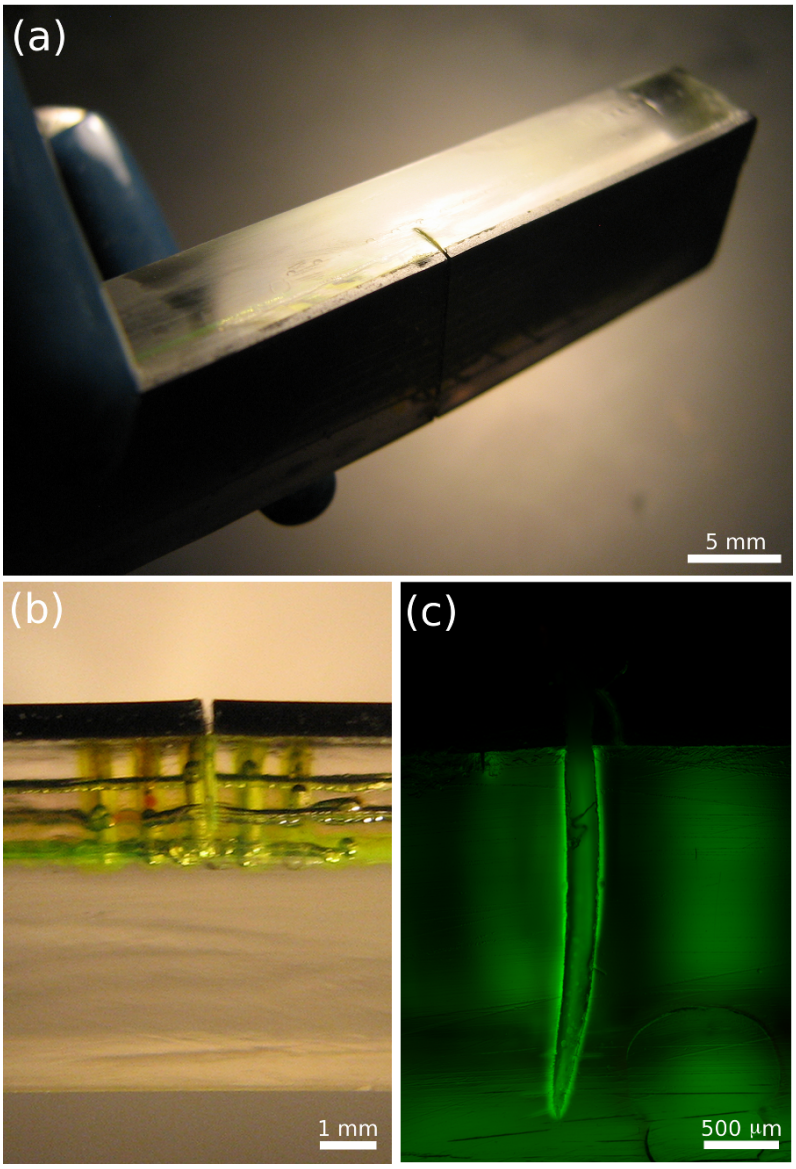

Figure 4.16. (a) Sample tested at 70°C with a crack that propagated into the substrate. (b) Side view of the fracture that has compromised the circulating network (i.e., horizontal channel closest to coating). (c) Fluorescence micrograph indicating epoxy material polymerized within the substrate region.

CHAPTER 5

MICROVASCULAR MULTINOZZLE PRINTHEADS FOR HIGH THROUGHPUT PRINTING

5.1 Introduction

Additive manufacturing encompasses a class of fabrication techniques in which structures are built in a "bottom up" mode. This paradigm is gaining acceptance as a low-cost production method for custom-designed components.[1-3] However, additive fabrication remains a relatively slow process that is often materials limited.

To enable high throughput patterning, several techniques have been recently modified to incorporate parallelization schemes. For example, inkjet printing utilizes silicon-based microfluidic printheads to eject microscale droplets via resistance heating or piezoelectric transducers.[4] Massively parallel variants of dip pen nanolithography, such as polymer pen lithography and hard-tip, soft-spring lithography, use multi-tip arrays composed of silicon or PDMS that deposit a low viscosity ink on a substrate to yield 2D nanoscale patterns.[5, 6] Parallel electrospinning simultaneously deposits nanofibers onto a substrate from independent and separate nozzles.[7, 8] Projection micro-stereolithography, a layer-by-layer manufacturing approach, enables fabrication via a digital micro-mirror dynamic mask, which selectively polymerizes voxels in parallel.[9] Each of these techniques, however, requires either low viscosity inks with dilute concentrations of the desired material or a restricted set of photocurable resins. The ability to pattern highly concentrated pastes or gels in a high throughput manner would broaden the palette of suitable materials and create devices that exhibit minimal shrinkage and deformation. The possibility of large scale, rapid production of planar and

3D microstructured components has broad relevance to fields such as printed electronics[10], solar cells[11], microfluidics[12], novel composites[13], and tissue engineering[14].

Direct-write assembly is a filamentary printing technique that is compatible with numerous highly concentrated ink systems[15] and offers the flexibility to pattern complex 3D shapes[16] over sub-micron to millimeter feature length scales. To date, however, this versatile technique has been restricted to serial deposition from a single nozzle[17]. To overcome the lengthy fabrication times needed to create large-scale structures, multinozzle arrays must be designed and demonstrated. In this chapter, we create a 64 nozzle printhead based on a hierarchical branching microvasculature for highly parallelized deposition of concentrated ink filaments. The distribution of flow velocities across individual nozzles is determined by microscopic particle image velocimetry (μ-PIV). Finally, we demonstrate uniform printing of parallel filament arrays over areas of ~1 m^2 using fugitive organic inks and photocurable resins.

5.2 Experimental Methods

5.2.1 Microvascular Multinozzle Fabrication and Assembly

Multinozzle arrays are manufactured in poly(methyl methacrylate) (PMMA) due to its ease of machining, ability to solvent weld, and to withstand high pressure without deformation. PMMA polymer blocks (2 x 2 x 0.5 in.) are mounted to a CNC-mill system (8540, Sherline Products Inc.) controlled by a G-code motion-control file specific to each design. A fly cutter is used to level the block surface relative to the CNC-mill *x*-*y*-*z* axes. Features 508 μm or smaller are milled with a 200 μm square-end end mill (Ultra-Tool

International), while features 635 μm or larger are milled with a 635 μm end mill. The channel depths are measured with an optical profilometer (LT-9010M, Keyence) and the piece is polished on a polishing wheel (Buehler Inc.) until the channel depths are within 5 μm of the intended depth and each channel is within ±2 μm across all 64 channels. The reservoir input(s) are machined with a 3/8" square-end drill bit and threaded with a 1/8-27 pipe thread with a 11/32" drill diameter. The network is cleaned by ultrasonication in water for 15 min intervals, with the channels rinsed between sonication steps. Any burrs that remain are removed by gently cleaning with either a 100 μm metal syringe tip (EFD, Inc.) or a pulled glass capillary. The microchannels are completely filled with a fugitive wax (Purester 24, Strahl & Pitsch) to prevent swelling during solvent welding. The solvents acetone and dichloromethane caused bulk polymer flow at the swollen interface, so acetonitrile is chosen for its minimal swelling distortion and negligible polymer flow under pressure. For a single multinozzle network printhead, a pure PMMA block (13 mm thick) is set on parafilm and acetonitrile is pipetted onto its surface. The microvascular PMMA block is carefully placed in contact with the solvent while avoiding bubble entrainment, and the pieces are quickly pressed together on an isostatic press (Model C, Carver Laboratory) for 15 min or longer. For multiple material deposition nozzles, the first nozzle is welded to a thinner PMMA block (1-3 mm thick). The welded piece is then flipped and a second milled network is aligned to the first piece with a jig and subsequently solvent welded under pressure. A combination of milling and polishing are used to expose the nozzles. Each output length is measured with an optical microscope (DMI 6000B, Leica Microsystems) and polishing continues until the final generation

lengths are equal to within ±10 μm. Finally, the part face is recessed by ~1-2 mm, except for the multinozzle outputs and a 1 mm surrounding border.

5.2.2 Computational Fluid Modeling

The 3D finite volume element model of the multinozzle geometry is created, modified, and meshed in GAMBIT (ANSYS Inc.). The boundary conditions consist of a constant mass flow into the inlet, a constant pressure at the outlets, and a no-slip condition at the channel walls. Uniformity of fluid flow is computationally modeled with ANSYS FLUENT (v.13, ANSYS Inc.) using Newtonian fluid models for either water or glycerol. The 2D finite area element model of the multinozzle geometry is modeled with COMSOL Multiphysics using the Chemical Engineering Modulue. The wax ink is modeled as a power law fluid, where the consistency parameter (K) and power law parameter (n) were determined experimentally from $\eta(\dot{\gamma})$.[18] The modeled flow velocity is averaged on an area-weighted basis at the nozzle exit for comparison to μ–PIV flow experiments. The volumetric flow rate (for 3D) or area flow rate (for 2D) are reported, as this parameter is paramount to ensure the uniformity of the as-printed ink filaments.

5.2.3 μ–PIV Measurements

μ-PIV measurements are carried out on microvascular nozzle arrays that are modified to include a collection reservoir that captures the flow output (see Figure 5.3a). The surface is encapsulated with a clear pressure-sensitive adhesive layer (3M Inc.) and all channels are verified by optical microscopy to be free of debris. For high viscosity fluids that cause adhesive layer debonding, the layer is reinforced in the reservoir region by adhering a glass slide with a UV-curable adhesive (NOA 61, Norland Products Inc.).

Suspensions of either deionized water or glycerol with 1.0 μm polystyrene particles dyed with nile red (F-8819, Invitrogen) are prepared (ϕ=0.024-0.03 v/v%) and loaded in 60 mL syringes (BD Syringe). The flow rate of the syringe pump (PHD2000, Harvard Apparatus) is measured by collecting data in LabView (v.2009, National Instruments) while water flows through the device to a balance (AG285, Mettler Toledo) in a humidity-controlled chamber.

Measurements are taken for a constant suspension flow rate after an initial start-up transient. A double-pulsed Nd:YAG laser (Solo PIV, New Wave Research) is directed through a 10X objective (N.A. = 0.30) on an upright microscope (Olympus BX60) to illuminate the region of interest. The particle light emission (λ_{peak} = 575 nm) is captured by a CCD camera (11 MP PowerView Plus, TSI). The μ–PIV images are collected with a time delay between successive image pairs sufficient to yield particle displacements in excess of 8 pixels. The images are interrogated with a two-frame cross correlation method with a vector grid spacing of $\Delta x = \Delta y$ = 26.976 μm. These parameters yield calculated vectors that represent the ensemble *x*-direction velocity in each microchannel midplane.

5.2.4 Ink Mixtures

Microcrystalline wax ink composed of 40 w/w% microcrystalline wax (SP-19, Strahl & Pitsch, Inc.) and 60 w/w% petroleum jelly (Vaseline, Inc.) is prepared by stirring the molten components at >100°C. The molten ink is filtered with a 25 mm diameter, 2 μm glass fiber filter (Millex AP 20 prefilter, Millipore) to remove impurities. The mixture is reheated for 15 min, then the ink is poured into a pump reservoir (500D, Teledyne, Inc.) held at 82°C by a circulating water bath. After all air bubbles float to the surface, the

reservoir is sealed and all air removed prior to pressurizing to 200 psi in order for the pump to compensate for ink volume changes upon solidification. The circulating bath is slowly cooled to room temperature overnight, according to the set-points listed in Table 5.1.

5.2.5 High Throughput Printing

High-throughput printing is carried out using a 64-nozzle printhead that is connected via high-pressure hose (US Hose Corporation) to the ink reservoir. The height of a large glass substrate is calibrated with an optical profilometer (LT-9010M, Keyence) so that the height variation is ±5 μm over 1 m^2. The printhead is mounted to the print stage (ABG10000, Aerotech Inc.) and material is deposited for velocities and applied pressures of 1-20 mm/s and 2-4 MPa, respectively. After deposition, filament height profiles are measured with the optical profilometer.

5.3 Results and Discussion

5.3.1 Multinozzle Printheads

Our multinozzle printheads mimic natural microvascular networks, and are therefore composed of branching channels, in which a large (parent) microchannel is repeatedly bifurcated into ever-smaller child branches. Specifically, our printheads distribute inks from a centralized reservoir to multiple distributed nozzles and conform to Murray's Law. Nearly a century ago, Murray calculated the optimum radii of branching microvascular vessels based on the minimum power requirement for the metabolic cost of blood and the viscous losses of fluid transport obeying Poiseuille's Law[19]. He

observed that the system is optimum when the cube of the parent branch radius (r_0) is equal to the sum of the cube of the child branch radii (r_1 and r_2):

$$r_0^3 = r_1^3 + r_2^3 \tag{5.1}$$

The derivation can be generalized to yield:

$$r_0^3 = \sum_i^n r_i^3 \tag{5.2}$$

where r_i are the radii of the n child branches.[20] When applied to the specific case of symmetrical bifurcated branching, the result is:

$$r_k = 2^{-k/3} r_0 \tag{5.3}$$

where r_k is the channel radius after k network bifurcations. This conforms to Young's Rule, proposed a century prior to Murray's derivation, for the ratio of a parent radius that bifurcates to equal child branches is equal to $2^{1/3}$.[21] Murray's law is extended to non-circular geometries through derivations that use the hydraulic diameter in lieu of the geometric diameter and a geometry-specific Poiseuille number.[22] For the specific case of square channel cross-sections, equation 5.2 is recovered.

The original derivation (equation 5.2) for systems with an associated volume cost applies to minimized dead volumes to conserve precious ink material when printing is constrained by a given pressure drop. A yet broader derivation for a constant vascular volume yields the same relationship for the radii as equation 5.2, indicating that any space-traversing microvascular network with Poiseuille flow will conform to Murray's law.[20] Though non-Newtonian printing inks will observe a modified optimum, the identical conductance of equally bifurcating network branches is expected to route fluid flow in a manner that results in uniform deposition across the entire nozzle array.

For a bifurcating microvascular design consisting of k generations, the final generation will possess 2^k branches. In order to substantially speed deposition, we choose to fabricate microvasculature with 6 branching generations, producing a total of 2^6 (or 64) nozzles. Features with square cross-sections and which are 200 μm on a side as desired. To maintain Murray's law, the microchannels are self-similar (i.e., channel length is proportional to the radius). The microvascular channel dimensions are provided in Table 5.2.

5.3.2 Computational Fluid Modeling

The flow uniformity of bifurcating multinozzle printheads is investigated with a commercial computational fluid modeling package. In the case of water flow in a symmetric bifurcating geometry (Figure 5.1a), the model predicts the intuitive result that uniform flow is achieved for steady-state laminar conditions over a broad range of typical printing velocities (Figure 5.4a). This flow uniformity also holds for both water and glycerol over 2 orders of magnitude for the exit flow velocity.

To evaluate the effects of microchannel non-uniformity within the multinozzle arrays, we systematically varied the width of a single channel and measured the resulting volumetric flow rate deviation(s). 3D steady state results reveal that the volumetric flow rate deviates from the mean by greater than 5% when the width of channel 1 is decreased by 5% or more (Figure 5.1b). 3D modeling of the fugitive wax ink is not possible due to computational instabilities induced by the shear rate-dependent viscosity model. However, convergence of the model is possible during 2D flow modeling. To investigate the effect of imperfections in the device fabrication on deposition quality, the dimensions of a single outlet are decreased in the model by ±1-10% (Figure 5.1c). The resulting flow

profiles indicate that printing with a viscoelastic ink can be achieved with nozzles that have dimensional changes of up to 5% (i.e., 10 μm for a 200 μm nozzle) before the flow profile deviates from the mean velocity by greater than 10%, which we empirically observe to be the limit of flow rate difference for continuous ink filament deposition.

5.3.3 Microvascular Multinozzles

The microvascular network (Figure 5.2a) is solvent welded to an acrylic block (Figure 5.2b) to create an embedded microvascular network (Figure 5.2c). The embedded microchannels conform to the desired dimensions within ±2-5 μm. For the 200 μm features, the observed deviation is less than 2.5% variation in width for all 64 printing nozzles, which the fluid modeling indicates is within acceptable tolerances. The sidewalls are vertical and the channel surface roughness is minimal (<1 μm).

To expand this nozzle design to allow for multi-material deposition, we created two multinozzle arrays and combined them within a single printhead. The two networks are identical in geometry, yet are supplied by two separate ink reservoirs. To create these multi-ink deposition nozzles (Fig. 5.5a), the network features are solvent welded with an offset equal to half the center-to-center spacing (Fig. 5.5b-c). During printing, the interstitial spaces created by the deposition of the first ink are designed to then immediately infiltrate with the second ink. The independence of exact bifurcation of flow in these networks with respect to the specific ink allows simultaneous patterning of inks with vastly different properties.

5.3.4 μ-PIV Characterization of Multinozzle Flow Uniformity

To validate the flow distribution profile of our hierarchical bifurcating microvascular design, microcropic particle image velocimetry (μ-PIV) is used to determine fluid

velocities within individual channels.[23] This technique determines instantaneous fluid velocity fields by correlating fluorescent particle positions in pairs of time-delayed images. We first attempt to capture the flow of a gelled ink similar to the Pluoronic fugitive ink. However, a 30 w/w% Pluronic triblock co-polymer in aqueous suspension with dyed latex particles (ϕ=0.00024) caused the glass slide-reinforced surface layer to debond and the syringe pump to stall. The suspension was then diluted to 21 w/w% Pluronic, which is the lowest gel strength possible at room temperature.[24] Despite these efforts, the ink remained too strongly gelled to flow through the imaging set-up. Hence, the channel flow uniformity is interrogated with Newtonian fluid suspensions with dilute concentrations of latex particles. Typical filamentary deposition occurs over a broad range of printing speeds, often 1 to 100 mm s^{-1}. To determine the effect of flow velocity on the equal distribution of fluid among nozzles, aqueous suspension input flow rates are chosen to span the two orders of magnitude of filamentary deposition velocities. The average individual velocity for all 64 nozzles are shown for target printing rates of ~1, 10 and 100 mm s^{-1} in Fig. 5.3a. For each flow velocity, the standard deviation as a fraction of the mean velocity U_{mean} (1.59, 14.7, and 144.3 mm s^{-1}) are within ±5%. This flow variation is close to the 1-5% volumetric flow variation of the syringe pump, as measured for 60 s bins of the flow rate. Some flow variation is likely due to imperfections of the fabricated microvascular geometry. An additional source of variation is the formation of bubbles in channels containing water suspensions. These bubbles often nucleate within the channels and need to periodically be flushed from the system. Due to the large lengths of channel in the bifurcating network, it is not possible to scan the entire array for microbubbles (i.e., less than ~25 μm), but rather bubbles are

expelled when they are visible to the eye (i.e., greater than ~50 μm). At this size, it is possible that bubbles may substantially impact flow uniformity. Printable inks, however, do not exhibit this behavior. Unfortunately, despite a rigorous filtering procedure, some debris (e.g., hair or fibers) remains in the ink, which, when trapped at bifurcations, can divert flow and reduce flow uniformity within the nozzle array.

Fugitive inks are substantially more viscous than these aqueous suspensions. To investigate the effect of viscosity on the flow distribution, a glycerol suspension with a viscosity μ of 832 cP at 22°C is flowed through the microvascular network. The glycerol viscosity is approximately three orders of magnitude greater than that of the aqueous suspensions (μ = 1 cP) and results in a concomitant decrease in *Re* ($Re_{glycerol}$ = 0.0023, $Re_{aqueous}$ = 2.2). For typical power law fluid inks,[18, 24] a comparable viscosity at the wall-fluid interface is estimated for deposition rates as low as 4.5 mm s^{-1}, though an unyielded core will remain for substantially higher velocities.[25] For a target printing rate of ~10 mm s^{-1}, the glycerol flow distribution (U_{mean} = 15.0 mm s^{-1}, $\sigma = 0.052U_{mean}$) is comparable to that of water (U_{mean} = 14.7 mm s^{-1}, $\sigma = 0.036U_{mean}$). The difference in standard deviation is statistically insignificant, indicating that the 2 order of magnitude difference in *Re* does not significantly affect flow uniformity.

5.3.5 Multinozzle Filamentary Deposition

To test the microvascular multinozzle design for high throughput deposition, we mount the printhead onto a 3-axis motion controlled stage capable of 1 m^2 deposition areas at speeds of up to 1 m/s. A microcrystalline wax ink is used for characterization tests of the deposition quality due to its low cost, bulk availability, and previous rheological characterization.[18] Prior to flow, we verify that all nozzles are clear of

debris for unobstructed flow (Fig. 5.5a). The first printhead design has 200 μm nozzles with a 400 μm center-to-center spacing for an anticipated 50% area coverage. The scalable deposition of filaments over large areas is successfully demonstrated over a 0.8 m^2 glass substrate (Fig. 5.5b). A single deposition pass quickly and simultaneously deposits 64 filaments (Fig. 5.6a) with small dimensional variation of the average filament height, h_{avg}, and width, w_{avg} (σ_h=0.025h_{avg}, σ_w=0.03w_{avg}). Deposition from similar printheads with 200 μm nozzles but either 800 μm (Fig. 5.6b) or 1600 μm (Fig. 5.6c) center-to-center spacings also exhibit uniform and continuous filamentary deposition. Filaments are successfully deposited for velocities ranging over an order of magnitude (~1 – 20 mm s^{-1}) while maintaining high profile fidelity. The effective single-nozzle print velocity, 1.25 m s^{-1}, is ~20 times faster than typical single-nozzle printing and is faster than the maximum motion capability of the deposition stage.

The dual microvascular network nozzles are used to create defined porosity structures from two inks with vastly different physical properties. The structures are built in a woodpile design with the embedded porosity defined by the microcrystalline wax ink, while the physical structure is constructed from a UV-curable urethane liquid. The wax ink is flowed through the nozzle array that leads the deposition with respect to the printing direction, while the trailing nozzle array deposits the urethane liquid within the grooves created by the wax features (Fig. 5.8a-c). The urethane is cured and the fugitive wax ink is removed to create a defined porosity microstructure whose shape and porosity can be easily controlled by the microvascular printhead design. Over deposition areas in excess of 0.5 m, infiltration of these structures after deposition is prohibitively long (>6 hr). Hence, the parallel deposition and infiltration process reduces manufacturing times

by over 90% relative to the serial process of multinozzle deposition followed by infiltration.

5.4 Conclusions

In summary, we have demonstrated the successful fabrication of and deposition from microvascular multinozzle printheads. The symmetric, bifurcating structures conform to the biological principle of Murray's law to minimize viscous resistance during deposition. Computational fluid modeling shows uniform flow through the networks for both Newtonian and non-Newtonian fluids and defines the dimensional tolerances for the smallest generation features. Micro-PIV flow experiments demonstrate flow that is sufficiently uniform for filamentary printing. Patterning of parallel filamentary features with multinozzle printheads results in a nearly two order of magnitude printing rate increase, demonstrating a manufacturing speed advantage that can be scaled yet further by increasing the number of bifurcating generations. The demonstrated ability to pattern polymeric gel inks, as well as traditional low visocity liquids, attest to the vast range of materials suitable for this technique.

5.5 References

1. J. G. Conley and H. L. Marcus, *Rapid prototyping and solid free form fabrication*. Journal of Manufacturing Science and Engineering-Transactions of the Asme, 1997, 119, p. 811-816.
2. D. W. Hutmacher, M. Sittinger, and M. V. Risbud, *Scaffold-based tissue engineering: rationale for computer-aided design and solid free-form fabrication systems*. Trends in Biotechnology, 2004, 22, p. 354-362.
3. S. F. Yang, K. F. Leong, Z. H. Du, and C. K. Chua, *The design of scaffolds for use in tissue engineering. Part II. Rapid prototyping techniques*. Tissue Engineering, 2002, 8, p. 1-11.

4. P. Calvert, *Inkjet Printing for Materials and Devices*. Chemistry of Materials, 2001, 13, p. 3299-3305.
5. W. Shim, A. B. Braunschweig, X. Liao, J. Chai, J. K. Lim, G. Zheng, and C. A. Mirkin, *Hard-tip, soft-spring lithography*. Nature, 2011, 469, p. 516-520.
6. F. Huo, Z. Zheng, G. Zheng, L. R. Giam, H. Zhang, and C. A. Mirkin, *Polymer Pen Lithography*. Science, 2008, 321, p. 1658-1660.
7. M. R. Ladd, S. J. Lee, J. D. Stitzel, A. Atala, and J. J. Yoo, *Co-electrospun dual scaffolding system with potential for muscle-tendon junction tissue engineering*. Biomaterials, 2011, 32, p. 1549-1559.
8. N. Q. Zhan, Y. X. Li, C. Q. Zhang, Y. Song, H. G. Wang, L. Sun, Q. B. Yang, and X. Hong, *A novel multinozzle electrospinning process for preparing superhydrophobic PS films with controllable bead-on-string/microfiber morphology*. Journal of Colloid and Interface Science, 2010, 345, p. 491-495.
9. C. Sun, N. Fang, D. M. Wu, and X. Zhang, *Projection micro-stereolithography using digital micro-mirror dynamic mask*. Sensors and Actuators A: Physical, 2005, 121, p. 113-120.
10. B. Y. Ahn, E. B. Duoss, M. J. Motala, X. Guo, S.-I. Park, Y. Xiong, J. Yoon, R. G. Nuzzo, J. A. Rogers, and J. A. Lewis, *Omnidirectional Printing of Flexible, Stretchable, and Spanning Silver Microelectrodes*. Science, 2009, 323, p. 1590-1593.
11. J. Yoon, A. J. Baca, S. I. Park, P. Elvikis, J. B. Geddes, 3rd, L. Li, R. H. Kim, J. Xiao, S. Wang, T. H. Kim, M. J. Motala, B. Y. Ahn, E. B. Duoss, J. A. Lewis, R. G. Nuzzo, P. M. Ferreira, Y. Huang, A. Rockett, and J. A. Rogers, *Ultrathin silicon solar microcells for semitransparent, mechanically flexible and microconcentrator module designs*. Nature materials, 2008, 7, p. 907-915.
12. J. C. McDonald, D. C. Duffy, J. R. Anderson, D. T. Chiu, H. K. Wu, O. J. A. Schueller, and G. M. Whitesides, *Fabrication of microfluidic systems in poly(dimethylsiloxane)*. Electrophoresis, 2000, 21, p. 27-40.
13. R. LAKES, *Foam Structures with a Negative Poisson's Ratio*. Science, 1987, 235, p. 1038-1040.
14. L. G. Griffith and G. Naughton, *Tissue Engineering--Current Challenges and Expanding Opportunities*. Science, 2002, 295, p. 1009-1014.
15. J. A. Lewis, *Colloidal Processing of Ceramics*. Journal of the American Ceramic Society, 2000, 83, p. 2341-2359.
16. G. M. Gratson, M. Xu, and J. A. Lewis, *Microperiodic structures: Direct writing of three-dimensional webs*. Nature, 2004, 428, p. 386-386.
17. J. A. Lewis, *Direct Ink Writing of 3D Functional Materials*. Advanced Functional Materials, 2006, 16, p. 2193-2204.
18. D. Therriault, S. R. White, and J. A. Lewis, *Rheological behavior of fugitive organic inks for direct-write assembly*. Applied Rheology, 2007, 17, p. 10112-10120.
19. C. D. Murray, *The Physiological Principle of Minimum Work*. Proceedings of the National Academy of Sciences, 1926, 12, p. 207-214.
20. T. F. Sherman, *On connecting large vessels to small*. Journal of General Physiology, 1981, 78, p. 431-453.

21. T. Young, *On the function of the heart and arteries*. Philosophical Transactions of the Royal Society London, 1809, p. 1-31.
22. D. R. Emerson, K. Cieślicki, X. Gu, and R. W. Barber, *Biomimetic design of microfluidic manifolds based on a generalised Murray's law*. Lab on a Chip, 2006, 6, p. 447-454.
23. B. D. Kozola, L. A. Shipton, V. K. Natrajan, K. T. Christensen, and S. R. White, *Characterization of Active Cooling and Flow Distribution in Microvascular Polymers*. Journal of Intelligent Material Systems and Structures, 2010, 21, p. 1147-1156.
24. W. Wu, A. DeConinck, and J. A. Lewis, *Omnidirectional Printing of 3D Microvascular Networks*. Advanced Materials, 2011, 23, p.
25. M. T. Roberts, A. Mohraz, K. T. Christensen, and J. A. Lewis, *Direct Flow Visualization of Colloidal Gels in Microfluidic Channels*. Langmuir, 2007, 23, p. 8726-8731.

5.6 Tables

Table 5.1. Cooling profile set-points for solidifying 500 mL of microcrystalline wax

Step start/end temperature °C	**Step duration [hr:min:sec]**
82/81	00:01:00
81/80	00:10:00
80/75	00:45:00
75/60	10:00:00
60/50	02:00:00
50/40	01:00:00
40/30	00:45:00
30/22	00:15:00

Table 5.2. Dimensions of the microvascular bifurcating network

Generation	w/w_6	w **[μm]**	L **[mm]**
0	4.0	800	10.0
1	3.175	635	
2	2.520	508	
3	2.0	400	5.0
4	1.587	317.5	3.97
5	1.260	252	3.15
6	1.0	200	2.50

5.7 Figures

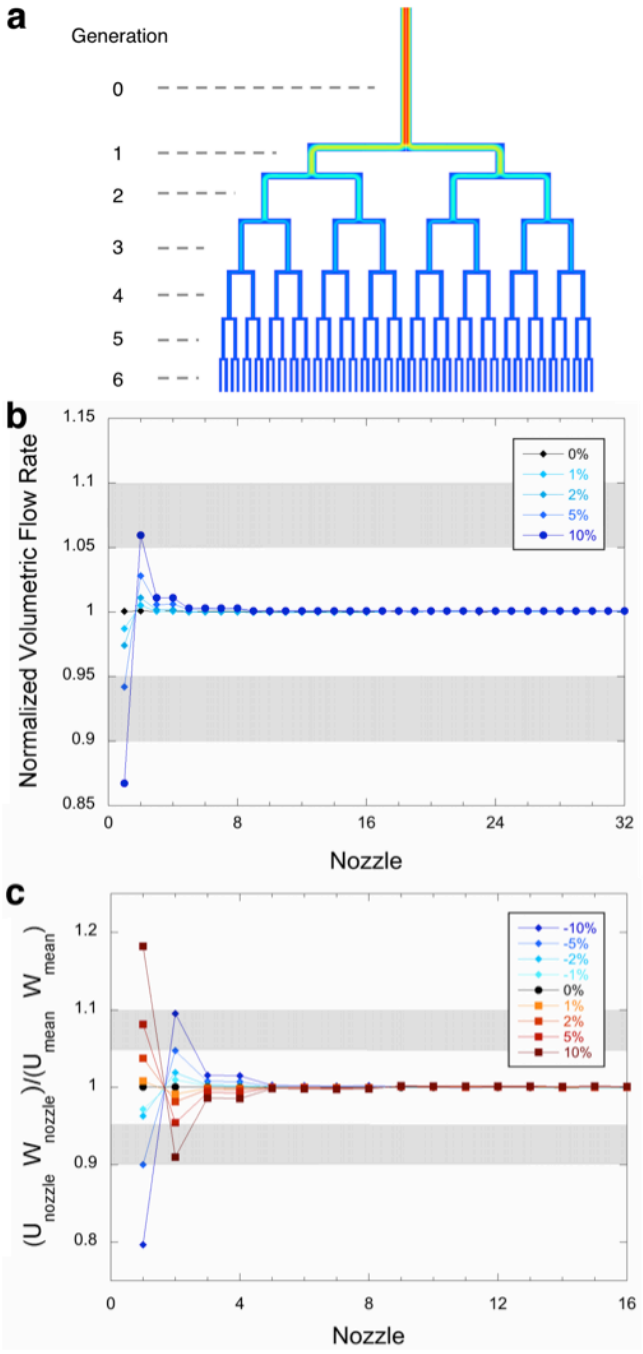

Figure 5.1. (a) Modeled fluid flow profile for water with U_{mean} = 10 mm s^{-1} at the outlets. (b) Modeled water volumetric flow rate normalized by the mean of all 64 nozzles. Channel 1 deviates from its 200 μm width by 0-10%. Grey bands indicate empirical limits of flow variation for printing. (c) Modeled wax area flow rate normalized by the mean all 64 nozzles. Channel 1 deviates from its 200 μm width by ±10%. Grey bands indicate empirical limits of flow variation for printing.

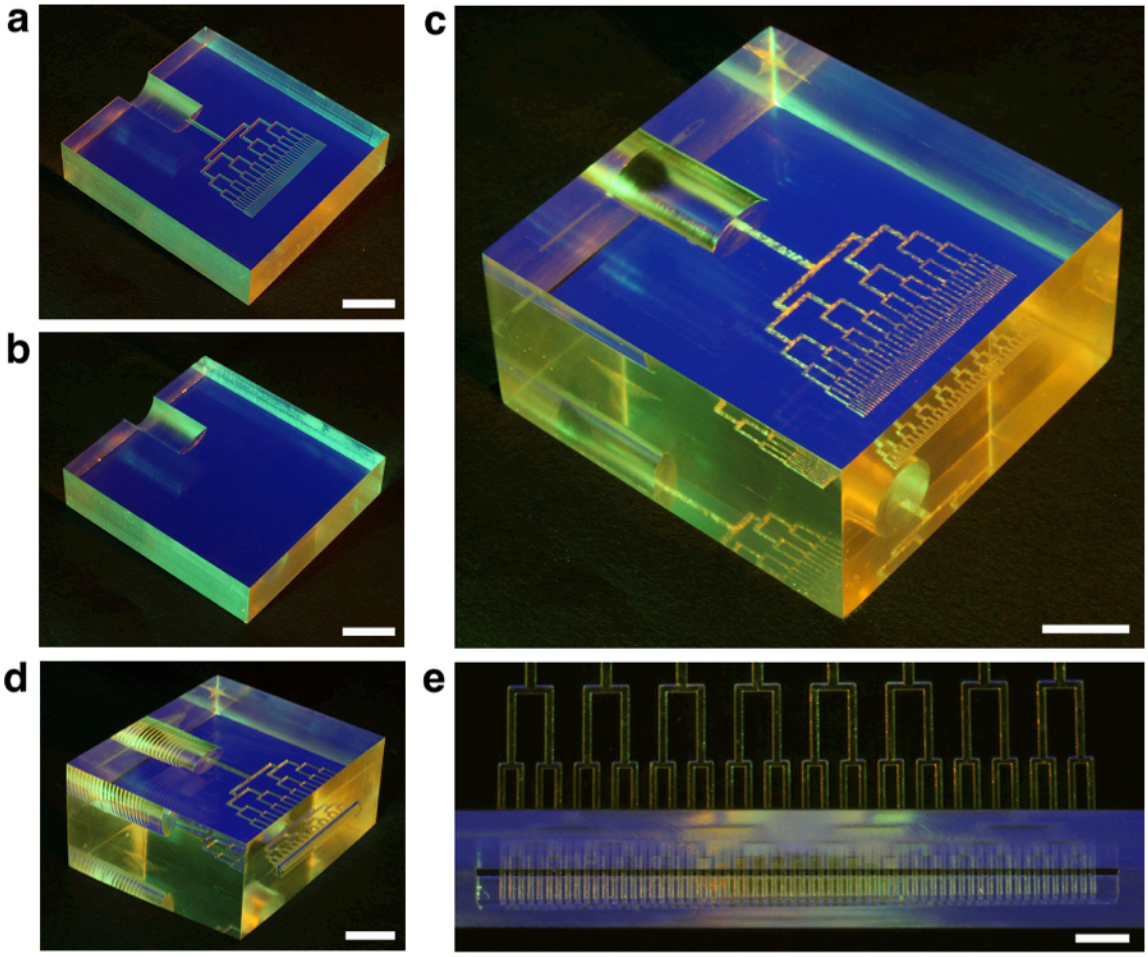

Figure 5.2. (a) Hierarchical microvascular channel network created by CNC milling, which is solvent welded to (b) a pristine acrylic block to form (c) the embedded microvascular structure. (d) The inlet is threaded and the bottom face of the device is milled and polished to expose the multinozzle array. (a)-(d) scale bars = 10 mm. (e) A view of the nozzles shows bifurcations terminate at 64 uniform and parallel outlets. Scale bar = 2 mm.

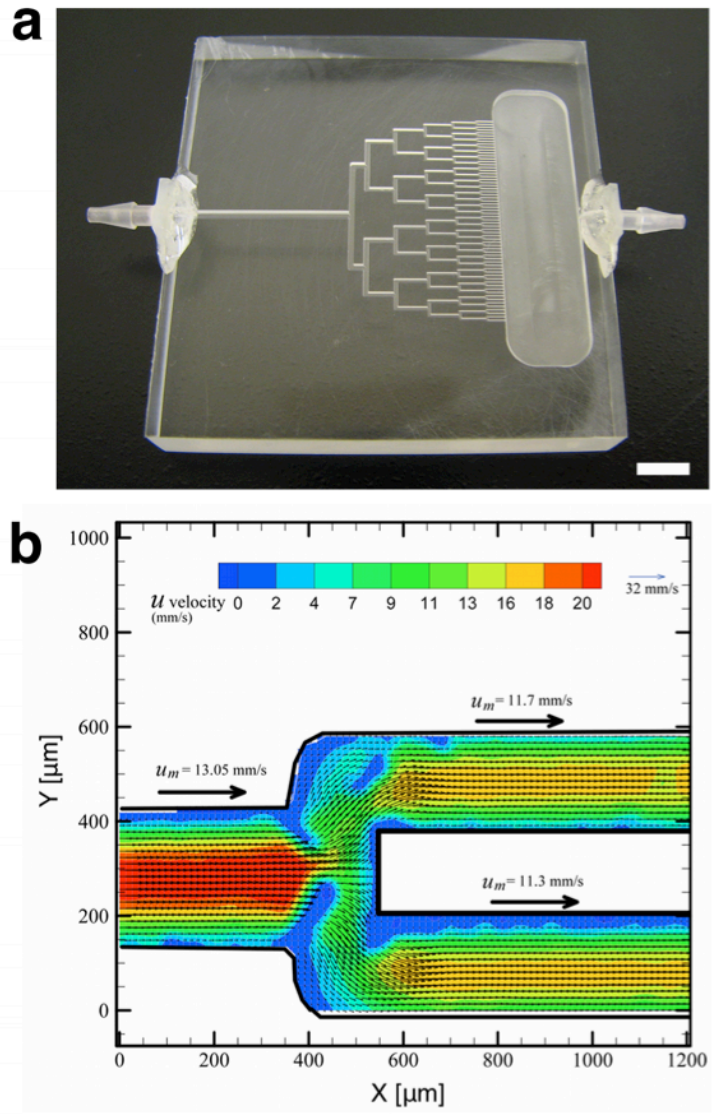

Figure 5.3. (a) Microvascular network modified to include a reservoir to collect fluid during µ-PIV experiments. Scale bar = 5 mm. (b) Ensemble average vector field from micro-PIV. Axial flow is well characterized, except for the bifurcation junction where excess background fluorescence precludes particle cross-correlations. (Graph courtesy R. Saksena.)

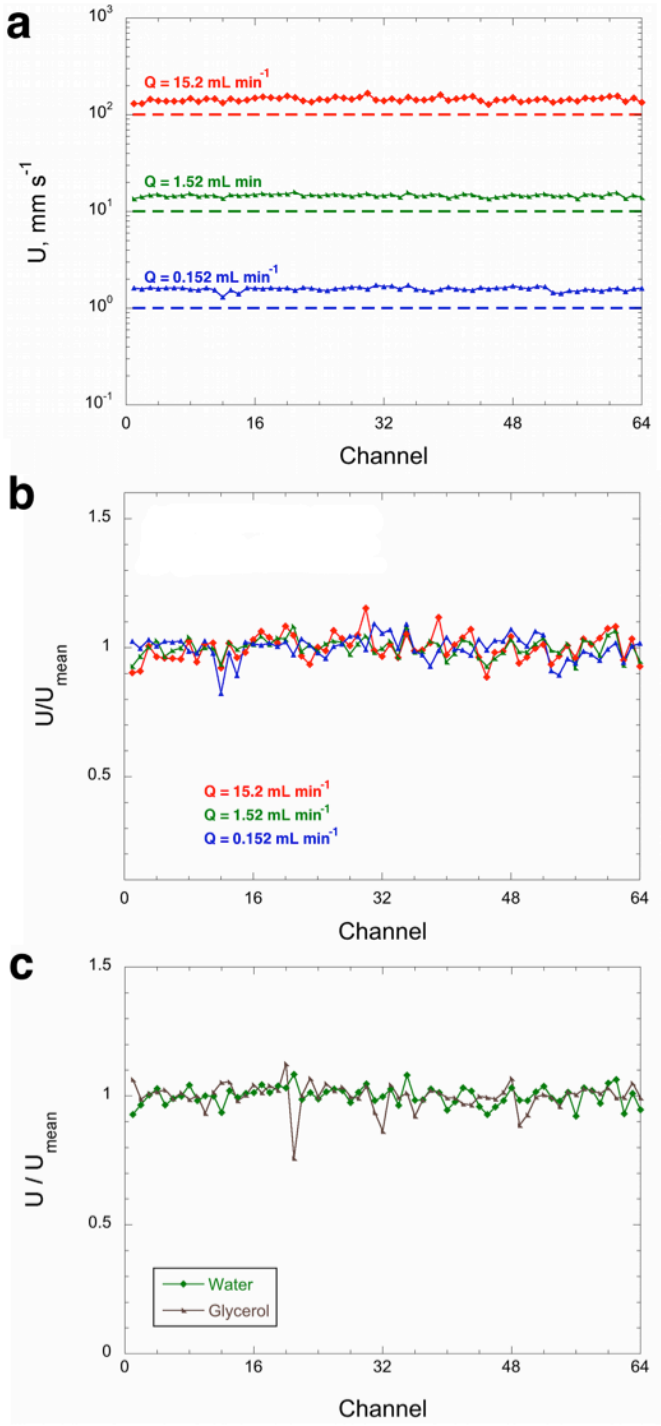

Figure 5.4. (a) Average axial velocity U measured by μ-PIV for each of the 64 outlet channels for input flow rates spanning 2 orders of magnitude. Dashed lines denote the computational fluid model results for the corresponding input flow rates. (b) Channel velocities (U) normalized by average velocity of all channels (U_{mean}). (c) Distribution of the normalized velocity for both water ($\phi_{\text{polystyrene}}$=0.00024) and glycerol ($\phi_{\text{polystyrene}}$ = 0.0003) input flow rate of 1.52 mL min^{-1}.

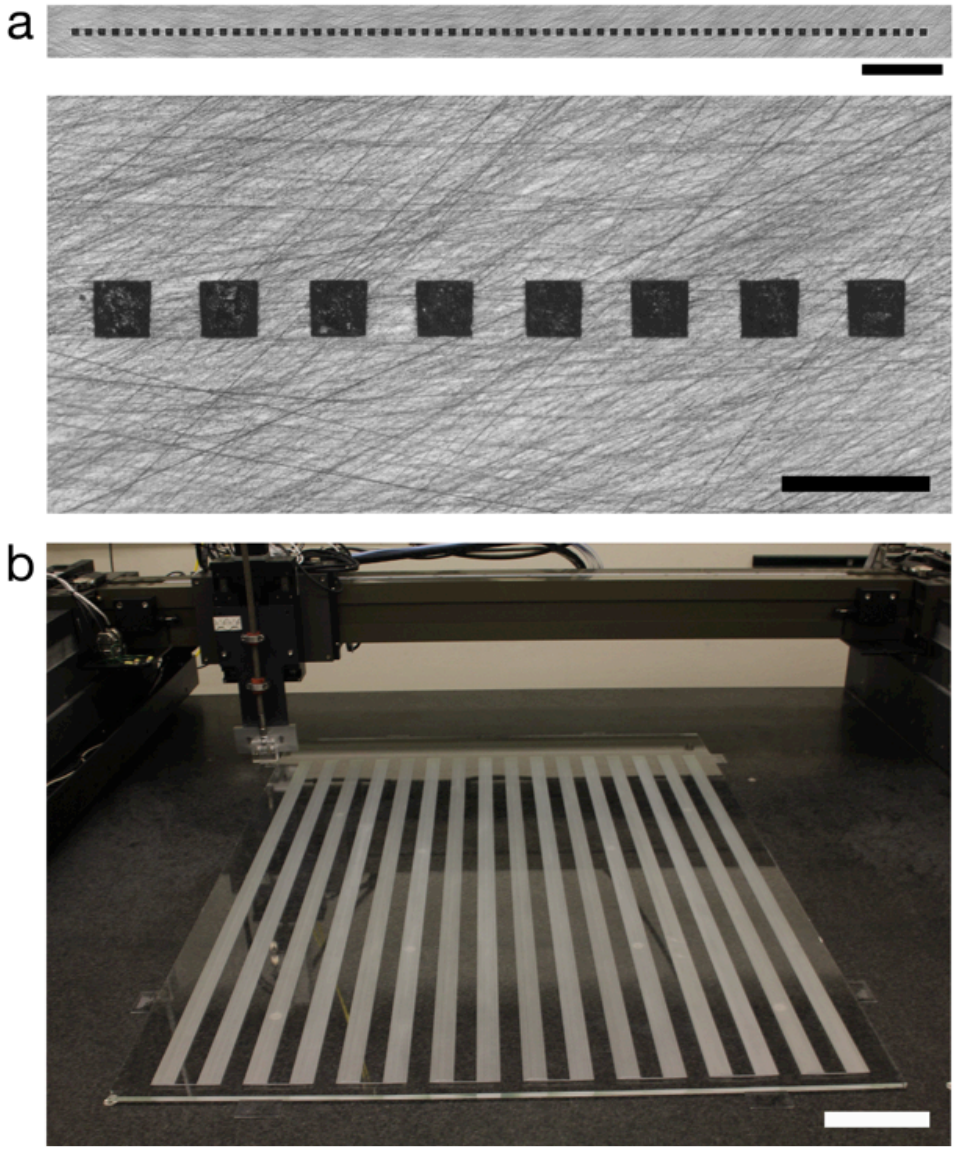

Figure 5.5. (a) Optical micrographs of all (top image, scale bar = 1 mm) and subset (bottom image, scale bar = 500 μm) of the printhead nozzles. (b) Large scale deposition over a 0.8 m^2 area (scale bar = 10 cm).

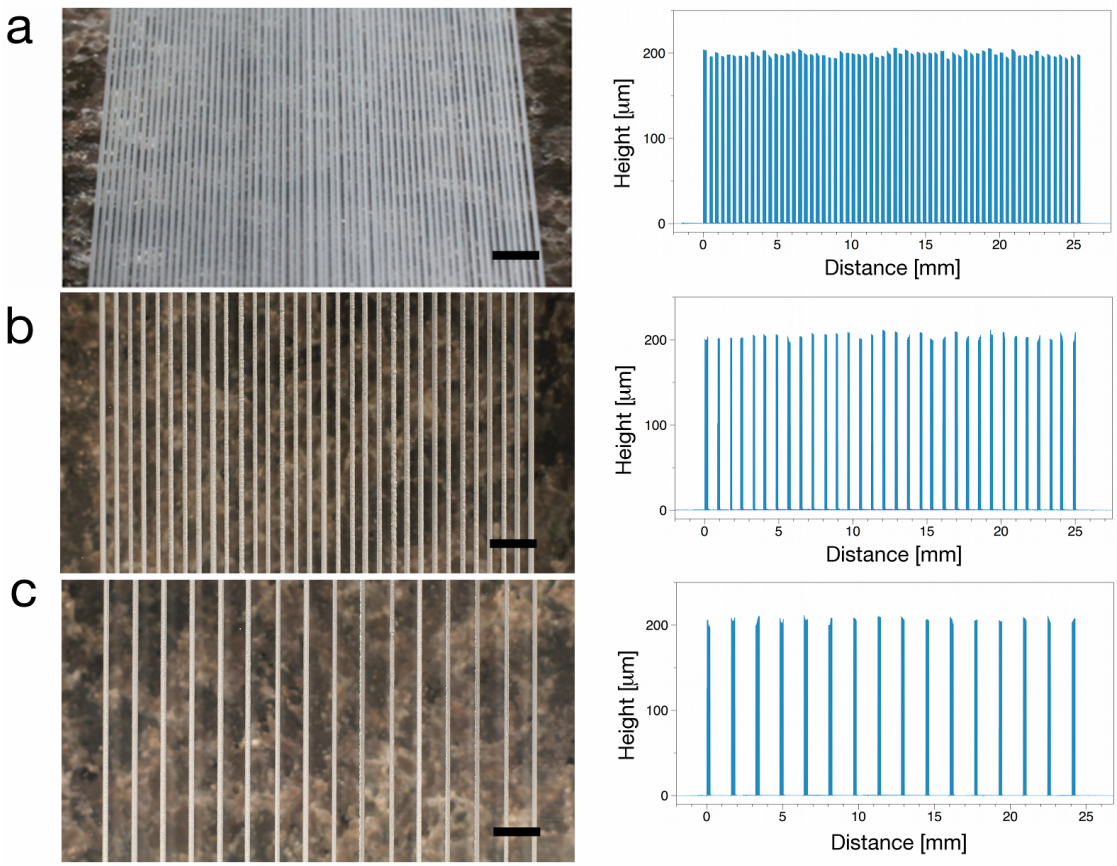

Figure 5.6. Images of a single pass of 64 nozzles printing simultaneously (left), with center-to-center spacings of (a) 400, (b) 800 and (c) 1600 µm (scale bar = 2 mm). Their corresponding height profiles (right) are measured with a non-contact optical profilometer.

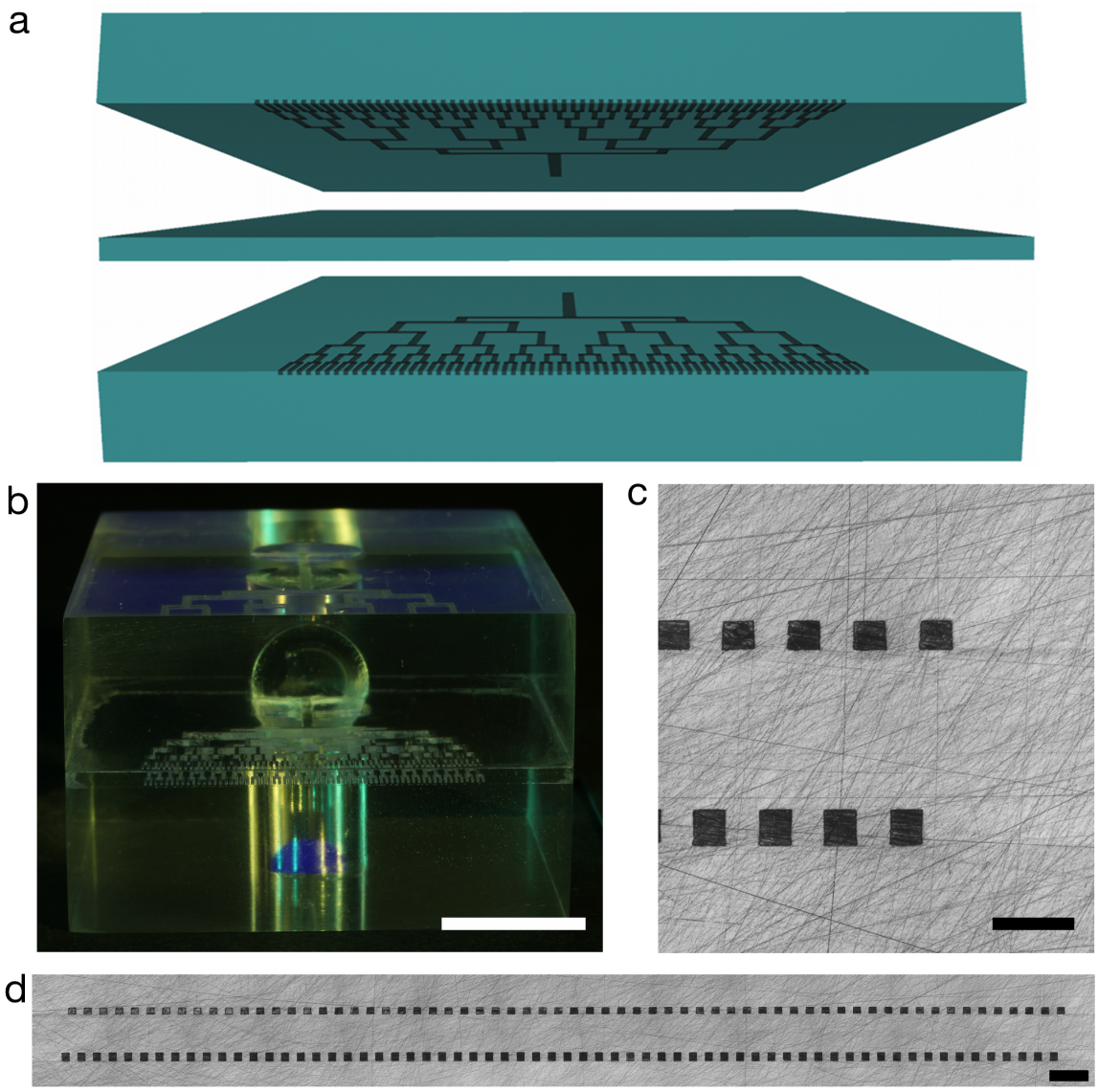

Figure 5.7 (a) Schematic of dual microvascular network printhead. The top and bottom networks are solvent welded to the center block with a predetermined offset. (b) Dual network multinozzle printhead with one inlet from the bottom and the second from behind (scale bar = 10 mm). (c) Nozzle openings for top network are offset by 200 μm relative to the bottom network (scale bar = 500 μm). (d) View of the 128 nozzles from the dual networks (scale bar = 1 mm).

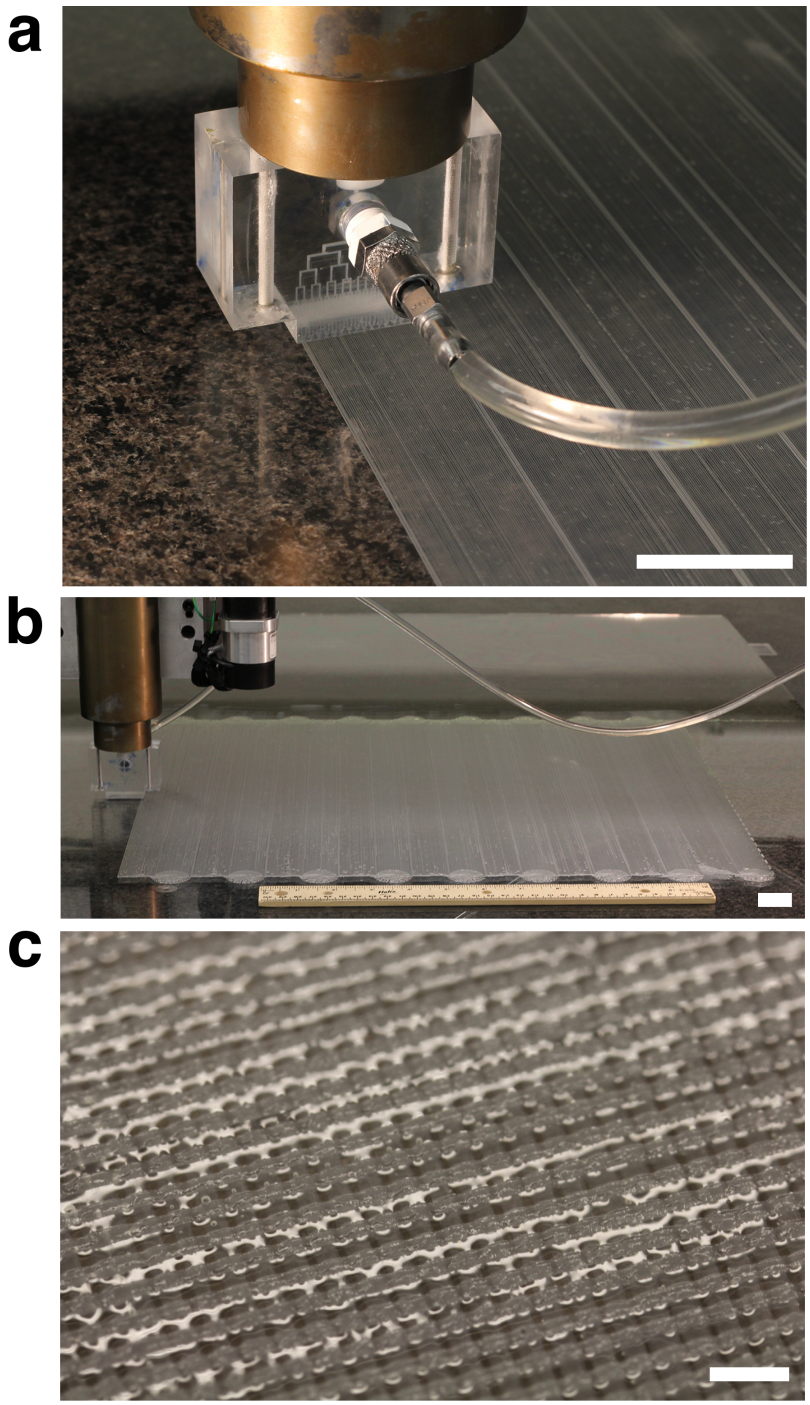

Figure 5.8 (a) Co-infiltration array with two embedded microvascular networks. The printhead is mounted to a rotation stage, with the leading network prints the fugitive wax filaments (top input, not visible), while the trailing network deposits the UV-curable epoxy (side input, visible). Scale bar = 25 mm. (b) Co-infiltration multinozzle printing of 0.5 x 0.5 m^2 structure. Scale bar = 25 mm. (c) View of two layer co-infiltrated structure with 200 μm spanning wax features and UV-curable epoxy in the interstitial regions. Scale bar = 1 mm.

CHAPTER 6

CONCLUSIONS

My dissertation describes the fabrication and implementation of interpenetrating microvascular networks which, in a binary motif, enable repeated self-healing and, in a ternary motif, accelerate the epoxy cure kinetics to quicken healing. Biological microvasculature and its hierarchical branching networks inspired the fabrication of microvascular multinozzle printheads that are capable of rapid parallel deposition of microscale filament features. The principle findings of my Ph.D. research are summarized below:

(1) Binary interpenetrating networks for self-healing

(a) Fabrication of interpenetrating microvascular networks required two key advances for direct write assembly: dual ink and vertical ink deposition. Dual fugitive ink printing allows deposition of separate, embedded interpenetrating microvascular networks. The distinct temperature-dependent rheology of a microcrystalline wax ink and a triblock-copolymer Pluronic ink permit selective removal of one ink, while the other ink remains intact.

(b) The second fabrication advance, vertical printing, enables features to transport fluid to the surface. Pressure valving integrated with vertical stage motion reproducibly prints vertical filaments. For aspect ratios below 25-35, depending on the filament diameter, features are stable. As the feature aspect ratio increases further, instability or collapse occurs. The buckling behavior and critical aspect ratio for filaments is described by column stability under self-weight.

(c) Binary interpenetrating microvascular networks are embedded in a substrate/coating architecture and filled with epoxy resin and hardener. A single crack forms in the brittle coating and fills with healing fluids. Healing efficiencies matching or exceeding those of previous self-healing microcapsule and microvascular architectures are observed for at least 30 continuous cycles.

(d) Fluorescence imaging of epoxy resin and hardener mimics in a crack plane geometry indicate several timescales for fluid mixing relevant to self-healing. The capillary wicking and taper migration times are on the order of seconds and dominate the diffusion time, which is on the order of hours.

(2) Ternary interpenetrating networks for thermally enhanced self-healing

(a) An epoxy resin and hardener system suitable for self-healing is thermally characterized by DSC, oscillatory rheology, and DMA from 30 – 70°C. Epoxy cure rates are significantly accelerated and indicate heal times can be reduced by an order of magnitude from 48 to 4 hours.

(b) A substrate/coating architecture with ternary interpenetrating microvascular networks is fabricated, with the third network devoted to circulating a thermal fluid. The specimen temperature response is measured with an infrared camera and shows a stable thermal profile is achieved within several minutes at a temperature a few degrees lower than the circulating fluid temperature.

(c) Mechanical testing demonstrates self-healing is accelerated by an order of magnitude, with comparable heal bending stress observed at 48, 8, and 4 hours for 30, 50, and 70°C respectively. Specimens heated to 50 and 70°C showed

consistent healing at times greater than the epoxy gel point, while 30°C showed inconsistent healing for up to 12 hours after the gel point.

(d) Fluorescent imaging of the epoxy components in the crack plane shows the ratio of resin to hardener closely matches their vertical conduit ratio. However, incomplete mixing is observed for a large majority of samples and only a minimal increase in mixed fluid occurs for elevated temperatures.

(3) Microvascular multinozzle printheads

(a) The design of a microvascular multinozzle printhead is inspired by hierarchical branching of biological microvasculature. Dimensions of the microvascular channels are calculated according to Murray's law to minimize pressure drops and the non-recoverable ink volume within the microvascular network.

(b) Computational fluid modeling is used to calculate fluid flow velocities for individual nozzles. Uniform flow is predicted for both Newtonian and non-Newtonian fluids. Dimensional tolerances necessary for microvascular fabrication are calculated to be ±5% for a 200 μm square nozzle.

(c) Microvascular multinozzle networks are quickly and reproducibly machined in acrylic with a CNC-mill. The milled networks are encapsulated by solvent welding with acetonitrile, which forms a strong bond with minimal feature deformation.

(d) Micro-PIV flow experiments are performed for water (μ=1 cP) and glycerol (μ=832 cP) solutions. Water flow rates are varied over two orders of magnitude (1 – 100 mm s^{-1}) and greater uniformity is observed for higher velocities.

Glycerol flow studies demonstrate flow uniformity roughly equivalent to that of water, despite its greater viscosity and concomitant decrease in Reynolds number.

(d) Patterning of parallel filamentary features demonstrates an unprecedented increase in effective printing speeds. Arbitrary center-to-center spacing of filaments are achieved, with all 64 feature height profiles measured to be within ±5%. Co-deposition of microcrystalline wax ink and a UV-curable epoxy from two closely-spaced microvascular arrays dramatically speeds the production of microstructures with defined porosity.